

The Role of Kinetics in Advanced Nuclear Fuel Reprocessing

Alexander Jackson, M.Eng(Hons.)



Submitted for the degree of Doctor of Philosophy at
Lancaster University

28 February 2023

Abstract

Liquid/liquid extraction processes are designed to selectively partition actinides with especially long-lived radiotoxicity from nuclear fuel waste streams. Uranium and plutonium partitioning is possible through application of the Plutonium Uranium Reduction Extraction (PUREX) and Advanced PUREX processes using tributyl phosphate (TBP). Furthermore, the technology for the fabrication of nuclear fuel using mixed actinide salt precursors relies heavily on the availability of the Innovative Selective Actinide Extraction (i-SANEX) and the European Grouped Actinide Extraction (EUROGANEX) processes. These processes utilise the organic ligand N,N,N',N'- tetraoctyl diglycolamide (TODGA) to extract trivalent lanthanides and actinides from nitric acid. As such, key properties and behaviours of TBP and TODGA are the object of the student's research at Lancaster University.

Using a Rotating Diffusion Cell (RDC), it is possible to interrogate the various chemical kinetic and diffusive contributions to actinide extraction by tracking the transfer of solutes over a fixed area membrane between the compartmentalised phases of nitric acid, containing dissolved metal ions, and TBP- or TODGA-loaded solvent. Furthermore, via manipulation of the rotation speed of the RDC several regimes of mass transfer may be reproduced, from low shear diffusion limiting conditions to high shear chemical kinetic control. The rate of extraction of the metal ions investigated is determined by ultraviolet-visible light absorbance spectroscopy.

An analytical model coded in the Process System Enterprise (PSE) General Process Modelling System (gPROMS) has been developed to estimate unknown constants, for example to obtain values for kinetic rate constants, based on the experimental extraction rates found. Information about unknowns such as these, as well as insight into the dominant mechanisms of transfer, are fundamental in building the safety case for state of the art reprocessing and partitioning plants.

Acknowledgements

This PhD was jointly funded by the National Nuclear Laboratory and the Engineering and Physical Sciences Research Council.

Throughout my time at Lancaster University, studying for a PhD and writing this thesis, I have received a great deal of support. First and foremost, I would like to thank Prof. Colin Boxall my supervisor. My work has also been ably supported by many academic staff, most notably Dr Michael Bromley, for assistance in the operation of the Rotating Diffusion Cell and Dr Richard Wilbraham, for insights into chemical processes relevant to my research. Furthermore, my industrial contacts at the National Nuclear Laboratory, Prof. Robin Taylor and Dr David Woodhead have been incredibly supportive throughout my studies.

I would like to thank the other PhD students studying at Lancaster University, and their partners and friends from the real world, for their friendship, most notably Michael Chimes, Suzanne Jones, Rosie Newton, Arran Plant, Andrew Morrall, Marcia Pryce, Oliver Tate, Nigel Huang, Olivia Albrecht, Jade Li, William Nelson, Amira Zied Abozied, Donglai Mao and Neil Barker. There are many more people who have been delightful at conferences and in passing. Though I may not name them all, my thanks extend to them also.

I would like to thank the Next Generation Nuclear Centre for Doctoral Training, run out of the University of Manchester by Prof. Scott Heath, Prof. Francis Livens, Mark Clegg and many other superb academic staff. During their excellent taught course preceding my studies I gained many friends and colleagues, most notably Olivia Voyce, Sarah Butterworth, Matt Jackson, Hannah Smith, Jonathan Cryer, James Mansfield and Connor McBride. All of them have my deepest thanks for being there for me right at the beginning.

Finally, my thanks go to my partner, Cara, my mum, my dad and my sister, Soph, for giving me a reason for doing all of this in the first place.

Declaration

I declare that the work in this thesis has been done by myself, unless otherwise stated, and has not been submitted elsewhere for the award of any other degree.

Alexander Jackson

Contents

Table of Contents

<i>Abstract</i>	<i>i</i>
<i>Acknowledgements</i>	<i>iii</i>
<i>Declaration</i>	<i>iv</i>
<i>Contents</i>	<i>v</i>
<i>List of Figures</i>	<i>vii</i>
<i>List of Tables</i>	<i>xii</i>
<i>List of Abbreviations and Technical Terms</i>	<i>xiv</i>
<i>List of Symbols</i>	<i>xvi</i>
<i>Chapter 1: General Introduction</i>	<i>1</i>
<i>Chapter 2: Supporting Background</i>	<i>1</i>
2.1 Nuclear Fuel Cycle.....	1
2.2 Chemistry of Key Actinides and Lanthanides in the context of PUREX.....	4
2.3 Mass Transfer and Chemical Kinetics in Actinide and Lanthanide Extraction Systems.....	9
2.3.1 Overview.....	9
2.3.2 Liquid-liquid Contactor Technology.....	11
2.4 Advanced PUREX Process.....	15
2.5 i-SANEX and GANEX Processes.....	16
2.6 Literature Survey of Mass Transfer and Chemical Kinetics.....	20
2.7 Scope of the Thesis.....	34
<i>Chapter 3: Experimental</i>	<i>35</i>
3.1 The Rotating Diffusion Cell Method.....	35
3.1.1 Sampling Protocol.....	36
3.2 Liquid-liquid Mixer-Centrifuge Method.....	37
3.3 Methods of Detection.....	37
3.3.1 Quantitative Metal Ion Detection with UV-visible Light Absorbance Spectroscopy.....	37
3.4 Computational Modelling in gPROMS.....	40
3.4.1 Confidence Intervals.....	41
3.4.2 t-value.....	41
3.4.3 Standard Deviation.....	41
3.4.4 Chi-squared Test for Goodness of Fit.....	41
<i>Chapter 4: RDC Extractions of Ce(IV) by TBP Part 1: Experiments which Underpin the Theory</i>	<i>44</i>
4.1 Published Absorbance Data.....	44
4.2 Obtaining the Organic Ce(IV) Extinction Coefficient.....	47
4.3 RDC Experimental Results in Units of Concentration.....	51

<i>Chapter 5: Theory</i>	55
5.1 RDC Parallels with Optical Rotating Disc Electrode Theory.....	55
5.2 Derivation of the RDC Diffusion-reaction model	59
5.3 Boundary condition where $[C]_i$ is equal to zero	64
5.4 Boundary condition where $[C]_i$ is a non-zero constant.....	68
5.5 Boundary Condition where $[C]_i$ is a distinct constant at each RDC rotation speed	69
5.6 Integrating Theory with Computational Modelling.....	70
5.6.1 Degrees of Freedom Analysis.....	70
<i>Chapter 6: RDC Extractions of Ce(IV) by TBP Part 2: Unknown Kinetic Constant Estimation</i>	72
6.1 Unknown Kinetic Constant Estimation Using Semi-analytical gPROMS Model.....	72
6.1.1 Estimating Unknown Constants Where $[C]_i$ is a Constant Across All RDC Rotation Speeds.....	73
6.1.2 Estimating Unknown Constants Where $[C]_i$ is a Distinct Constant at Each RDC Rotation Speed	78
6.2 Analysis of Ligand and Complex Concentration Profiles	82
6.3 Summary.....	86
<i>Chapter 7: RDC Extractions of Nd(III) by TODGA</i>	87
7.1 Nd(III) Calibration Curves of UV-visible Light Absorbance with Organic and Aqueous Concentrations	87
7.2 Stoichiometry of TODGA/Nd(III) Complex at Equilibrium	95
7.3 RDC Experimental Results for Nd(III)/TODGA.....	98
7.4 Unknown Kinetic Constants Estimation Using Semi-analytical gPROMS Model	105
7.4.1 Estimating Unknown Constants Where $[C]_i$ is a Constant Across All RDC Rotation Speeds.....	107
7.4.2 Estimating Unknown Constants Where $[C]_i$ is a Distinct Constant At Each RDC Rotation Speed .	110
7.5 Analysis of Ligand and Complex Concentration Profiles	115
<i>Chapter 8: Conclusions and Further Work</i>	120
<i>Bibliography</i>	123

List of Figures

Figure 1.1: Binding energy per nucleon curve (LibreTexts.org, 2019).	2
Figure 1.2: Pie chart showing the composition by mass (g/MTHM) of spent nuclear fuel: 96.5% uranium-238, 0.63% uranium-235, 0.60% other uranium isotopes, 1.2% plutonium isotopes, 0.12% other transuranic isotopes and 0.92% fission products. Burnup is 52 GWd/t (NEA, 2011).	5
Figure 1.3: Fission product isotopic yield for uranium-235, plutonium-239 and plutonium- 241 (IAEA, 2001).	5
Figure 2.1.1: The radiotoxicity with time of spent nuclear fuel (orange), nuclear glass (green), nuclear waste after a closed fuel cycle including minor actinide recycle (blue) and natural uranium ore (brown) (Poinssot, Rostaing, Greandjean, & Boullis, 2012, p. 353).2	2
Figure 2.1.2: Diagram of the PUREX process (Poinssot, Rostaing, Greandjean, & Boullis, 2012, p. 352).	3
Figure 2.1.3: European nuclear fuel cycle roadmap (Poinssot, Rostaing, Greandjean, & Boullis, 2012, p. 357).....	4
Figure 2.2.1: Blocks within the periodic table (Jones, 2001, p. 2). Actinides and lanthanides appear in the f-block.	5
Figure 2.2.2: Diagram showing the different actinide valencies (Cotton, 2006, p. 149).....	6
Figure 2.2.3: Technical flowsheet of the PUREX process where solvent refers to a TBP/OK organic phase (Nash & Lumetta, 2011, p. 147).	7
Figure 2.3.1: Diagram of the twin film model of the l/l interface, showing the phase boundary between two phases and the transferring species concentration profile each side of the interface.....	10
Figure 2.3.2.1: Diagram of a pump-mix box-type mixer-settler (Perry & Green, 2007, p. 1748).	11
Figure 2.3.2.2: Diagram of sieve tray pulsed columns whereby pulsing is performed on the whole liquid content (left) or the whole plate package (right) (Kislik, 2012).	12
Figure 2.3.2.3: Diagram of a centrifugal contactor/separator (Perry & Green, 2007, p. 1750).	13
Figure 2.5.1: Technical flowsheet of the i-SANEX process (Modolo, Wilden, Kaufholz, Bosbach, & Geist, 2014, p. 110).	17
Figure 2.5.2: Structural formula of a TODGA molecule.....	18
Figure 2.5.3: Technical flowsheets of the first stage of the GANEX process (left), which is common to all GANEX variations, and a particular variation of the second stage of GANEX known as the EUROGANEX process (right) (SACSESS, 2015).	18
Figure 2.6.1: Diagram of the needle tip (left) and apparatus (right) of the Single Drop method for studying mass transfer and chemical kinetics. (Hughes & Zhu, 1985).	21
Figure 2.6.2: Microscope image of a typical microfluidic liquid/liquid extraction capillary (left) and cross sectional diagram of the manifest two-phase flow (right) (Corne, et al., 2019).	22
Figure 2.6.4: Diagram of a Rotating Membrane Cell (RMC) (Simonin & Weill, 1998).	24

- Figure 2.6.5: Diagram of the Rotating Diffusion Cell (RDC) (Bromley & Boxall, 2015).....25
- Figure 2.6.6: Diagram of the hydrodynamic layers near to a rotating disc according to Levichian hydrodynamic theory.27
- Figure 2.6.7: Normalised Levichian speed functions of a fluid in the convection region near to a rotating disc where F , G and $-H$ are normalised dimensionless parameters related to the radial speed, the tangential speed and the axial speed respectively. ξ is dimensionless and is a function of ω and ν , which are rotation speed and viscosity respectively, and y , the normal distance from the surface of the rotating disc (Levich, 1962).29
- Figure 3.3.1.1: Diagram showing the UV-visible light spectrometer apparatus set up.38
- Figure 3.3.1.2: Example graphs showing the light intensity/raw counts spectra for neodymium(III) dissolved in nitric acid on top of pure water (left) and the absorbance spectrum of nitric acid and neodymium(III) ions in solution with respect to water as the chosen blank sample (right).39
- Figure 3.3.1.3: Illustration of base-line correction effects on a zoomed in section of Figure 3.3.1.2. By addition of the amount by which the absorbance base-line is shifted in the spectrum, shown by the red arrows, the parts of the spectrum which should be zero become zero and the characteristic peak adopts its slightly higher, true magnitude.40
- Figure 4.1.1: Example RDC spectra of Ce(IV) extraction by TBP/OK for a rotation speed of 1Hz. Base corrected with respect to a wavelength region of 400-500 nm. Data gathered by Bromley *et al* (Bromley & Boxall, 2015).45
- Figure 4.1.2: RDC extraction of Ce(IV) into the organic phase of 0.2 mol.dm^{-3} TBP in OK from an initial aqueous phase of 10 mmol.dm^{-3} Ce(IV) in 1.0 mol.dm^{-3} nitric acid, as a function of time. The organic absorbance was taken at a λ_{max} peak of 338 nm. Data originate from experiments conducted by Bromley *et al* (Bromley & Boxall, 2015).46
- Figure 4.2.1: Aqueous UV-visible light spectra for pre- and post-mixer-centrifuged samples of aqueous 10 mmol.dm^{-3} Ce(IV) in 1.0 mol.dm^{-3} nitric acid. The samples were contacted with an organic phase of 0.2 mol.dm^{-3} TBP in OK in the thermomixer. Absorbance computed with respect to a blank of 1.0 mol.dm^{-3} nitric acid with both the sample and the blank diluted by a factor of ten in 0.5 mol.dm^{-3} sulphuric acid. Base corrected with respect to absorbance at 800-850 nm.48
- Figure 4.2.2: Aqueous UV-visible light spectra for pre- and post-mixer-centrifuged samples of aqueous 10 mmol.dm^{-3} Ce(IV) in 1.0 mol.dm^{-3} nitric acid. The samples were contacted with an organic phase of 0.2 mol.dm^{-3} TBP in OK in the thermomixer. Plotted alongside is a pure nitric acid spectrum for comparison. Absorbance in all cases computed with respect to a blank of water with the two samples as well as the nitric acid diluted by a factor of ten in 0.5 mol.dm^{-3} sulphuric acid. Base-corrected with respect to absorbance at 800-850 nm.48
- Figure 4.2.3: Organic UV-visible light spectra for post-mixer-centrifuged samples of aqueous 10 mmol.dm^{-3} Ce(IV) in 1.0 mol.dm^{-3} nitric acid. The samples were contacted with an organic phase of 0.2 mol.dm^{-3} TBP in OK in the thermomixer. Absorbance computed with respect to a blank of the organic phase before it was mixed-centrifuged with the Ce(IV) loaded aqueous. Base corrected with respect to absorbance at 800-850 nm.49
- Figure 4.3.1: Concentration of organic Ce(IV) as a function of experimental time period for the RDC at several rotation speeds. Organic phase consists of 0.2 mol.dm^{-3} TBP in OK

and aqueous phase initially consists of 10 mmol.dm ⁻³ Ce(IV) in 1.0 mol.dm ⁻³ nitric acid. Base correction calculated with respect to the wavelength region 400-500 nm.....	51
Figure 4.3.2: RDC extraction flux, j , of Ce(IV) into the organic phase of 0.2 mol.dm ⁻³ TBP in OK from an initial aqueous phase of 10 mmol.dm ⁻³ Ce(IV) in 1.0 mol.dm ⁻³ nitric acid, as a function of RDC inverse square root of rotation speed, $\omega^{-0.5}$. Original data gathered by Bromley <i>et al.</i>	53
Figure 5.1.1: Diagram of an Optical Rotating Disc Electrode (Boxall, 2022).	56
Figure 5.2.1: Theoretical two-film model based on derived RDC theory. The general shape of the curves for the ligand and complex profiles shown originate from Equations 5.2.10 and 5.2.11. The metal ion curve is deduced from the fact that it diminishes close to the interface as it becomes complexed by the ligand.....	63
Figure 5.3.1: Case diagram of RDC flux efficiency, N , for the analytical model solved with $C_i=0$ boundary condition as a function of X_D , X_f and X_k ($\xi = X_D/X_f$, $\kappa = X_D/X_k$, $X_f = (D_L/k_f')^{1/2}$ and $X_k = (D_C/k_b)^{1/2}$	66
Figure 6.1.1.1: RDC experimental extraction flux as a function of RDC inverse square root of rotation speed, $\omega^{-0.5}$. Flux of Ce(IV) into the organic phase of 0.2 mol.dm ⁻³ TBP in OK from an initial aqueous phase of 10 mmol.dm ⁻³ Ce(IV) in 1.0 mol.dm ⁻³ nitric acid. Organic diffusivities are obtained directly from the literature and aqueous diffusivities are derived via the Stokes-Einstein relation. Best fit found using the model where $[C]_i$ is a constant in gPROMS.....	74
Figure 6.1.1.2: RDC experimental extraction flux, j , of Ce(IV) into the organic phase of 0.2 mol.dm ⁻³ TBP in OK from an initial aqueous phase of 10 mmol.dm ⁻³ Ce(IV) in 1.0 mol.dm ⁻³ nitric acid, as a function of RDC inverse square root of rotation speed, $\omega^{-0.5}$. $[C]_i$ fixed at 5%, 10% and 25% of the initial Ce(IV) concentration. Best fit achieved using the model where $[C]_i$ is a constant in gPROMS.....	77
Figure 6.1.2.1: RDC experimental extraction flux as a function of RDC inverse square root of rotation speed, $\omega^{-0.5}$. j of Ce(IV) into the organic phase of 0.2 mol.dm ⁻³ TBP in OK from an initial aqueous phase of 10 mmol.dm ⁻³ Ce(IV) in 1.0 mol.dm ⁻³ nitric acid. Best fit achieved using the model where $[C]_i$ is a distinct constant at each RDC rotation speed in gPROMS.....	79
Figure 6.1.2.2: The variation of interfacial complex concentration C_i as a function of inverse square root of rotation speed $\omega^{-0.5}$ corresponding to the estimations of the unknown constants shown in Table 6.1.2.1.	81
Figure 6.2.1: Aqueous phase diffusion layer concentration profiles resulting from the constant $[C]_i$ model of TBP (shown by L) and Ce(IV)/TBP complex (shown by C) with diffusivities derived via the Stokes-Einstein equation. List of constants: $D_L = 5.6 \times 10^{-10} \text{ m}^2 \cdot \text{s}^{-1}$, $D_C = 3.1 \times 10^{-10} \text{ m}^2 \cdot \text{s}^{-1}$, $\gamma = 2.0$, $k_f' = 14 \text{ s}^{-1}$, $k_b = 4.7 \text{ s}^{-1}$, $[C]_i = 1.0 \text{ mmol} \cdot \text{dm}^{-3}$	83
Figure 6.2.2: Aqueous phase diffusion layer concentration profile resulting from the model where $[C]_i$ is a distinct constant at each rotation speed of TBP (shown by L) and Ce(IV)/TBP complex (shown by C) with diffusivities derived via the Stokes-Einstein equation. List of constants: $D_L = 5.6 \times 10^{-10} \text{ m}^2 \cdot \text{s}^{-1}$, $D_C = 3.1 \times 10^{-10} \text{ m}^2 \cdot \text{s}^{-1}$, $\gamma = 2.0$, $k_f' = 5.6 \text{ s}^{-1}$, $k_b = 1.8 \text{ s}^{-1}$, $k_{ex} = 3.0 \times 10^{-5} \text{ m} \cdot \text{s}^{-1}$	85
Figure 7.1.1: Aqueous UV-visible light absorbance spectra of Nd ³⁺ dissolved in 1.0 mol.dm ⁻³ nitric acid, measured with respect to a blank water reference. As-obtained spectra have been smoothed using a 7-point moving average and base corrected as described in the	

text. Error bars have been calculated based on the two readings taken per concentration. The use of unit mM is shorthand for mmol.dm^{-3}	88
Figure 7.1.2: Aqueous neodymium(III) absorbance-concentration calibration curve for nitric acid concentration of 1.0 mol.dm^{-3} plotted in order to determine the UV-visible light absorbance extinction coefficients ($\epsilon_{\text{Nd,aq},\lambda_{\text{max}}}$) at $\lambda_{\text{max}} = 524, 578, 740$ and 795 nm	89
Figure 7.1.3: Aqueous neodymium(III) absorbance-concentration calibration curve for nitric acid concentration of 0.8 mol.dm^{-3} plotted for a study not presented, but included in order to validate the results shown in Figure 7.1.2.	91
Figure 7.1.4: Organic UV-visible light absorbance spectra of Nd(III) extracted from an initial load of 10 mmol.dm^{-3} of Nd(III) in 1.0 mol.dm^{-3} nitric acid into varying concentrations of TODGA in n-dodecane (5% octanol). Absorbances calculated with respect to a blank organic phase. Spectra smoothed using a 9-point moving average and base corrected using the average absorbance between 600-700 nm. Error bars calculated based on the two readings taken per concentration. The use of unit M is shorthand for mol.dm^{-3}	93
Figure 7.1.5: Aqueous UV-visible light absorbance spectra of Nd(III) following mixer-centrifuge with varying organic TODGA concentrations in n-dodecane, 5% octanol. Initial aqueous metal ion load is 10 mmol.dm^{-3} of Nd(III) in 1.0 mol.dm^{-3} nitric acid. Absorbances measured with respect to a blank spectrum of water. Spectra smoothed using a 9-point moving average and base corrected using the average absorbance between 600-700 nm and 820-850 nm. Error bars calculated based on the two readings taken per concentration. The use of unit M is shorthand for mol.dm^{-3}	94
Figure 7.1.6: Organic Nd(III) absorbance-concentration calibration curve for nitric acid concentration of 1.0 mol.dm^{-3} plotted in order to determine the UV-visible light absorbance extinction coefficients ($\epsilon_{\text{Nd,org},\lambda_{\text{max}}}$) at $\lambda_{\text{max}} = 584, 739$ and 803 nm	95
Figure 7.2.1: Distribution coefficient of Nd(III) in a TODGA/Nd(III) system as a function of initial TODGA concentration in the organic phase. Initial load of aqueous Nd(III) is 10 mmol.dm^{-3}	96
Figure 7.2.2: Log/log plot of Figure 7.2.1 which shows Nd(III) distribution coefficient as a function of initial organic TODGA concentration.	98
Figure 7.3.1: RDC spectra of Nd(III) extraction by TODGA/n-dodecane, with 5% octanol, for a rotation speed of 1 Hz. Base corrected calculated with respect to a wavelength region of 600-610 nm. Curve-smoothing via 9-point moving average.	99
Figure 7.3.2: RDC spectra of Nd(III) extraction by TODGA/n-dodecane, with 5% octanol, for a rotation speed of 2.5 Hz. Base corrected calculated with respect to a wavelength region of 600-610 nm. Curve-smoothing via 9-point moving average.	99
Figure 7.3.3: RDC spectra of Nd(III) extraction by TODGA/n-dodecane, with 5% octanol, for a rotation speed of 5 Hz. Base corrected calculated with respect to a wavelength region of 600-610 nm. Curve-smoothing via 9-point moving average.	100
Figure 7.3.4: RDC spectra of Nd(III) extraction by TODGA/n-dodecane, with 5% octanol, for a rotation speed of 7.5 Hz. Base corrected calculated with respect to a wavelength region of 600-610 nm. Curve-smoothing via 9-point moving average.	100
Figure 7.3.6: Concentration of organic Nd(III) as a function of experimental time period for the RDC at several rotation speeds. Organic phase consists of 0.2 mol.dm^{-3} TODGA in n-dodecane and aqueous phase initially consists of 10 mmol.dm^{-3} Nd(III) in 1.0 mol.dm^{-3}	

- nitric acid. λ_{max} used is 584 nm. Base correction calculated with respect to the wavelengths at 560 and 600 nm. 102
- Figure 7.3.7: RDC extraction flux, j as a function of RDC inverse square root of rotation speed, $\omega^{-0.5}$. Extraction of Nd(III) into the organic phase of 0.2 mol.dm⁻³ TODGA in n-dodecane and 5% octanol from an initial aqueous phase of 10 mmol.dm⁻³ Nd(III) in 1.0 mol.dm⁻³ nitric acid. 103
- Figure 7.3.8: Plots of Nd(III) concentration with time at different rotation speeds. The slopes of the regression lines plotted over the experimental data divided by two equate to the experimental error of the extraction flux in Figure 7.3.7. 104
- Figure 7.4.1.1: RDC experimental extraction flux as a function of RDC inverse square root of rotation speed, $\omega^{-0.5}$. j of Nd(III) into the organic phase of 0.2 mol.dm⁻³ TODGA in n-dodecane with 5% octanol from an initial aqueous phase of 10 mmol.dm⁻³ Nd(III) in 1.0 mol.dm⁻³ nitric acid. Organic diffusivities are obtained directly from the literature and aqueous diffusivities are derived via the Stokes-Einstein relation. Best fit using the model where $[C]_i$ is a constant in gPROMS. 107
- Figure 7.4.2.1: RDC experimental extraction flux, j , of Nd(III) into the organic phase of 0.2 mol.dm⁻³ TODGA in n-dodecane with 5% octanol from an initial aqueous phase of 10 mmol.dm⁻³ Nd(III) in 1.0 mol.dm⁻³ nitric acid, as a function of RDC inverse square root of rotation speed, $\omega^{-0.5}$. Best fit achieved using the model where $[C]_i$ is a distinct constant at each rotation speed in gPROMS. 111
- Figure 7.4.2.2: RDC experimental extraction flux as a function of RDC inverse square root of rotation speed, $\omega^{-0.5}$. j , of Nd(III) into the organic phase of 0.2 mol.dm⁻³ TODGA in n-dodecane with 5% octanol from an initial aqueous phase of 10 mmol.dm⁻³ Nd(III) in 1.0 mol.dm⁻³ nitric acid. k_{ex} boundary condition set at 8.00×10^{-6} m.s⁻¹. Best fit achieved using the model where $[C]_i$ is a distinct constant at each rotation speed in gPROMS. . 113
- Figure 7.4.2.3: Sensitivity analysis of k_{ex} using model fits of the TODGA/Nd(III) RDC experimental data. 115
- Figure 7.5.1: Aqueous phase diffusion layer concentration profiles resulting from the constant $[C]_i$ model of TODGA (shown by L) and Nd(III)/TODGA complex (shown by C) with diffusivities derived via the Stokes-Einstein equation. List of Constants: $D_L = 4.1 \times 10^{-10}$ m².s⁻¹, $D_C = 2.0 \times 10^{-10}$ m².s⁻¹, $\gamma = 2.0$, $k_f' = 49000$ s⁻¹, $k_b = 1.0$ s⁻¹, $[C]_i = 1.9$ mmol.dm⁻³. 116
- Figure 7.5.2: Zoomed in concentration profile of complex for the system described by the right hand plot of Figure 7.5.1. It is clear to see the negative slope of the complex concentration profile at distances very close to the interface at $x=0$ 118
- Figure 7.5.3: Aqueous phase diffusion layer concentration profiles of TODGA (shown by L) and Nd(III)/TODGA complex (shown by C). The concentration profiles were made using the model where $[C]_i$ is a constant at each RDC rotation speed. The diffusivities were derived via the Stokes-Einstein equation. List of Constants: $D_L = 4.1 \times 10^{-10}$ m².s⁻¹, $D_C = 2.0 \times 10^{-10}$ m².s⁻¹, $\gamma = 2.0$, $k_f' = 1100$ s⁻¹, $k_b = 1.0 \times 10^{-4}$ s⁻¹, $k_{ex} = 8.0 \times 10^{-6}$ m.s⁻¹. 119

List of Tables

Table 1.1: Examples of some isotopic fission (Sjöstrand & Story, 1960), neutron scatter (NIST, 2013) and neutron capture (NIST, 2013) microscopic cross sections for thermal neutrons.....	4
Table 2.6.1: Summary of relevant literature reports on the use and modelling of rotating and non-rotating RDC-based systems in the study of liquid-liquid extractions and other interfacial processes. The cells shaded blue are instances of the RMC technique being used.	30
Table 5.1.1: RDC theory correspondence with the ORDE (Jackson, Boxall, Bromley, Taylor, & Woodhead, 2019).....	57
Table 5.6.1.1: Degrees of Freedom (DoF) analysis for the RDC analytical model, with constant $[C]_i$ boundary condition.....	71
Table 6.1.1: Table containing viscosity and density information for odourless kerosene and water.....	73
Table 6.1.1.1: Constants associated with the optimum model fit of TBP/Ce(IV) system shown by the organic diffusivities model results shown in Figure 6.1.1.1. The χ^2 value being smaller than the χ^2 -critical value indicates a good model fit.	75
Table 6.1.1.2: Constants associated with the optimum model fit of TBP/Ce(IV) system shown by the aqueous diffusivities model results shown in Figure 6.1.1.1. The χ^2 value being smaller than the χ^2 -critical value indicates a good model fit.	75
Table 6.1.1.3: Constants associated with the optimum model fit of TBP/Ce(IV) system shown by the aqueous diffusivities model results shown in Figure 6.1.1.2. $[C]_i$ boundary condition set to a range of values; 5%, 10% and 25% the initial Ce(IV) concentration. Other constants: $D_L=5.6\times 10^{-10} \text{ m}^2.\text{s}^{-1}$, $D_C=3.1\times 10^{-10} \text{ m}^2.\text{s}^{-1}$, $\gamma=2.0$	77
Table 6.1.2.1: Constants associated with the optimum model fit of TBP/Ce(IV) system shown by the aqueous diffusivities model results shown in Figure 6.1.2.1. The χ^2 value being larger than the χ^2 -critical value indicates a poor model fit.	79
Table 6.1.2.2: Constants associated with the optimum model fit of TBP/Ce(IV) system shown by the organic diffusivities model results shown in Figure 6.1.2.1. k_{ex} boundary condition set at $3.0\times 10^{-5} \text{ m}.\text{s}^{-1}$. The χ^2 value being smaller than the χ^2 -critical value indicates a good model fit.	81
Table 7.1.1: UV-vis light absorbance extinction coefficients (ϵ) for aqueous Nd(III) ions at characteristic λ_{max} peaks. Units defined per cm of path length l . Corresponding to Figure 7.1.2.....	90
Table 7.1.2: UV-vis light absorbance extinction coefficients (ϵ) for aqueous Nd(III) ions at characteristic λ_{max} peaks. Units defined per cm of path length l . Corresponding to Figure 7.1.3.....	91
Table 7.1.3: UV-vis light absorbance extinction coefficients (ϵ) for organic Nd(III) ions at characteristic λ_{max} peaks. Units defined per cm of path length l	95
Table 7.4.1.1: Constants associated with the optimum model fit of the TODGA/Nd(III) system shown by the organic diffusivities model results shown in Figure 7.4.1.1. The χ^2 value being smaller than the χ^2 -critical value indicates a good model fit.....	108

Table 7.4.1.2: Constants associated with the optimum model fit of the TODGA/Nd(III) system shown by the aqueous diffusivities model results shown in Figure 7.4.1.1. The χ^2 value being smaller than the χ^2 -critical value indicates a good model fit.....	108
Table 7.4.1.3: Constants associated with the optimum model fit of the TODGA/Nd(III) system shown by the aqueous diffusivities model results shown in Figure 7.4.1.1. $[C]_i$ boundary condition set at 1.0 mmol.dm^{-3} . The χ^2 value being smaller than the χ^2 -critical value indicates a good model fit.	110
Table 7.4.2.1: Constants associated with the optimum model fit of the TODGA/Nd(III) system shown by the aqueous diffusivities model results shown in Figure 7.4.2.1. The χ^2 value being larger than the χ^2 -critical value indicates a poor model fit.....	112
Table 7.4.2.2: Constants associated with the optimum model fit of the TODGA/Nd(III) system shown by the organic diffusivities model results shown in Figure 7.4.2.2. k_{ex} boundary condition set at $8.00 \times 10^{-6} \text{ m.s}^{-1}$. The χ^2 value being larger than the χ^2 -critical value indicates a poor model fit.	113

List of Abbreviations and Technical Terms

ACS – American Chemical Society

AHA – Acetohydroxamic acid

ALARP – As low as reasonably practicable

CANDU – Canada Deuterium Uranium Reactor

CDTA – 1,2-(cyclohexylenedinitrilo)tetraacetic acid

CFD – Computational fluid dynamics

DEHiBA – N, N-(2-ethylhexyl)isobutyramide

DMDOHEMA – N, N'-Dimethyl, N, N'-dioctylhexylethoxymalon amide

EUROGANEX – European variation of the Grouped Actinide Extraction nuclear fuel partitioning process

FHA – Formohydroxamic acid

GANEX – Grouped Actinide Extraction nuclear fuel partitioning process

GENIORS – Generation IV Integrated Oxide Recycling Strategies

gPROMS – General Process Modelling System

HAN – Hydroxylamine

HPLC – High Performance Liquid Chromatography

IAEA – International Atomic Energy Agency

Magnox – Magnesium non-oxidising UK reactor design utilising magnesium alloy fuel cladding and unenriched uranium metal as fuel

MOX – Mixed oxide

MTHM – Metric tonnes of heavy metal

MTWCR – Mass Transfer with Chemical Reaction

NDA – Nuclear Decommissioning Authority

NEA – Nuclear Energy Agency

ODE – Ordinary Differential Equation

OK – Odourless kerosene

ORDE – Optical Rotating Disc Electrode

PSE – Process Systems Enterprise (developer of gPROMS)

PUREX – Plutonium Uranium Reduction Extraction: spent nuclear fuel reprocessing stage designed for the separation of plutonium and uranium from fission products and other transuranic isotopes

RDC – Rotating Diffusion Cell

SACSESS – Safety of Actinide Separation Processes

i-SANEX – Innovative Selective Actinide Extraction: partitioning process for the selective extraction of trivalent lanthanides and actinides from a PUREX raffinate, followed by a separation of the actinides from the lanthanides

List of Abbreviations and Technical Terms

1c-SANEX – i-SANEX process modified to be effective in a single cycle

TBP – Tributyl phosphate

Thorp – Thermal oxide reprocessing plant (at Sellafield)

TODGA – N,N,N',N' - tetraoctyl diglycolamide

List of Symbols

A – UV-visible light absorbance

$[C]_D$ – Complex concentration at distance X_D from the RDC interface in the aqueous phase (mol.dm^{-3})

$[C]_i$ – Complex concentration at the RDC interface in the aqueous phase (mol.dm^{-3})

$[C]_{\text{org}}$ – Complex concentration in the organic phase (mol.dm^{-3})

c – Speed of light (m.s^{-1})

d_{mem} – Diameter of the porous area of the RDC membrane (m)

$D_{\text{dist},M^{n+}}$ – Distribution coefficient of metal ion M

D_C – Diffusion coefficient of the complex in the aqueous phase ($\text{m}^2.\text{s}^{-1}$)

D_L – Diffusion coefficient of the ligand in the aqueous phase ($\text{m}^2.\text{s}^{-1}$)

D_S – Diffusion coefficient of a given solute S ($\text{m}^2.\text{s}^{-1}$)

E – Energy (J)

I – UV-visible light intensity ($(\text{mol photons}).\text{m}^{-2}.\text{s}^{-1}$ or photon counts)

I_0 – UV-visible light intensity for a ‘blank’ sample ($(\text{mol photons}).\text{m}^{-2}.\text{s}^{-1}$ or photon counts)

j – Flux of extraction over the aqueous/organic interface ($\text{mol.m}^{-2}.\text{s}^{-1}$)

k_b – Ligand/metal-ion decomplexation rate constant (s^{-1})

k'_f – Ligand/metal-ion complexation rate constant (s^{-1})

$K_{\text{Nd(III)}^{\text{eq}}^{\text{TODGA}}}$ – Equilibrium constant for TODGA/Nd(III) extraction (units system-dependent)

l – Sample length of the cuvette in the UV-visible light absorbance spectrometer (cm)

$[L]_D$ – Ligand concentration at distance X_D from the RDC interface in the aqueous phase (mol.dm^{-3})

$[L]_i$ – Ligand concentration at the RDC interface in the aqueous phase (mol.dm^{-3})

$[L]_{\text{org}}$ – Ligand concentration in the organic phase (mol.dm^{-3})

$[M]$ – Metal ion concentration in the aqueous phase (mol.dm^{-3})

m – Mass (kg)

v_x – Speed profile as a function of distance from the RDC interface (m.s^{-1})

X_D – Diffusion layer thickness in the aqueous phase (m)

γ – Ligand stoichiometry with respect the metal ion in the formed complex

ε – UV-visible light absorbance extinction coefficient ($\text{m}^3.\text{mol}^{-1}.\text{cm}^{-1}$)

λ – Wavelength (nm)

λ_{max} – Wavelength at which a peak in the UV-visible light absorbance spectrum occurs (nm)

μ – Phase dynamic viscosity (Pa.s)

ν – Phase kinematic viscosity ($\text{m}^2.\text{s}^{-1}$)

ω – RDC rotation speed (Hz)

The electron valency of elements, particularly metal ions, in this thesis is denoted interchangeably by brackets and superscript, i.e. a metal ion with a +2 charge can be expressed as M(II) and M^{2+} .

Chapter 1: General Introduction

The energy which is produced from nuclear fission originates from the phenomenon known as the *binding energy* of a nucleus. The binding energy is defined (per nucleon) as the energy required to split a nucleus into the subatomic particles of which it is made up (i.e. its protons and neutrons). As the mass of the nuclei of chemical isotopes increases as the periodic table is ascended, starting from low-mass isotopes, there is an increase in binding energy per nucleon until it peaks at around the mass of nickel. The binding energy per nucleon curve is shown by Figure 1.1. As the mass of the nuclei increases past nickel, binding energy per nucleon decreases. Related to this phenomenon, it is known that the nucleus of an atom has a mass which is less than the total mass of its constituent parts. This is known as the *mass defect* which is related to the binding energy by Einstein's equation $E = mc^2$, where E is energy, m is mass and c is the speed of light. Observing Figure 1.1, the heaviest isotopes have less of a mass defect, therefore also less binding energy per nucleon, than an elemental isotopes in the middle of the curve, for example nickel. Hence, when a heavy nucleus fissions to form two fission fragments, the mass defect decreases and this lost mass is reconstituted as fission fragment kinetic energy (94%), prompt neutron kinetic energy (3%) and prompt gamma radiation (3%) (Joyce, 2016, p. 74). *This* is the energy which western societies seek to utilise. Inside a nuclear reactor, this kinetic energy is transferred through the reactor materials until it comes into contact with a coolant (typically water), causing it to ultimately raise steam and drive a turbine to produce electricity.

Historically, the principal elemental isotope in the periodic table which undergoes fission is uranium-235. Uranium occurs naturally as an ore comprised of 99.3% uranium-238 and 0.7% uranium-235 isotopes; but only the latter is fissile in the most commonly used thermal reactors (Taylor, 2015, p. 6). In early nuclear reactors, such as the Magnox reactors built in the UK, natural uranium metal was used as reactor fuel due to the unavailability of enrichment facilities in the UK, however, as the technology developed, the industry standard fuel became uranium dioxide (UO₂) with the uranium-235 content enriched to 3-5% (Joyce, 2016, pp. 31-33). To explain choices like these in fuel technology development one must understand the interactions between neutrons and uranium-235 on the atomic scale.

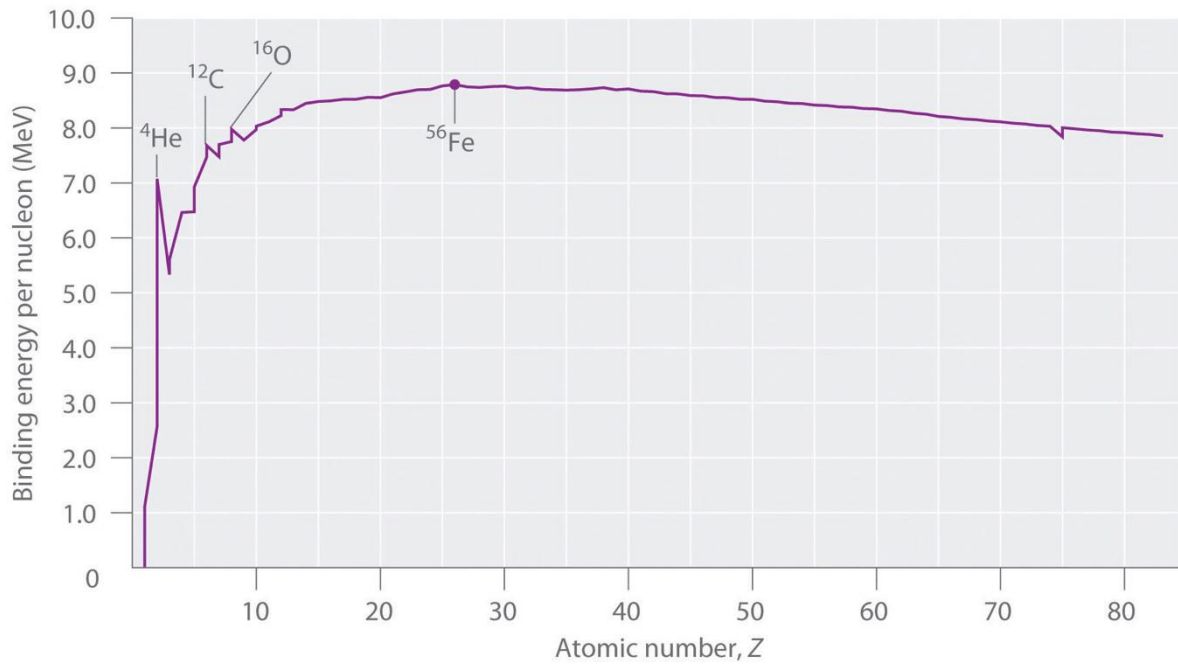


Figure 1.1: Binding energy per nucleon curve (LibreTexts.org, 2019).

Neutrons are the subatomic particles which cause a sustainable fission chain reaction to occur and they possess a wide range of kinetic energies from 0.025 eV up to 5 MeV (Joyce, 2016, p. 68). The neutrons at the low end of this scale are ‘thermal’ neutrons and at the high end they are ‘fast’ neutrons (Amsler, 2015, pp. 15-20 (c. 5)). Neutrons are typically *fast* if they are travelling through air or materials that ensure a minimal change in neutron momentum. Conversely, neutrons lose their kinetic energy and become *thermal* when they collide with the atoms of a *moderator*, water or graphite, for example. When a neutron, of any energy, collides with a nucleus of uranium-235, it can either scatter, be captured, or cause fission to occur (Joyce, 2016, p. 67). The moderation of neutrons is important because fission is the more likely outcome when a neutron of thermal energy collides with a uranium-235 nucleus, which is desirable from an energy production perspective. Each fission reaction produces another neutron which continues the fission chain reaction. When the reactor is critical there is exactly one neutron which goes on to cause another fission per neutron produced from a previous fission, meaning the reactor will have a constant and stable power output. At sub-criticality, less than one neutron goes on to cause fission per neutron produced from fission which will eventually lead to fission ceasing within the reactor and its power output decreasing to zero. At super-criticality, greater than one neutron goes on to cause fission per neutron produced and the fission chain reaction will continue to increase, generating an increasing amount of energy within the reactor. In general, low atomic mass isotopes, carbon

in graphite and oxygen and hydrogen in water, are good moderators and the higher the atomic mass of an elemental isotope, the lower its capacity for moderation. However, the density of a material and the likelihood of a collision resulting in scattering, and not capture, must also be considered to assess the effectiveness of a moderator (Burchell, 2001).

A useful property to evaluate the capacity for fission, neutron scatter or neutron capture is the neutron microscopic *cross section*. The greater the value of the microscopic cross section with respect to a particular neutron event, the higher the likelihood is for that neutron event to occur. Microscopic cross sections for some key isotopes are shown in Table 1.1. It is immediately clear from Table 1.1 why isotopes like carbon, oxygen and hydrogen, are deployed as moderators as their scattering microscopic cross sections are two to four orders of magnitude higher than their capture microscopic cross sections. Neutrons colliding or passing close to atoms of these isotopes will lose energy from the interaction, will become thermalised, and remain mobile within the medium rather than be captured which would prevent any further neutronic interactions in the material. Furthermore, heavy water containing deuterium (hydrogen-2), found to be an especially effective moderator (historically) used in Canadian CANDU reactors, shows an extremely low capture microscopic cross section which is why the fuel rods in these reactors do not need to be enriched to 5% U-235 content. Conversely, it is not always desirable to allow neutron interactions to continue to multiply indefinitely. Boron-10 has a high capture microscopic cross section, shown in Table 1.1, which is why it is often used as a neutron poison and in control rods to shut down and/or control the power output of a nuclear reactor. The heavier fissile isotopes of U-233, U-235 and Pu-239 shown in Table 1.1 have similar fission microscopic cross sections, however U-235 has the lowest capture microscopic cross section compared to the other two. Thus, U-235 is more likely to be able to sustain a fission chain reaction while U-233 and Pu-239 are respectively five and ten times more likely to capture a neutron and undergo α or β decay, forming other isotopes of similar atomic mass which build up inside the nuclear fuel.

Though graphite and heavy water have been moderators incorporated into early reactor designs, the most common moderator is light water (Joyce, 2016, pp. 122-123). However, as described below in Table 1.1, its absorption microscopic cross section is much higher than either graphite or D₂O, resulting in a need to enrich the uranium-235 content of reactor fuel to 5%, or similar. Furthermore, uranium dioxide, as opposed to uranium metal became the

industry standard fuel simply because of its higher thermodynamic efficiency, safety and resilience to the rigours of reactor use attributable to its higher melting point, lower chemical reactivity, etc (Joyce, 2016, p. 10).

Table 1.1: Examples of some isotopic fission (Sjöstrand & Story, 1960), neutron scatter (NIST, 2013) and neutron capture (NIST, 2013) microscopic cross sections for thermal neutrons.

Elemental isotopes	Thermal neutron fission microscopic cross section (barns)	Total bound neutron scattering microscopic cross section (barns)	Thermal neutron capture microscopic cross section (barns)
Hydrogen-1	-	82.03	0.3326
Hydrogen-2	-	7.64	0.000519
Boron-10	-	3.1	3835
Carbon-12	-	5.559	0.00353
Oxygen-16	-	4.232	0.0001
Uranium-233	536	12.9	574.7
Uranium-235	598	19.3	100.1
Plutonium-239	648	7.7	1017.3

When neutron fission or capture occurs, different by-products build up inside the body of the fuel. If neutron capture occurs, rather than fission, heavier isotopes, known as ‘transuranic isotopes’, such as plutonium, neptunium, americium and curium, of varying isotopic composition, of which some are also fissile, are produced. Neptunium, americium and curium are also referred to in this thesis as the ‘minor actinides’. Alternatively, if fission occurs, the fissile nuclei in the oxide fuel become two fission fragments of any two lighter elemental isotopes in the periodic table (Joyce, 2016, pp. 80-83). At the point when the nuclear fuel leaves the reactor after operation, the isotopic composition of the fuel is as shown by Figure 1.2. It is clear to see how the initial percentage of U-235 of ~5%, present in the fresh fuel, has dropped to 0.63% (in this example, depending on burnup) due either to successful fission or neutron capture. Figure 1.2 exhibits how the transuranic isotopes and fission products emerge in place of U-235.

A more detailed breakdown of the fission product yield is shown by Figure 1.3. The isotopes shown are produced by the most fissile of the elemental isotopes found in operating nuclear fuel, which are uranium-235, plutonium-239 and plutonium-241. During reactor operation, which could be for some hours or weeks depending on the required power output and reactor type, a range of fission product isotopes build up inside the reactor fuel.

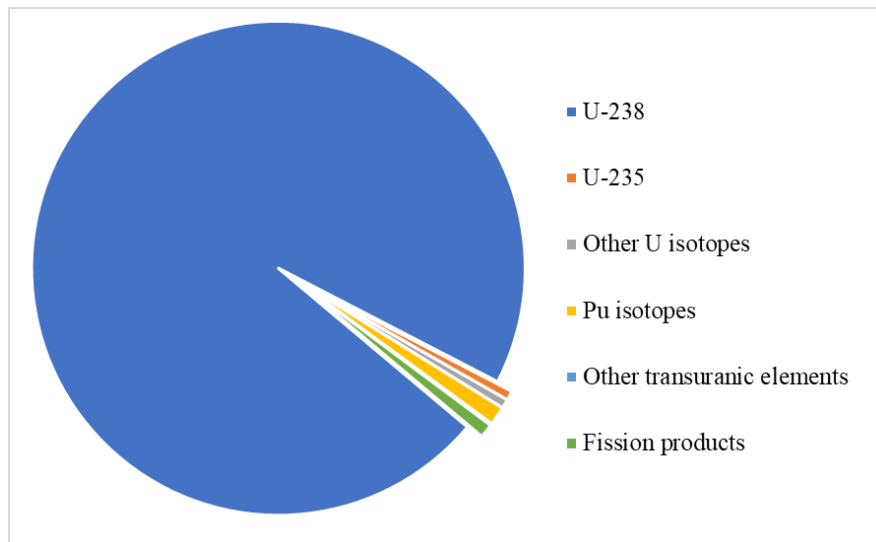


Figure 1.2: Pie chart showing the composition by mass (g/MTHM¹) of spent nuclear fuel: 96.5% uranium-238, 0.63% uranium-235, 0.60% other uranium isotopes, 1.2% plutonium isotopes, 0.12% other transuranic isotopes and 0.92% fission products. Burnup is 52 GWd/t² (NEA, 2011).

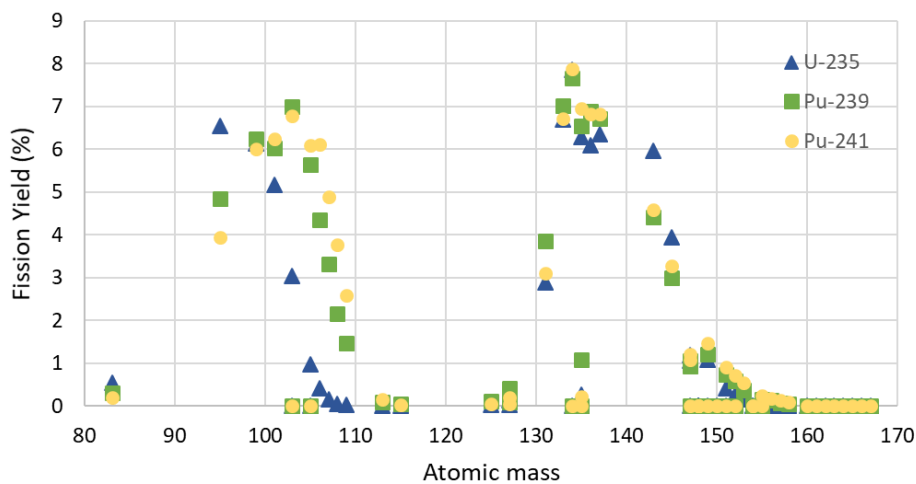


Figure 1.3: Fission product isotopic yield for uranium-235, plutonium-239 and plutonium-241 (IAEA, 2001).

The treatment of the spent fuel following its residency in a nuclear reactor represents a contentious aspect of the nuclear industry with significant safety management requirements. The potentially harmful chemical and radiological effects on biological systems of

¹ MTHM – metric tonnes of heavy metal.

² GWd/t – gigawatt day per metric tonne

transuranic isotopes and fission products spurred the development of a robust and, above all, safe nuclear fuel cycle, which is the topic of Section 2.1. Processes designed to improve the management of the spent fuel within the nuclear fuel cycle continue to be keenly researched by the nuclear industry. The work presented here focuses on furthering this knowledge.

A detailed description of the nuclear fuel cycle follows. However, it is useful to first examine the causes of the harmful effects of nuclear waste products. At the start of the twentieth century, around thirty years before the discovery that fission produces energy, scientists such as Henri Becquerel are credited to have found that some elemental isotopes in the periodic table are radioactive (Nye, 2002, pp. 352-355). Radioactive isotopes have the potential to release alpha (α), beta (β) or gamma (γ) radiation. Other types of ionising radiation are possible, however α , β and γ are commonly used to characterise radiation sources in the context of nuclear safety and thus they are the focus here. α radiation is a highly ionising short range particle comprised of two protons and two neutrons, essentially a helium atom without its electron shell, β radiation is a moderately ionising medium range free electron and γ radiation is a weakly ionising long range electromagnetic wave with a frequency of greater than 1019 Hz (Martin, 2011, pp. xiv-xvi).

The different radiation types present different hazards. For example, γ radiation travels many metres and may pass through the walls of typical buildings, but is only weakly ionising, meaning that its damage can be limited by adequate lead-lined concrete shielding.

Conversely, α radiation is very low range, only a couple of centimetres, but is highly ionising meaning if an α source is ingested or inhaled, for instance, it can cause a large amount of biological damage. The stopping power of α radiation is such that it only requires paper or skin to adequately shield its effects. β radiation presents a level of hazard somewhere in between that of α and γ , having a range of around three metres, may pass through skin, but can be abated by a thin sheet of aluminium or Perspex.

Natural, as well as enriched, uranium, before it has been loaded into a reactor, is only a weak α emitter and thus is easily managed from the twin perspectives of safety and security. The transuranic isotopes also emit α , but additionally emit extremely harmful levels of β and γ radiation through the processes of radioactive decay aforementioned (Joyce, 2016, pp. 89-99). Fission fragments, such as caesium-137, strontium-90 and others, are also β and γ radioactive. The above radioactive inventory in spent nuclear fuel, and nuclear environments

generally, requires much greater control measures from safety and security perspectives. In exercising these control measures, it is the goal of UK nuclear industry employees to ensure the radiation exposure of nuclear industry employees is As Low As Reasonably Practicable (ALARP).

It was the goal of the civil nuclear economy, in its earliest incarnation, to consider the contained elemental isotopes in reactor fuel to be tradeable commercial products like any other (Hecht, 2012, pp. 29-34). The creation of a nuclear fuel cycle was the result of this consideration and is the subject of the proceeding section.

Chapter 2: Supporting Background

2.1 Nuclear Fuel Cycle

The nuclear fuel cycle envelopes the entire endeavour of procuring energy from the nuclear fission of uranium taking into account the reprocessing and/or disposal of the harmful by-products briefly outlined in Section 1.

The underlying driver to incorporate a nuclear fuel cycle, of which there are a number of variations, into nuclear industrial discourse is illustrated by Figure 2.1.1. In summary, spent fuel from a nuclear reactor exceeds the radiotoxicity of natural uranium ore initially by three orders of magnitude and only diminishes back to acceptable levels after a period of 10^5 to 10^6 years, which is shown by the orange curve in Figure 2.1.1. This radiotoxicity scenario carries an epoch-sized time period and is practically beyond the power of human beings to conceive. Uranium and plutonium may be removed from spent fuel and recycled as reprocessed UO_2 fuel, in the case of the former, and MOX (mixed-oxide) fuel, in the case of the latter. The remaining fission products and transuranic isotopes are immobilised in a glass wasteform; nuclear glass, which is shown by the green curve in Figure 2.1.1. Due to the long half lives of the radioisotopes typically vitrified into nuclear glass, it remains a greater than acceptable radiotoxicity risk for 10^3 to 10^4 years. However, if the transuranic isotopes other than plutonium are removed and recycled as minor actinide-bearing fuel in a closed fuel cycle, the radiotoxicity of the remaining waste decreases to an acceptable level in a few hundred years. This is shown in blue on Figure 2.1.1. *This* nuclear waste legacy may only be the burden on a small number of generations which is a project far less daunting than the alternatives and much more marketable as a solution.

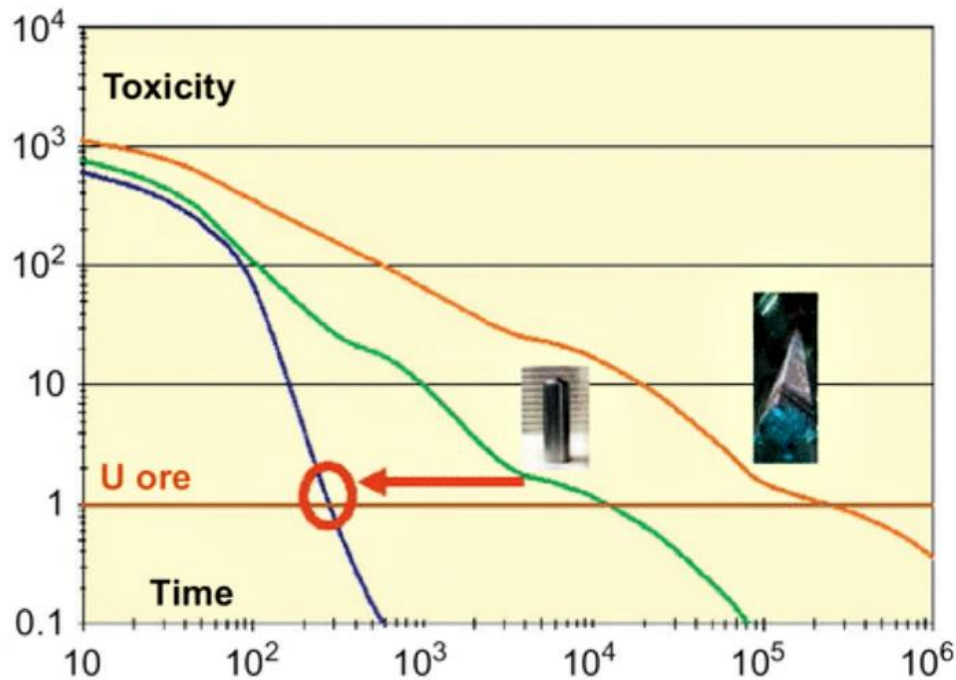


Figure 2.1.1: The radiotoxicity with time of spent nuclear fuel (orange), nuclear glass (green), nuclear waste after a closed fuel cycle including minor actinide recycle (blue) and natural uranium ore (brown) (Poinssot, Rostaing, Greandjean, & Boullis, 2012, p. 353).

There are two broad categories of fuel cycle; open and closed. The closed fuel cycle requires the implementation of a series of reprocessing steps including:

- fuel rod conditioning, where the cladding is sheared or cut;
- dissolution of the fuel in an aqueous medium;
- the liquid/liquid extraction of recyclable elemental isotopes, which are uranium and plutonium principally, but the minor actinides are intended to be eventually utilised also when the technology allows; and
- vitrification of the remaining fission products, turning them into a glass wastefrom for long-term storage (Taylor, 2015, pp. 97-105).

Alternatively, the open cycle is a once-through chain of processes which attempts to minimise the instances where a human being can come into contact with the products within the fuel (Joyce, 2016, p. 310). In an open cycle, the fuel assemblies themselves may not even be disassembled but directly stored as they are pending direct and final disposal in a geologic repository.

A chemical partitioning process, developed for the closed fuel cycle is the PUREX process. The chemistry of PUREX outlined in more detail in Section 2.2, however the overarching aim is to produce two separate, pure streams of material; uranium and plutonium which, in a plant such as Thorp, are subsequently converted into their oxides, as shown in Figure 2.1.2.

As stated in Section 1, typically 95% of the uranium in nuclear fuel is uranium-238; an unstable isotope, but with an extremely long half-life (forming thorium-234 by α decay), that may only spontaneously fission to a very small extent (Joyce, 2016, p. 93). Following a chemical separation of uranium and plutonium from dissolved spent nuclear fuel, the majority of the uranium remains the same -238 isotope which went into fabricating the fuel. However, the most prevalent isotopes of plutonium (-238, -239, -240, -241 and -242) in spent nuclear fuel are far from harmless and in a greater abundance than the fissile fraction of the uranium; uranium-235. Such is their instability, all isotopes of plutonium may themselves undergo, or cause via transmutation, spontaneous fission or stimulated fission in a thermal reactor (Joyce, 2016, p. 94).

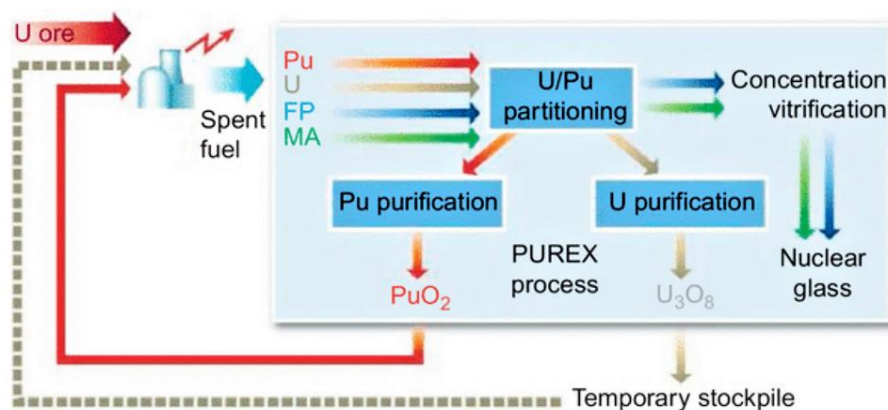


Figure 2.1.2: Diagram of the PUREX process (Poinssot, Rostaing, Greandjean, & Boullis, 2012, p. 352).

As well as the PUREX process, civil use of plutonium and reprocessed U is present in future projections of nuclear fuel technology e.g. the proposed European nuclear fuel cycle roadmap shown in Figure 2.1.3.

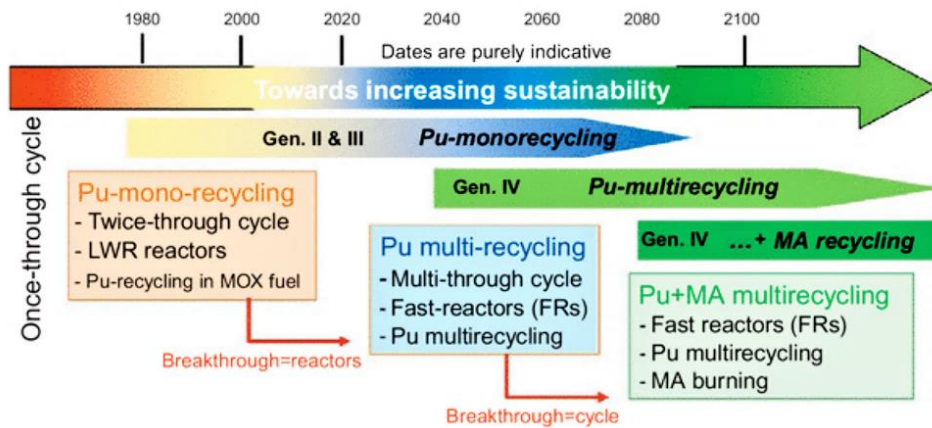


Figure 2.1.3: European nuclear fuel cycle roadmap (Poinssot, Rostaing, Greandjean, & Boullis, 2012, p. 357).

The final discussion point in this section concerns the transuranic isotopes so far unaddressed in depth; the minor actinides such as americium and curium. As can be seen in the bullet points in Figure 1.2.3, another type of nuclear reactor is proposed to utilise the energy contained in the transuranic isotopes; a *fast reactor*. Recalling the definition of fast neutrons from Section 1.1, a fast reactor relies on neutrons with an energy upwards of 1 MeV (Amsler, 2015, pp. 15-20 (c. 5)). Though a fast reactor is unsuitable for uranium-based fuel, it may be used to burn up the transuranic isotopes which are more likely to fission in a fast neutron flux.

At time of writing, fast reactor technology is not ready to be deployed beyond a research setting. Fast reactors are included in the plans for Generation IV reactor technology, which consists of predominantly non-commercial conceptual designs. Furthermore, the safety case based on current knowledge of fuel fabrication, plant material and structural stability and chemical degradation and corrosion, has not been finalised. The reprocessing technology required for the supply chain of proposed future nuclear reactors is also still at the research stage (NIRAB, 2020) and is the area which the work presented here aims to build upon. Key to this are aspects of the fundamental chemistries of the actinides and lanthanides, which are discussed in the following section.

2.2 Chemistry of Key Actinides and Lanthanides in the context of PUREX

For this section, which deals with the principal chemistry relevant to nuclear reprocessing, the case study is PUREX, a well-known reference process. Despite the work presented here

being largely concerned with advanced reprocessing solutions being developed to replace PUREX, such as the i-SANEX and GANEX processes, the mechanism of PUREX is similar to most other chemical partitioning systems deployed by the nuclear industry.

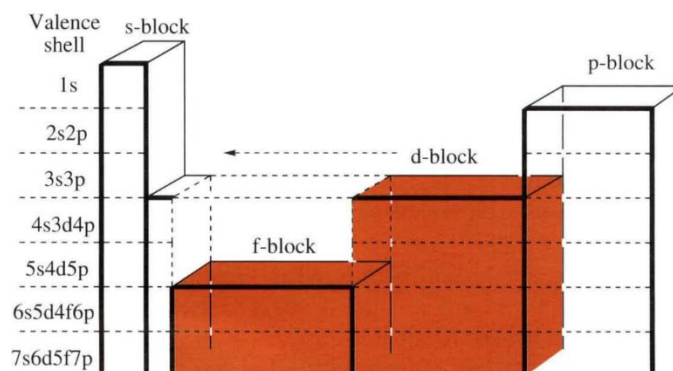


Figure 2.2.1: Blocks within the periodic table (Jones, 2001, p. 2). Actinides and lanthanides appear in the f-block.

The periodic table organises elements into different blocks representing electron valency, which is shown by Figure 2.2.1. For example, the s-block contains the elements which have electron valency in the atomic s-orbital, the p-block contains likewise for the atomic p-orbital, etc (Jones, 2001, p. 1). Actinides and lanthanides are f-block metals and are similar to the d-block elements in some physical aspects such as heat and electricity conduction as well as versatility in acid-base chemistry (Jones, 2001, p. 3). It is the acid-base chemistry and the relative stability of the ionic valencies of the different actinides and lanthanides that reprocessing steps such as the PUREX process relies upon.

In a similar way to d-block transition metals, actinides and lanthanides may exist in a range of valencies (2+ to 7+). The lanthanide series favours the 3+ oxidation state, as does the actinide series from americium upwards in mass, but the actinide series between thorium and plutonium, inclusive, have 4+, 5+ and 6+ stabilities under certain aqueous conditions (Cotton, 2006, p. 149). A helpful diagram of the divergence in valency of some actinides is shown by Figure 2.2.2.

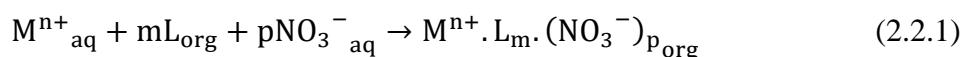
	2+	3+	4+	5+	6+	7+
Ac		Common				
Th	?	Common	Common			
Pa		Common	Common	Common		
U		Common	Common	Common	Common	
Np		Common	Common	Common	Common	Common
Pu		Common	Common	Common	Common	Common
Am	Common	Common	Common	Common	Common	?
Cm		Common	Common	Common	?	
Bk		Common	Common	Common		
Cf	Common	Common	Common			
Es	Common	Common	?			
Fm	Common	Common				
Md	Common	Common				
No	Common	Common				
Lr		Common				

Known
 Common

Figure 2.2.2: Diagram showing the different actinide valencies (Cotton, 2006, p. 149).

As well as the oxidation state of the actinide or lanthanide in question, another property, which the PUREX process exploits, is the ability for these metal ions to form neutral complexes with organic ligands in the context of a liquid/liquid extraction process. The mixture of fission products, minor actinides and stable uranium and plutonium ions, UO_2^{2+} , U^{4+} , Pu^{4+} and Pu^{6+} , dissolved in nitric acid may form complexes with TBP (tributyl phosphate). A TBP organic solution in OK (odourless kerosene) is immiscible when added to the acid solution of metal ions but on vigorous mixing, to form a (metastable) emulsion and subsequent centrifugation or settling, the metal ions have had sufficient time to contact the ligand molecules at the aqueous-organic solvent interface that comprises the surface of the emulsion droplets that complexation may occur, the resultant complexes being transferred or extracted into the organic phase (Joyce, 2016, p. 314). Overall, the metal ion has been extracted from one liquid, the aqueous nitric acid phase, to another, the TBP/OK organic phase – hence liquid/liquid extraction.

This chemical process is broadly described by Equation 2.2.1 where M is the metal ion, L is the ligand, in this case TBP, and subscript org and aq denotes presence in the organic and aqueous phases respectively. It is known that nitrate ions (NO_3^-) also form part of the complex in order to form an overall neutral extracted entity.



A useful metric to define at this stage is the distribution (or partition) coefficient, $D_{\text{dist},M^{n+}}$, shown by Equation 2.2.2, which is the quotient of the metal ion concentration in the organic phase over that in the aqueous phase.

$$D_{\text{dist},M^{n+}} = \frac{[M^{n+} \cdot L_m \cdot (\text{NO}_3^-)_p]_{\text{org}}}{[M^{n+}]_{\text{aq}}} \quad (2.2.2)$$

At 22°C with 2.0 mol.dm⁻³ nitric acid and 30% TBP/OK organic phase, the distribution coefficients of UO₂²⁺, U⁴⁺, Pu⁴⁺ and Pu⁶⁺ are greater than 1 (15, 1.2, 2.1 and 8 respectively (Nash & Lumetta, 2011, p. 143)), implying that there is a greater proportion of metal ion in the organic phase than in the aqueous phase following mixing/settling. At the same conditions, all other significant metal ions have distribution coefficients of less than 1, meaning the non-uranium, non-plutonium ions remain in the acid (Joyce, 2016, pp. 314-315). In the scaled up industrial PUREX process, a series of contactors, as opposed to one, are required. The small amounts of fission products, which are extracted by the organic, are scrubbed back into the aqueous phase and the uranium and plutonium remaining in the acid is extracted by a cleaner TBP phase. A simplified technical flowsheet of this process is shown by the left-hand side of Figure 2.2.3.

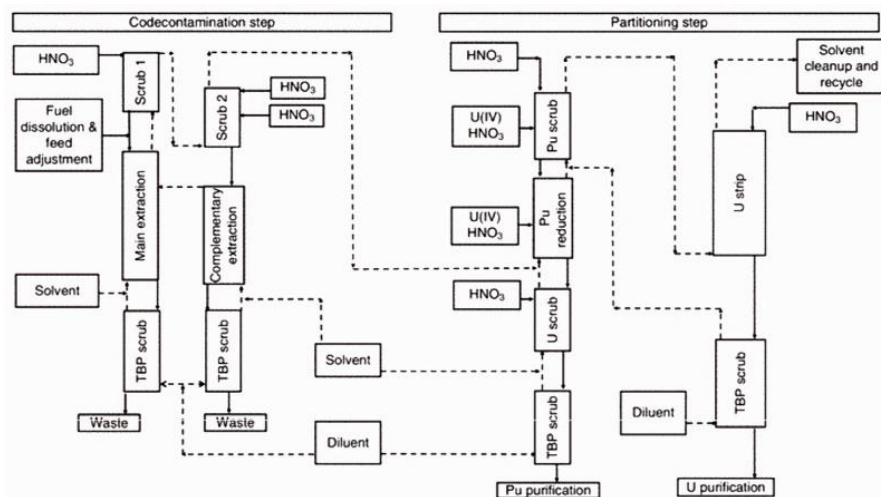


Figure 2.2.3: Technical flowsheet of the PUREX process where solvent refers to a TBP/OK organic phase (Nash & Lumetta, 2011, p. 147).

Described above is the extraction of the uranium and plutonium, leaving all other components of the spent nuclear fuel dissolved in the nitric acid. The right-hand side of the flowsheet shown by Figure 2.2.3 shows the subsequent partitioning of uranium and

plutonium by reducing the Pu^{6+} to Pu^{4+} , then to Pu^{3+} . Plutonium in its trivalent form has a distribution coefficient of 0.62, crucially less than 1, at 25°C with 3.0 mol.dm⁻³ nitric acid and 30% TBP/OK organic phase (Joyce, 2016, p. 314). Hence, the same liquid/liquid extraction process using TBP may be deployed to partition uranium from plutonium. Uranous ions (U^{4+}) may act as a reducing agent but some additional reducing compounds have proved effective in this role also such as hydroxylamine nitrate (HAN) and ferrous sulphamate; stabilising the Pu^{3+} .

Stabilising Pu^{3+} is difficult to achieve, even via addition of the chemicals mentioned above. The radiolytic breakdown of nitric acid produces nitrous acid. Dinitrogen tetroxide, a product of nitric and nitrous acid interactions, may re-oxidise Pu^{3+} to form Pu^{4+} which produces more nitrous acid resulting in an overall oxidation process which is self-catalysing (Nash & Lumetta, 2011, p. 153). Hydrazine nitrate is an example of an additive which acts as a nitrite ion scavenger, removing radiolytically generated nitrous acid and thus preventing dinitrogen tetroxide from forming and subsequently oxidising Pu^{3+} back up to extractable Pu^{4+} (Joyce, 2016, p. 316).

The addition of extra chemicals to ensure the success of the PUREX process is undesirable from a safety perspective, given the possibility of radiolytic degradation into species with behaviour that is difficult to predict. Furthermore, azides formed from hydrazine interactions can be explosive. From a disposal perspective, extra chemical addition also increases the volume of eventual waste. New reprocessing techniques have the potential to greatly improve upon matters such as these because they may be thoroughly designed to achieve maximum efficiency, modelled and tested on the lab-scale before any plant is built.

A description of two more recently developed nuclear fuel reprocessing procedures for which research has been undertaken in the studies presented here, Advanced PUREX, a new reprocessing scheme based on the PUREX process, and i-SANEX, a minor actinide-lanthanide separations scheme that may be used in the treatment of PUREX raffinates, are outlined in Sections 2.4 and 2.5. However, before explaining these processes, the principal knowledge area of interest, mass transfer and chemical kinetics, will be summarised in the following section.

2.3 Mass Transfer and Chemical Kinetics in Actinide and Lanthanide Extraction Systems

2.3.1 Overview

Liquid/liquid extraction processes such as the nitric acid-TBP/OK extraction at the heart of the PUREX process are widely used in the treatment of spent fuel and the waste streams that arise from that treatment. For instance, as well as the separation of uranium and plutonium from dissolved spent nuclear fuel, liquid/liquid extractions may be performed on many of the waste streams of nuclear reprocessing to partition the harmful by-products in nuclear fuel for separate treatment to optimise the burden on nuclear waste repositories.

Quantifying the thermodynamics of an extraction process is a strong basis for demonstrating its feasibility. However, as in chemical processes more generally, kinetics of key steps such as the rate of formation of the extracting complex from its component metal ion and ligands will also play a role – as will the mass transfer of the extracting entity to the aqueous phase-organic phase interface.

For transfer of dissolved species between phases, the most commonly applied model is two-film theory. The first thing to consider in this model is that the immiscible organic and aqueous phases have an area of interfacial contact between them. This area represents the sum of the interfacial area between the two phases. For instance, in the case of two immiscible phases mixed under conditions of high shear usually forming a metastable emulsion, this will be the sum surface area of the droplets of one phase dispersed in the other.

Irrespective of its actual geometry, the region of interfacial contact between two phases can be represented through a simple model of the two phases as shown by Figure 2.3.1, the so-called twin film model. As a result of the transfer of a species from one phase to the other, and prior to the transfer process reaching equilibrium, there will exist regions of concentration polarisation either side of the interface. The region in the phase from which the transferring species is extracted will have a concentration of that species that is depleted with respect to that in the bulk of that phase, whilst the region in the phase that is being extracted into will have a concentration of the transferring species that is elevated with respect to the bulk of that phase. i.e. there exists twin *concentration polarisation layers* at the interface, one on each side – hence the name of the twin film model. If each layer may be considered to be

convection-free, i.e. effectively stagnant, then diffusion will be the only mode of mass transfer in each and they may both be referred to as *diffusion layers*.

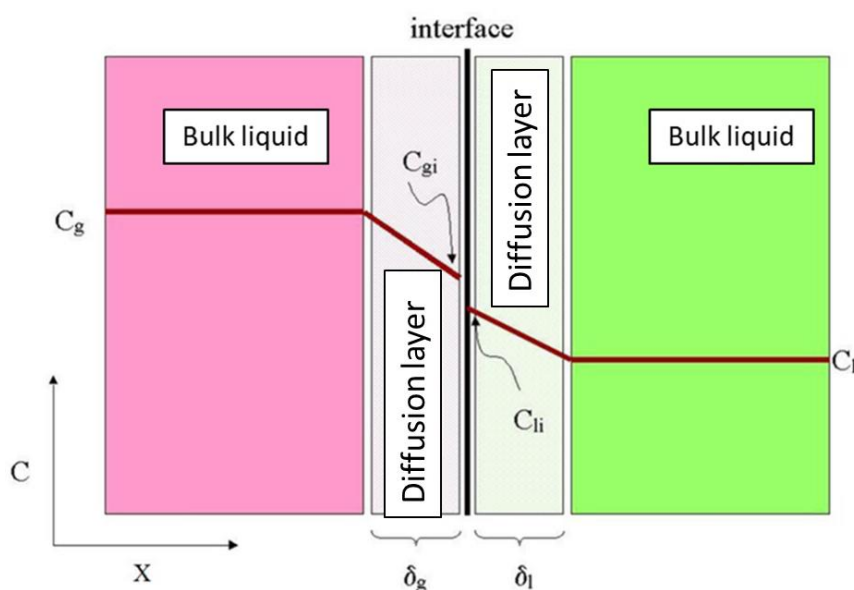


Figure 2.3.1: Diagram of the twin film model of the l/l interface, showing the phase boundary between two phases and the transferring species concentration profile each side of the interface.

As discussed above, in reactive systems, such as the ligand-metal complexation reactions used in actinide and lanthanide partitioning processes, there is another influence on top of diffusive mass transfer which influences the speed of transfer of species between phases; chemical kinetics. These systems are often referred to as mass transfer with chemical reaction (MTWCR) systems.

A MTWCR system may be limited by a combination of chemical kinetics and by diffusive mass transfer. However, if a reaction, which creates a mobile and assimilable species in both of the two-phases, is sufficiently fast, the system could be considered to be diffusion controlled, i.e. the slowest step is the mass transfer over the stagnant diffusion layer of either phase. On the other hand, if the chemical reaction has slow kinetics, or if the diffusion layer thickness is reduced by thorough mixing, thus increasing the concentration gradient and diffusion rate across the film in accordance with Fick's first law, then the system can be considered to be kinetically controlled. A key assumption of this model is that a chemical reaction occurs in the bulk of one phase, with no reactants requiring prior transport from one phase to the other. Such an assumption may *not* be universally applied to the lanthanide and actinide extraction systems; especially in the context of the PUREX, i-SANEX and GANEX

processes considered here, a point we shall return to below. However, the fundamental relationship between mass transfer and chemical kinetics expressed here is essential knowledge when the complexity is increased in later sections of this thesis.

2.3.2 Liquid-liquid Contactor Technology

There are three general kinds of contactor that have found application in the nuclear industry: conventional mixer-settlers, pulsed columns and centrifugal contactors.

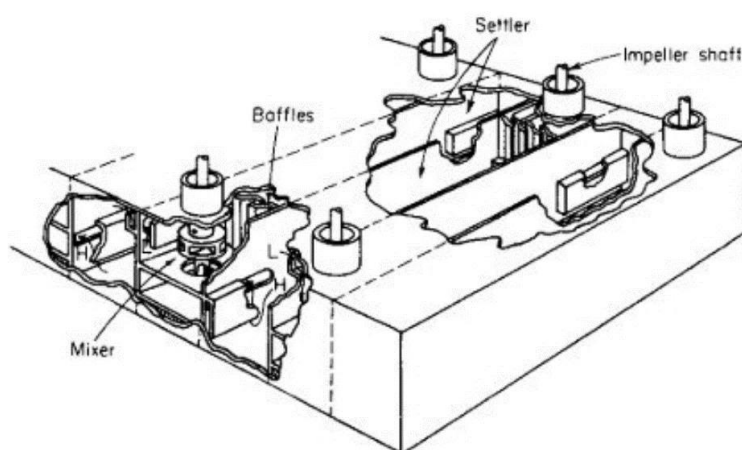


Figure 2.3.2.1: Diagram of a pump-mix box-type mixer-settler (Perry & Green, 2007, p. 1748).

Mixer-settlers of the type shown by Figure 2.3.2.1 operate by pumping the two phases to be mixed, i.e. the aqueous liquor containing the target solutes for extraction and the organic phase containing the ligand that extracts the solute, into a box-shaped mixing space. Following mixing, the resulting metastable emulsion is pumped gently through the baffles into a long settler compartment, shown in Figure 2.3.2.1. Along the length of this compartment, the greater density of the aqueous phase means that it flows along the bottom of the settler, while the less dense organic flows along the top, thus allowing for their routing into separate compartments within the mixer-settler box. The organic phase on the top leaves the settler to enter the mixer directly adjacent on one side and the aqueous phase at the bottom leaves to enter the mixer on the opposite side. In this manner, the organic phase flows through the system in one direction and the aqueous in the other, in counter-current flow. The flow-through speed is slow compared to other contactor technologies because if the pump is

set too fast the phases in the settler may not have time to effectively separate, resulting in less effective overall transfer of solute from one phase to the other.

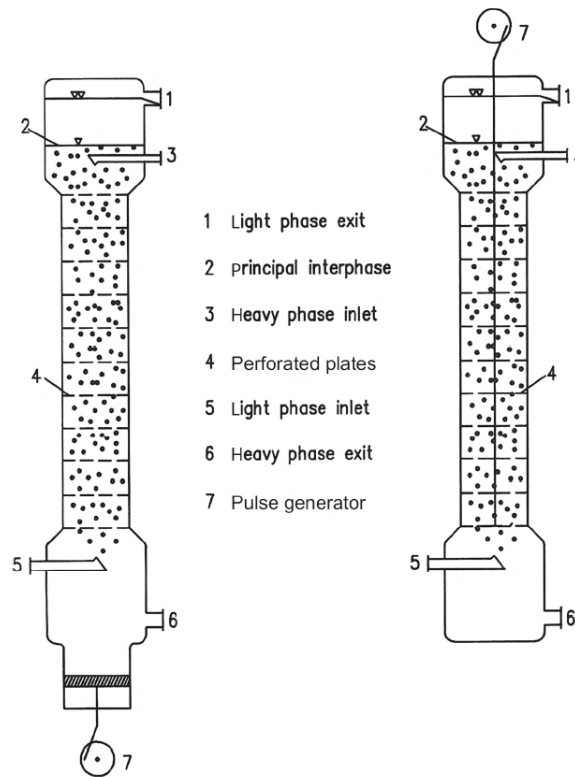


Figure 2.3.2.2: Diagram of sieve tray pulsed columns whereby pulsing is performed on the whole liquid content (left) or the whole plate package (right) (Kislik, 2012).

Pulsed columns, as used in nuclear reprocessing and partitioning, are counter current liquid-liquid contactors whereby the aqueous liquor containing the target solutes for extraction is fed into the top of the column and the light organic phase containing the ligands that may extract those target solutes is fed into the bottom. The less dense organic phase flows up through the aqueous phase and exits at the top whilst the aqueous phase flows downwards and exits at the bottom with both phases passing through multiple plates or sieves to maximise the interfacial contact area. This is shown in Figure 2.3.2.2. The pulsing of the organic phase as it undergoes counter current flow in the column introduces greater shear forces on the fluid across the sieve plates which creates a more efficient droplet formation, aiding extraction efficiency (Theobald, Hanson, Fairweather, & Heggs, 2020).

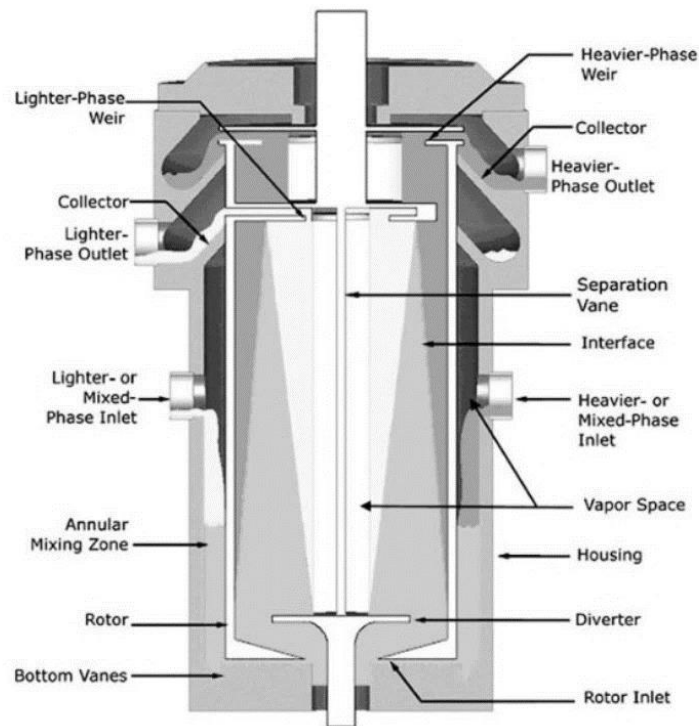


Figure 2.3.2.3: Diagram of a centrifugal contactor/separator (Perry & Green, 2007, p. 1750).

A liquid-liquid system fed into a centrifugal contactor utilises the high shear force manifest in the annular mixing zone between the rotor and housing, shown by Figure 2.3.2.3, to reduce the diffusion path length of the solute being extracted from one phase to the other, in this case the aqueous solute species being extracted from the aqueous liquor by the organic ligand. The centrifugal force inside the rotor, where the metastable emulsion produced during mixing is subsequently fed, increases the driving force for phase separation which is beneficial for liquid-liquid systems where the density difference between the phases is small and where short contact time is needed (Perry & Green, 2007, p. 1749). The denser aqueous phase, forced by centrifugal force to the edge of the rotor, and the less dense organic phase thus displaced and flowing closer to the middle axis of the rotor, both exit by separate weirs at the top of the contactor shown in Figure 2.3.2.3.

There are benefits and drawbacks for each of these categories of contactor, for example a bank of conventional mixer-settlers, shown in Figure 2.3.2.1, the oldest of the three contactor technologies, are simple to operate, with minimal moving parts, but require long residence times and have criticality risks due to the small surface area to volume ratio for neutron escape. In other words, a neutron produced from a dissolved radioactive solute has an increased probability of becoming moderated, causing a fission reaction, because it has a long

pathlength before it exits any one vessel, containing fissile material, in a contactor bank. Mixer-settlers also take up a large area within a nuclear site, ‘in the uranium industry (uranium production and fuel reprocessing) a single mixer-settler may hold as much as 1000m³’ (Van Hecke & Goethals, 2006) which is about a third of the volume of an Olympic sized swimming pool. Additionally, due to the scale of mixer-settlers, they can be more difficult to decommission.

Given the finite area available for the construction of facilities in a licenced nuclear site, a more compact solution than mixer-settlers is desirable from a land efficiency perspective. Pulsed columns, Figure 2.3.2.2, and centrifugal contactors, Figure 2.3.2.3, are more compact contactors which additionally address the criticality risks found in mixer-settlers due to their larger surface area for neutron escape per unit volume, i.e. neutrons are easily lost to the surrounding air between the thin pulsed columns and small centrifugal contactors before they have the required time and volume of water in which the neutrons may become moderated. However, despite the small footprint of pulsed columns, they have a large height which introduces vulnerability to earthquakes and potential aircraft-based terrorist attacks. Centrifugal contactors, which are not as tall as pulsed columns, appear to be the optimal choice in contactor technology, when considering plant footprint, height and criticality risks. However, centrifugal contactors possess more moving parts and mechanisms than the original mixer-settlers, increasing the chances of malfunction, i.e. if there are more parts to a system, there are more parts that may go wrong. The parts themselves may also be radioactive, which introduces further problems when repairs take place. Experience in the operation of centrifugal contactors will eventually reduce the likelihood of malfunctions, but this information regarding best practice must be obtained whilst upholding the key principle of ALARP.

The choice of contactor for a reprocessing plant should be based upon the totality of knowledge about the process it is to perform. Currently, there is not a thorough basis of knowledge regarding the mass transfer and chemical kinetics of proposed next generation reprocessing systems within the commonly used contactor technologies, or indeed in any contactor technology. The kinetics of interfacial transfer coupled with complexation are very poorly understood. Any understanding of the macro-kinetics of mixer-settlers and pulsed columns have been largely empirically derived and based on extraction rates as a function of, for example, shear rates or flow rates, with no genuine micro-scale understanding of the

chemistry and interfacial transfer behaviour. Understanding what takes place during extraction on the micro-scale may directly inform which is the best available contactor technology to deploy. Increasing interfacial area between the phases is desirable for systems with rapid chemical kinetics which are mass transfer limiting, hence pulsed columns and centrifugal contactors should ideally be used.

2.4 Advanced PUREX Process

Recalling the discussion of plutonium in Section 2.1, it is desirable to avoid the production of a pure plutonium stream for reasons of proliferation. As such, there has been work to develop an Advanced PUREX process which addresses this concern (Nash & Lumetta, 2011, pp. 159-161).

The solution which the Advanced PUREX process offers, to prevent the production of a pure plutonium stream, is to allow the bleeding of neptunium and/or uranium, which in spent fuel is largely the non-fissile -238 isotope, into the pure plutonium stream to effectively diminish its ability to fission (Nash & Lumetta, 2011, pp. 159-160). This issue could be avoided altogether should the technology for MOX fuel, with mixed metal salt precursors, become sophisticated enough to allow controllable ratios of U, Pu and even Np to become the constituents of reactor fuel (Nash & Lumetta, 2011, pp. 159-160). However, the technology may not make this a reality for many years to come³.

The alterations in the chemical process of standard PUREX necessary for it to function as an Advanced PUREX process were as follows. In Advanced PUREX the TBP/OK solvent is used in the same manner as standard PUREX to extract the actinides from nitric acid (Nash & Lumetta, 2011, p. 162), however, in Advanced PUREX, the additional ligand AHA (acetohydroxamic acid) or FHA (formohydroxamic acid) is added in the partitioning stages to better manage the redox chemistry (Nash & Lumetta, 2011, p. 163) of U/Pu/Np separations. In Advanced PUREX, whilst the TBP may complex with and extract the U^{4+} species from the nitric acid phase, it is prevented from complexing with the Pu^{4+} ions in nitric acid, which is the tendency of TBP in standard PUREX, because AHA or FHA, a hydrophilic ligand,

³ Of course, heterogeneous MOX, whereby blended powders of pure uranium and plutonium oxides are fabricated into fuel pellets, is already a tested, well established process. However, the technology for mixed uranium, plutonium, and especially minor actinide salt-bearing homogeneous MOX fuel, with no pure metal oxide precursors required, is not yet available on industrial scale.

successfully complexes with Pu^{4+} in solution, so preventing the complexation with TBP and, due to the hydrophilic nature of the Pu^{4+} -hydroxamate complex itself, thus also preventing its extraction from the aqueous nitric acid phase. AHA/FHA may self-hydrolyse in nitric acid to form HAN (hydroxylamine) which is a reducing agent in solution, converting some Pu^{4+} to Pu^{3+} , however since TBP does not selectively extract this valency of plutonium, the process is robust at preventing plutonium entering the uranium output stream and does not require the undesirable reducing and scavenging conditions, mentioned above in Section 2.2, needed to stabilise Pu^{3+} in standard PUREX.

99.8% of the neptunium in standard PUREX is recovered in the uranium purification stages (Nash & Lumetta, 2011, p. 155), however it is possible to engineer the AHA/FHA system so that some portion of it remains in the nitric acid phase with the plutonium. For example TBP may not extract Np^{5+} , therefore ensuring there is sufficient HAN present in solution to reduce Np^{6+} to Np^{5+} would 'poison' the Pu stream with Np, addressing proliferation concerns (Nash & Lumetta, 2011, p. 164).

2.5 i-SANEX and GANEX Processes

A leading candidate process for minor actinide partitioning is the i-SANEX (innovative - Selective Actinide Extraction) process, for which a wide range of models and lab scale experimental data have been generated (Modolo, Asp, Schreinemachers, & Vijgen, 2007; Modolo, et al., 2008; Magnusson, et al., 2009).

The i-SANEX process is a two part liquid/liquid extraction technique which aims to co-extract the trivalent actinides and lanthanides from a PUREX raffinate, shown in the upper part of the flowsheet presented in Figure 2.5.1, leaving the fission products behind, followed by a stripping of the actinides from the lanthanides, shown in the bottom part of Figure 2.5.1 (Modolo, Wilden, Kaufholz, Bosbach, & Geist, 2014, pp. 107-114).

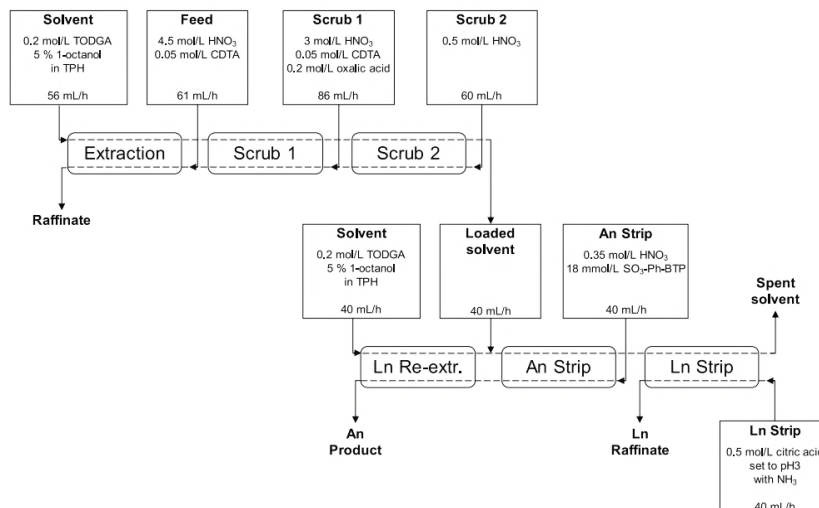


Figure 2.5.1: Technical flowsheet of the i-SANEX process (Modolo, Wilden, Kaufholz, Bosbach, & Geist, 2014, p. 110).

The ‘extraction’, ‘scrub 1’ and ‘scrub 2’ units shown in Figure 2.5.1 are the locations in which mixing and separation of the ligand-containing organic phase and the aqueous nitric acid phase, containing the actinides, lanthanides and fission products, occurs. The main ligand in the solvent feed, TODGA (N, N, N’, N’-tetraoctyldiglycolamide), which has a structural formula shown by Figure 2.5.2, selectively complexes to the trivalent actinides and lanthanides leaving the fission products behind. Some of the fission products have a tendency to become extracted into the organic phase by TODGA also, such as Zirconium, Palladium and Molybdenum, however CDTA and oxalic acid, for Zr/Pd and Zr/Mo, respectively, are added to both the aqueous feed and one of the scrubbing phases to effectively complex to these elements. This prevents TODGA from doing so, thus ensuring that they remain in the aqueous phase (Modolo, Wilden, Kaufholz, Bosbach, & Geist, 2014, p. 109).

The TODGA extraction stage from this previous study was performed using sixteen annular miniature centrifugal contactors with four contactors spanning the ‘extraction’ unit in Figure 2.5.1 (Modolo, Wilden, Kaufholz, Bosbach, & Geist, 2014, p. 110). With this many contactors, this process proved to be very efficient in extracting trivalent actinides and lanthanides, to the extent that an adaptation of the i-SANEX process, the 1c-SANEX (1-cycle SANEX) in which the objective was to extract the actinides in one single cycle, was attempted. This proved feasible but revealed some engineering drawbacks (Modolo, Wilden, Kaufholz, Bosbach, & Geist, 2014, p. 113). Given the high level of mixing in centrifugal contactors, the question remains: would the extraction be as efficient with alternative

liquid/liquid contactors deployed where the contribution of diffusive mass transfer and chemical kinetics to the overall extraction is different? Acquiring answers to this question by exploring the relevance and applicability of the two-film model, outlined in Section 2.3, remains paramount.

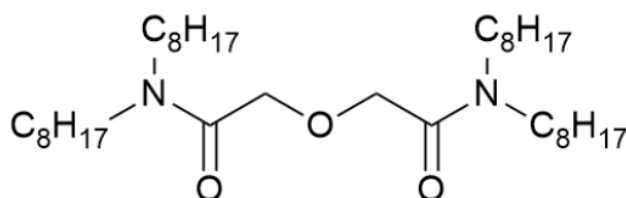


Figure 2.5.2: Structural formula of a TODGA molecule.

Due to the success of the above studies, TODGA has become a key ligand in the EUROGANEX (European Group Actinide Extraction) process which is described by the flowsheet shown on the right hand side in Figure 2.5.3. EUROGANEX refers only to a specific variation of the *second* stage of the overall GANEX process. For all variations of the GANEX process there is a common first stage, which is shown on the left hand side of Figure 2.5.3.

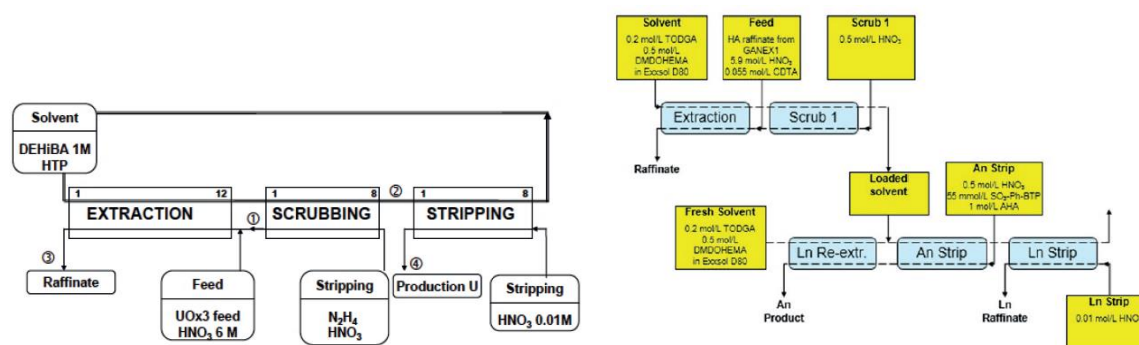


Figure 2.5.3: Technical flowsheets of the first stage of the GANEX process (left), which is common to all GANEX variations, and a particular variation of the second stage of GANEX known as the EUROGANEX process (right) (SACSESS, 2015).

In the first stage of the overall GANEX process, shown by the flowsheet on the left hand side of Figure 2.5.3, only uranium is extracted from the spent nuclear fuel dissolved in 6 mol.dm⁻³ nitric acid into the solvent phase by selective complexation with the organic ligand DEHiBA.

The raffinate from the ‘extraction’ unit produced in the first GANEX stage becomes the feed for the second GANEX stage, which in this case is the EUROGANEX process.

The EUROGANEX feed contains plutonium, neptunium, americium and curium along with additional lanthanide isotopic elements and other fission products. The ‘extraction’ and ‘scrub 1’ stages shown in the right hand flowsheet of Figure 2.5.3 utilise a solvent phase containing TODGA and DMDOHEMA to extract all actinides and lanthanide species from the loaded nitric acid feed, leaving the fission products behind. Following this, the actinide and lanthanide loaded solvent is contacted in the ‘An strip’ stage with a low acidity nitric acid phase containing SO₃-Ph-BTP and AHA which selectively extracts the neptunium, plutonium, americium and curium. AHA in the nitric acid phase forms hydrophilic complexes with the tetravalent actinides (Carrot, et al., 2014) preventing their re-extraction by the fresh TODGA/DMDOHEMA solvent phase used in the ‘Ln re-extr.’ stage which assists in the re-extraction of the lanthanides that are partially stripped from the loaded solvent by SO₃-Ph-BTP. The remaining lanthanides in the organic phase are then finally stripped into a low acidity nitric acid phase in the ‘Ln strip’ stage. Thus, the overall GANEX process is designed to produce a pure uranium stream, a mixed stream containing neptunium, plutonium, americium and curium, a mixed lanthanide stream and a fission product stream.

TODGA-containing (and indeed most diglycolamide-containing) solvents, such as are used in the i-SANEX and EUROGANEX processes, are prone to third phase formation when in contact with nitric acid phases containing metal ions, especially at elevated concentrations (Weßling, Müllich, Guerinoni, Geist, & Panak, 2020). The third phase consists of non-metal-bearing TODGA reverse-micelles. The phenomenon can occur when four TODGA molecules complex around a polar core of up to three protons and/or water molecules, components of the acidic aqueous phase, forming small, spherical aggregates with short-range attractive forces (Nave, Modolo, Madic, & Testard, 2004). The density of the third phase is less than the that of the aqueous phase but greater than that of the organic (Ravi, Mishra, Murali, Desigan, & Pandey, 2021), thus in a fully settled system the third phase would settle between the aqueous and organic phases. This is a problem because the interface between the trivalent actinide and lanthanide bearing aqueous phase and the extracting organic phase, over which efficient mass transfer may proceed, ceases to be manifest whilst a non-extracting third phase containing TODGA reverse-micelles lies between them. Additionally, the overall liquid/liquid contact process is specifically designed, at the tail-end, for the separation of *two*

immiscible liquids, not three. As such, either, or both, of the two expected phases may be contaminated by droplets of the third phase, which would require a further separation. Furthermore, the maximum load of the overall i-SANEX or EUROGANEX process may be diminished if a quantity of complexing TODGA is lost to third phase formation. Despite the issues arising from third phase formation, suitable preventative measures have been found. Common phase modifiers added to suppress third phase formation include TBP, lipophilic alcohols like octanol and mono-amides (Weßling, Müllich, Guerinoni, Geist, & Panak, 2020). In the studies for this thesis 5% octanol by volume is added routinely to TODGA-bearing organic phases for this reason.

Given the general utility of diglycolamide ligands in the SANEX and GANEX families of extraction processes, the work presented here has focused on TODGA with a view to experiments on the other ligands present in these processes, such as DMDOHEMA and DEHiBA, being pursued once the baseline behaviour of TODGA has been fully established.

2.6 Literature Survey of Mass Transfer and Chemical Kinetics

The effects of mass transfer and chemical kinetics in liquid/liquid extraction systems may be interrogated through a range of closely related experimental techniques. These techniques include the Single Drop method, microfluidics, the Nitsch Cell, the Rotating Membrane Cell (RMC) and the Rotating Diffusion Cell (RDC). The last of these methods, the RDC, is deployed here due to its advantages over the other three techniques when applied to the systems of interest in this thesis. Following are brief overviews of the alternative methods.

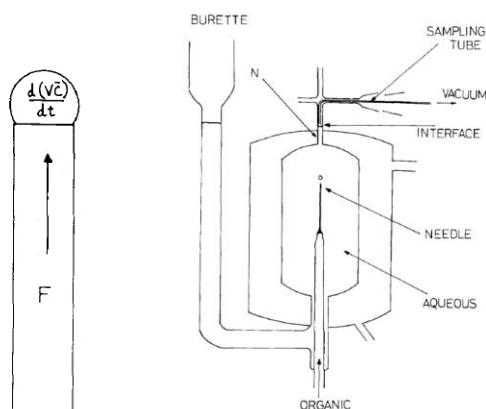


Figure 2.6.1: Diagram of the needle tip (left) and apparatus (right) of the Single Drop method for studying mass transfer and chemical kinetics. (Hughes & Zhu, 1985).

The Single Drop method (also known as the Growing Drop method) interrogates the transfer of a solute from a bulk liquid phase into a single droplet of another phase suspended into the bulk liquid phase from a needle tip. A typical experimental setup of the Single Drop method is shown by Figure 2.6.1. The advantage of using a single droplet of one phase dispersed in another is that the interfacial surface across which transfer occurs is well defined and spherical in nature, which is analogous to the geometry of the interfaces encountered in liquid/liquid contactors (Hughes & Zhu, 1985). The example shown in Figure 2.6.1 is the Rising Single Drop method whereby the light organic phase rises through the denser aqueous phase, however the opposite setup has also been studied, the Falling Single Drop, whereby a droplet of aqueous phase falls through the bulk organic phase (Lélias & Miguiditchian, 2015). Whilst the spherical diffusion field associated with a droplet means that diffusive mass transfer is well controlled, understood and, indeed, can be varied to some extent by use of different sized needle tips to change the radius of the extruded droplet, there is no possibility of investigating mass transfer under high shear conditions. High shear conditions are encountered in all types of contactor technology described in Section 2.3.2 and result in bulk phase turbulence and convective mass transfer. It is not possible to investigate these conditions in the Single Drop method as such conditions will disrupt the well-defined interfacial geometry which is essential to the interpretation of the gathered data.

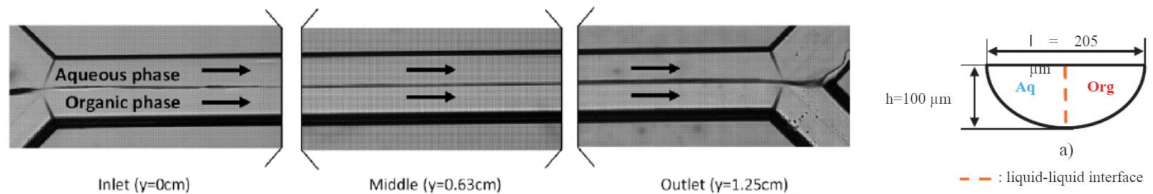


Figure 2.6.2: Microscope image of a typical microfluidic liquid/liquid extraction capillary (left) and cross sectional diagram of the manifest two-phase flow (right) (Corne, et al., 2019).

Microfluidic liquid/liquid extractions are conducted in capillaries in the order of 100-200 μm in diameter. By conducting the extractions on such small scales, the Reynolds number, derived from the fluid motion through the capillary, becomes so small that laminar flow can be maintained at high flow rates. This ensures that the interfacial area of contact between the two phases remains well defined and may not break up and form droplets or emulsions due to turbulence. A microfluidic liquid/liquid system of this nature is shown by Figure 2.6.2. There is another incarnation of this method whereby droplets or ‘slugs’ of one phase are dispersed along the capillary within which another phase is flowing, rather than the two phases flowing parallel. Though the geometry and nature of the extraction may be different between these two microfluidic methods, the key similarity between all extractions performed using a capillary is that, due to laminar flow being manifest, the geometries of the extracting entities may be well defined and easily controlled (Corne, et al., 2019). Low shear convective mass transfer may be interrogated in microfluidic experiments, however, similar to the Single Drop method, high shear convection and bulk phase turbulence encountered in typical contactors may not be, which is a key disadvantage to the microfluidic technique.

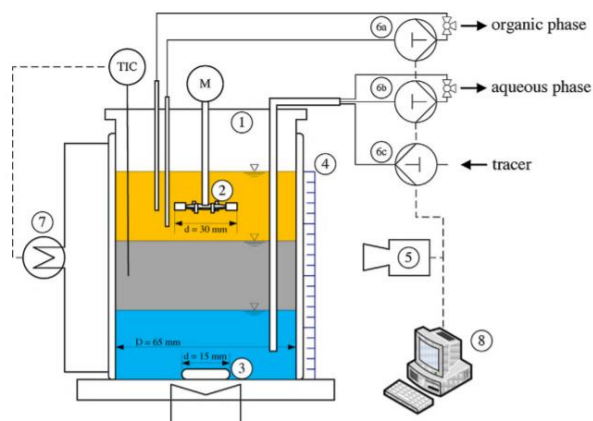


Figure 2.6.3: Diagram of a Nitsch Cell investigating a three-phase system (Paul, Schulz, & Kraume, 2015).

The Nitsch Cell is a stirred stationary cylindrical vessel in which multiple immiscible liquids may be held with the heavy phases sinking to the bottom and the lighter phases rising to the top. The interface between phases is well defined as the circular cross-sectional area of contact between the phases; the same as the cross-sectional area of the cell itself. Transfer of species from one phase to another in a Nitsch Cell occurs through the flat, circular, unsupported interfaces between phases. An advantage of the Nitsch Cell is that it is able to interrogate systems possessing more than two liquid phases, which is useful in systems which exhibit third phase formation as described in Section 2.5. A disadvantage, in common with the other techniques mentioned above, is that only low shear conditions may be reproduced because, under high shear conditions, the same conditions encountered in a liquid/liquid contactor, the unsupported interfacial geometry will be disturbed. This is because the surface tension between two phases, which keeps the interface uniform under low shear conditions, is overcome by the force of fluid flow directed towards the membrane under high shear conditions and would encourage droplet formation at the interface. A disruption of the interface in this manner is undesirable as it alters the overall surface area of transfer between one phase and another and ultimately does not allow mass transfer and interfacial kinetics to be accurately interrogated. A diagram of a typical Nitsch Cell is shown by Figure 2.6.3.

The Rotating Membrane Cell (RMC) consists of a membrane, which is saturated with either a metal-loaded aqueous or metal-loaded organic phase, mounted on the end of a rotating cylinder that is submerged in a larger vessel containing the metal-free other phase. The

interfacial area over which mass transfer can be studied is thus the porous outer surface area of the mounted membrane. An example RMC apparatus is shown in Figure 2.6.4.

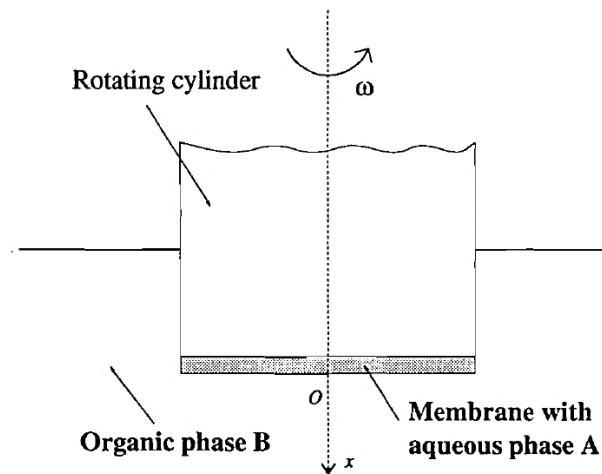


Figure 2.6.4: Diagram of a Rotating Membrane Cell (RMC) (Simonin & Weill, 1998).

Unlike the three methods described above, the RMC is able to recreate a range of shear conditions in the fluid phase situated in the outer vessel as the rotation speed of the inner cylinder is varied, from low shear, diffusion limiting conditions, to high shear kinetic control. The high shear conditions encountered in a contactor may be produced at the highest rotation speeds whilst maintaining the geometry of the liquid/liquid interface due to the fact that the interface is supported by the mounted membrane filter. The main disadvantage associated with the RMC technique is that the liquid phase absorbed into the membrane mounted on the inner cylinder is of such small volume that one may only accurately interpret the diffusive and chemical kinetic transfer of species *out* of it, not *into* it because of the much smaller solute load the smaller, membrane mounted, phase is capable of supporting. Furthermore, in liquid/liquid contactors, the volume of each phase undergoing mixing is typically equivalent, thus the high shear conditions are manifest in *both* phases undergoing contact, not just one. The phase absorbed into the membrane in the RMC will not be undergoing shear conditions akin to the phase located in the outer vessel. It is far more likely that no hydrodynamic flow is taking place at all within the membrane due to the tortuosity of the inner membrane environment and because such a small amount of fluid is residing within it. Therefore, though the RMC is a technique with greater applicability to the study of the mass transfer in industrial-scale high shear contactors than the techniques described before it, it is best suited

to the interrogation of species transfer in one direction with contactor-appropriate shear conditions being reproduced in one phase only.

All of the shortcomings of the above techniques are addressed by the RDC. The Rotating Diffusion Cell (RDC), which is the primary experimental technique employed in the studies presented in this thesis, maintains a supported interface between two liquid phases via the use of a defined area porous membrane. The membrane is located at the base of a cylindrical vessel, in which one phase is contained, which is submerged into a larger cylindrical vessel, where the other phase resides. The volume of each phase is typically 10-100 cm³. The volumes of the two phases allows for solute loads equivalent to those encountered in contactors and furthermore the transfer of species in both directions, if applicable, may be studied. As with the RMC, the inner cylinder of the RDC is mounted within a pulley system which allows for the rotation of the inner cylinder whilst the outer cylinder remains stationary. The RDC apparatus is shown in Figure 2.6.5.

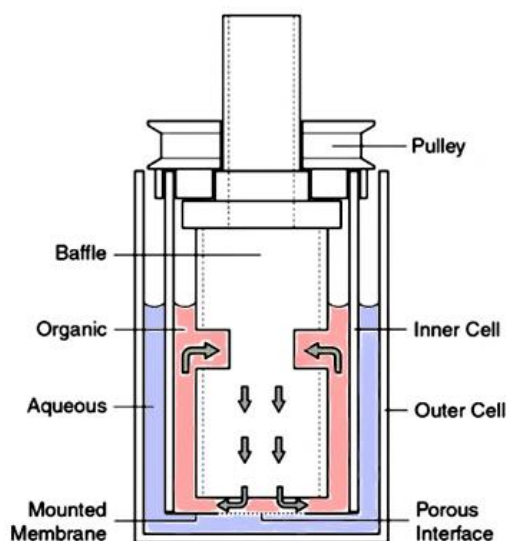


Figure 2.6.5: Diagram of the Rotating Diffusion Cell (RDC) (Bromley & Boxall, 2015).

Varying the rotation speed of the RDC allows for a greater range of mass transfer and chemical kinetic conditions to be studied compared to the low shear-dependent techniques described above; from low shear, diffusion limiting, to high shear chemically limiting extractions. Furthermore, since the interface is supported by a porous membrane, similar to the RMC, much higher convective shear conditions, which are akin to those encountered in centrifugal contactors may be achieved at the fastest rotation speeds without affecting the defined circular interfacial area between phases. Similar shear conditions in

previous low-shear techniques are either not possible, such as in the microfluidic systems, or would result in the changing of the geometry of the defined interface as it becomes disturbed by fluid turbulence, e.g. as described above for the Nitsch Cell.

In the studies presented in this thesis, the extracting organic phase within the RDC, which consists of an organic solvent containing a ligand, TBP or TODGA, for interrogation of PUREX or i-SANEX/EUROGANEX systems respectively, is housed in the inner cylinder. The aqueous phase, consisting of either tetra- or tri-valent metal ion salts dissolved nitric acid, the solutes to be extracted, reside in the outer cylinder. The concentration of the metal ion in the inner rotating vessel containing the organic phase is measured over time which indicates the rate of overall extraction.

As aforementioned, the rotation speed of the RDC is a unique experimental control which may be used to interrogate a range of MTWCR regimes. RDC rotation speed allows the switching between these regimes due to its influence on the thickness of the effective diffusion layer in the aqueous nitric acid phase on the outer surface of the interface. Due to viscosity effects, the rotating disc-shaped membrane drags a layer of solution around with it when it rotates. Within the frame of reference of the membrane, this layer of solution appears as a convection-free, effectively stagnant layer through which the only mode of mass transfer that obtains is diffusion. Such a layer may be equivalent to the diffusion layer as described in the twin film model of the interface between the two phases of a liquid/liquid extraction system shown in Figure 2.3.1.

To approximate the thickness of this effectively stagnant aqueous diffusion layer in the RDC, the Levich Equation may be used which is shown in its simplest form by Equation 2.6.1 (Levich, 1962), where X_D is the diffusion layer thickness, ω is RDC rotation speed in Hz (or s^{-1}), ν is the kinematic viscosity in $m^2.s^{-1}$, and D is the diffusion coefficient in $m^2.s^{-1}$ of a given solute travelling through the aqueous phase. The constant 0.643 is dimensionless.

$$X_D = 0.643\omega^{-\frac{1}{2}}\nu^{\frac{1}{6}}D^{\frac{1}{3}} \quad (2.6.1)$$

The outer vessel containing the aqueous phase is not stirred conventionally using magnetic or mounted stirrers encountered in a Nitsch Cell, shown in Figure 2.6.3. Instead, the high shear hydrodynamic flow regime, convective in nature, is brought about by the presence of the rotating surface of the membrane mounted on the inner cylinder. As mentioned above the

diffusion region in the aqueous phase, situated in the outer RDC vessel, is considered effectively stagnant with respect to the membrane surface i.e. the region of the liquid that comprises the diffusion layer can, to a first approximation, be considered to rotate *with* the membrane. Beyond this there is a fluid region referred to as a convection layer in which laminar convective flow is manifest. Both the convection and diffusion layers are enveloped within what is termed the *hydrodynamic* layer which has a thickness X_H . Beyond this laminar convection region, the bulk liquid is well mixed. Figure 2.6.6 is a diagram showing the interrelationship between the components of the hydrodynamic layer and the well mixed bulk liquid phase, as described above.

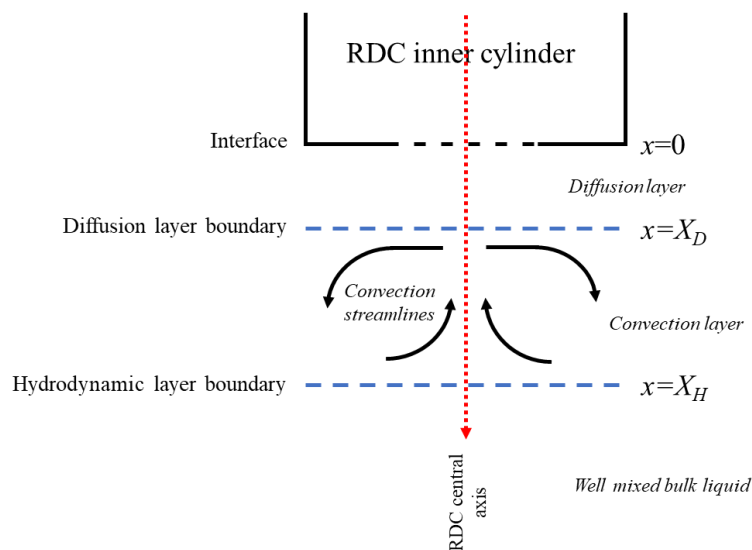


Figure 2.6.6: Diagram of the hydrodynamic layers near to a rotating disc according to Levichian hydrodynamic theory.

Considering the *diffusion* and *convection* layers as discrete regions in the RDC is a simplification useful in modelling, however, in reality, diffusive *and* convective transfer is *continuous* throughout the entire hydrodynamic layer. However, at distances close to the interface, i.e. distances less than X_D , diffusion of a given solute through the aqueous phase dominates its motion, whereas beyond X_D , but at distances less than X_H , convection is dominant. Due to the nature of X_D as an *effective* diffusion layer, species in solution, which possess different diffusivities, will be associated with different effective diffusion layers, X_D , as exhibited by the general nature of the D in Equation 2.6.1. Thus, the motion of a more diffusive solute in the aqueous phase, for example, will be governed by diffusion a much greater distance, X_D , *into* that phase than a solute that is less diffusive. This phenomenon will

become an important factor to take into consideration in later sections of this thesis. The diffusivity of a solute depends on the atomic radius of a single molecule of the solute, r , the dynamic viscosity the liquid phase it is moving through, μ , and the temperature of the system, T . The properties above are interrelated by the Stokes-Einstein relation, Equation 2.6.2, which will also be drawn upon in later sections of this thesis. k_B in Equation 2.6.2 is the Boltzmann constant.

$$D = \frac{k_B T}{6\pi\mu r} \quad (2.6.2)$$

The hydrodynamic theory of Levich was derived to describe the flow of liquid that obtains at the surface of, and within the hydrodynamic layer near to, a generic rotating disc – in the specific case of the RDC, the rotating disc is comprised of the RDC's membrane. Levich's model may be summarised as follows. In the convection layer, fluid incident on the rotating disc/membrane surface at distances just beyond the diffusion region, X_D , flows outwards in a radial direction due to the influence of centripetal force. Thus, the fluid closer, radially, to the centre of the circular disc/membrane flows radially outwards to the edge, displacing the fluid there. This fluid at the edge of the disc/membrane, in turn, is now displaced further both axially and radially within the cell containing the liquid. Eventually, in a convective motion, it flows full circle and replaces the initially displaced liquid, close to the centre, both radially and axially, of the rotating membrane. Thus, there is a continuous axial/normal flow in the perpendicular direction *towards* the interfacial membrane when the inner cylinder of the RDC is rotated. Streamlines to illustrate the convective transfer taking place in the RDC are shown in Figure 2.6.6.

Speed functions of the fluid on the outer surface of the rotating disc in the radial, axial and tangential directions as a function of distance normal to the membrane surface are shown in Figure 2.6.7. There are limits to these Levichian assumptions as found in computational fluid dynamics (CFD) models of a rotating disc system. These CFD models predict that conditions further into the bulk aqueous phase, away from the interfacial membrane surface, do not accurately concord with Levichian hydrodynamic theory (Mandin, Fabian, & Lincot, 2006). However, as will become clear below, only distances very close to the liquid/liquid interface are considered in the work presented here.

The inner cylinder of the RDC containing the organic phase adopts an enforced convective flow regime which is also pseudo-Levichian in nature. However, due to the presence of the walls of the inner cylinder, a feature not present in Levich's hydrodynamic theory, a static baffle is included in the design of the RDC, shown in Figure 2.6.5, to ensure that when the fluid flows outwards radially, and when flow is stopped by the inner cylinder wall, the fluid must flow up between the outer wall of the baffle and the inner wall of the vessel. Then, the fluid flows through the hole in the top of the baffle, shown in Figure 2.6.5, and finally down the centre of the baffle, axially, the whole system adopting a convective motion similar to the fluid in the outer vessel.

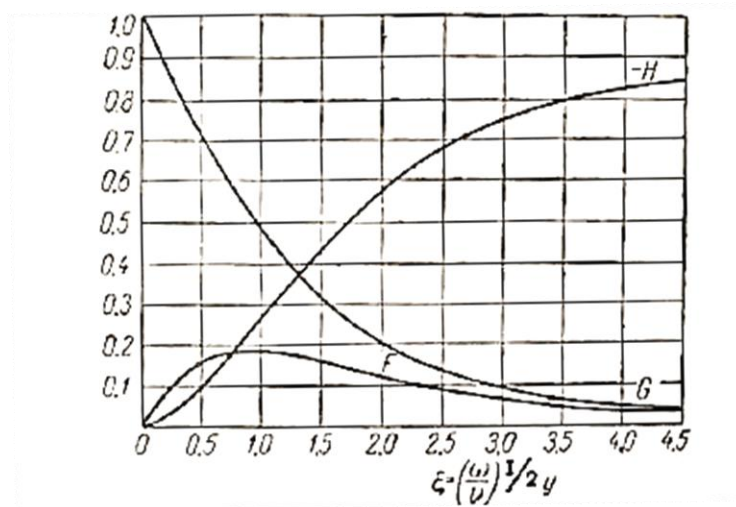


Figure 2.6.7: Normalised Levichian speed functions of a fluid in the convection region near to a rotating disc where F , G and $-H$ are normalised dimensionless parameters related to the radial speed, the tangential speed and the axial speed respectively. ξ is dimensionless and is a function of ω and ν , which are rotation speed and viscosity respectively, and y , the normal distance from the surface of the rotating disc (Levich, 1962).

The level of control available and the firm basis of knowledge in terms of the hydrodynamic conditions in a liquid/liquid extraction system makes the RDC a common choice for studying the mass transfer and chemical kinetics of two-phase chemical systems, especially if these chemical systems are intended to be scaled up industrially using the contactor technologies described in Section 2.3.2. Table 2.6.1 contains a selection of key publications in which the RDC has been used in the measurement of interfacial transfer kinetics, indicating the specific chemical systems studied and the key findings – most especially the observed dependence of the rate of extraction on the membrane rotation (column 3 of Table 1.7.6), the rate

determining step of the extraction (column 4) and the locus of the reaction between extracted metal ion and extracting ligand (column 5). Table 2.6.1 also lists three RMC experiments (columns highlighted in light blue) which have been included due to the similarities between their extraction systems and those studied for this thesis.

Table 2.6.1: Summary of relevant literature reports on the use and modelling of rotating and non-rotating RDC-based systems in the study of liquid-liquid extractions and other interfacial processes. The cells shaded blue are instances of the RMC technique being used.

Reaction and system studied	Authors	Rotation speed (ω) dependence	Rate determining step	Location of reaction
Reaction: hydrolysis Reactants: methylbenzyl chloride System: water/isopropyl mirtrate	(Albery, Couper, Hadgraft, & Ryan, 1974)	Proportional to $\omega^{\frac{1}{2}}$	Diffusion	Interface
Reaction: acid dissociation Reactants: hexanoic acid System: water/isopropyl hexane	(Albery, Burke, Leffler, & Hadgraft, 1976)	Proportional to $\omega^{\frac{1}{2}}$	Diffusion	Interface
Reaction: acid dissociation Reactants: ethanoic acid System: water/isopropyl mirtrate	(Albery, Burke, Leffler, & Hadgraft, 1976)	Proportional to $\omega^{\frac{1}{2}}$	Diffusion	Interface
Reaction: extraction Reactants: Cu(II)/hydroxynonylbenzaldehyde oxime System: water/n-heptane	(Albery, Choudhery, & Fisk, 1984)	Proportional to $\omega^{\frac{1}{2}}$	Mixed control; chemical reaction and diffusion	Interface
Reaction: extraction Reactants: Fe(III)/methyloctadecyl amine/TBP System: water/octane	(Meng, Yu, & Chen, 1996)	Proportional to $\omega^{\frac{1}{2}}$	Chemical reaction	Interface
Reaction: extraction Reactants: Th(IV)/TBP System: water/dodecane	(Horner, et al., 1980)	Not studied	Chemical reaction	Interface
Reaction: extraction Reactants: Zn(II)/D2EHPA System: water/heptane	(MacLean & Dreisinger, 1993)	Proportional to ω	Diffusion	Interface
Reaction: extraction Reactants: Cu(II)/salicylaldehyde oxime System: water/ CCl_4	(Rod, Strnadová, Hančil, & Šír, 1981)	Stagnant system	Mixed control; chemical reaction and diffusion	Aqueous phase
Reaction: extraction Reactants: Cu(II)/LIX64N (mixed hydrophobic oxime) System: water/kerosene	(Hughes & Rod, 1984; Rod, Strnadová, Hančil, & Šír, 1981)	Stagnant system	Mixed control; chemical reaction and diffusion	Aqueous phase
Reaction: extraction Reactants: Cu(II)/D2EHPA & Cu(II)/hydroxyoximes System: water/heptane and water/toluene	(Hughes & Kuipa, 1996)	Constant ω	Mixed control; chemical reaction and diffusion	Aqueous reaction layer 0.03-0.7mm thick
Reaction: extraction Reactants: acetic acid/isopropyl myristate, Ni(II)/D2EHPA & Zn(II)/D2EHPA System: HCl/IPM and HCl/n-dodecane	(Simonin & Weill, 1998)	Proportional to ω	Mixed control; chemical reaction and diffusion	Interface
Reaction: extraction Reactants: Eu(III)/DMDBTDMA & Eu(III)/DMDOHEMA System: HNO_3 /TPH	(Simonin, Perrigaud, Perrigaud, & Vu, 2014)	Not studied	Diffusion	Interface
Reaction: extraction & stripping Reactants: Eu(III)/TODGA System: HNO_3 /TPH with 5% octanol	(Simonin, Boxall, & Lelias, 2015)	Proportional to ω	Mixed control; chemical reaction and diffusion	Interface
Reaction: extraction & stripping Reactants: Eu(III)/TODGA & Am(III)/TODGA System: HNO_3 /TPH with 5% octanol	(Simonin, Boxall, & Lélías, 2019)	Proportional to ω	Mixed control; chemical reaction and diffusion	Interface

The literature in Table 2.6.1 predominantly reports a *direct* dependence of extraction rate on membrane rotation speed or square root of rotation. Furthermore, the coupled hydrodynamic-

chemical kinetic models for the systems of Table 2.6.1 all assume that the key complexation occurs either directly at the aqueous-organic interface or in the bulk solution of one of the two phases involved. Some studies also predict a reaction inside the membrane used in rotating cell systems to provide a stable interface between the aqueous and organic phases.

The specific chemical system of interest presented and expanded upon in this thesis, which was studied by Bromley *et al*, is TBP extraction of Ce(IV) giving insight into the PUREX process (standard and Advanced) (Bromley & Boxall, 2015). Bromley *et al* reports an *inverse* dependency of extraction rate with RDC rotation speed (Bromley & Boxall, 2015). This trend diverges from traditional two-film theory briefly outlined in Section 2.3, which would predict a *direct* dependence of extraction rate on rotation speed and this is what is widely encountered in the literature shown in Table 2.6.1.

Recalling the discussion in Section 2.3, where interfacial transfer phenomena were introduced, typically the diffusion layer acts as a region through which reactants must diffuse from the interface to the bulk phase and visa-versa. The stagnant diffusion layer thus becomes a concentration depletion and emergence region, in the case of reactants and products, respectively. The fundamental principle of two-film theory described above results in rotating cell extraction behaviour as per the findings overwhelmingly shown by Table 2.6.1. In both the RDC runs previously conducted in these laboratories by Bromley *et al*, and in the runs reported in this thesis, the ligands are sparingly soluble in the bulk aqueous phase, where the reactions conventionally occur. This theoretically rules out the interface as the *sole* reaction zone because the reactants have the potential to migrate from the organic phase into the acid/aqueous phase containing the metal ion. Furthermore, as encountered in Table 2.6.1, a predominantly interfacial reaction results in direct dependence of extraction rate on RDC rotation speed, which is not encountered by Bromley *et al*, thus an interfacial locus of complexation between metal ion and ligand must not be dominant – and indeed, may not manifest at all. TBP and TODGA, are soluble in the aqueous nitric acid phase at concentrations of $1.46 \text{ mmol.dm}^{-3}$ for TBP (Velavendan, et al., 2013) and $0.042 \text{ mmol.dm}^{-3}$ for TODGA (Sasaki, Sugo, Suzuki, & Tachimori, 2001). However, the values of the ligand solubilities are small compared to the 10 mmol.dm^{-3} of metal ion present in the nitric acid (Bromley & Boxall, 2015) and as such the bulk aqueous phase is also unlikely to be the principal reaction zone due to the high levels of mixing and thus dilution of the migrating ligand within it. This leaves the aqueous diffusion region, in between the interface and the

bulk aqueous phase, as a potential locus of complexation. Due to the above considerations regarding species solubility, the aqueous diffusion region is hypothesised to be the principal zone where aqueous metal ions and the organic ligands meet one another, undergo complexation, and are then subsequently extracted into the organic phase.

None of the previous literature studies model the response of the RDC under conditions where the complexation event occurs in the diffusion layer apart from the study by Hughes and Kuipa referenced in Table 2.6.1. However, this study was not concerned with the effects of varying RDC rotation speed, thus it is not possible to draw a comparison with the work presented here. We shall return to this point below.

Systems directly analogous to the TODGA systems under investigation in this thesis have been studied by Simonin *et al* as indicated in Table 2.6.1. These studies involved use of the RMC and are indicated as such. Two types of RMC experiment are conducted by Simonin *et al*. Firstly, TODGA extractions of Eu(III) or Am(III) in nitric acid were performed, with the aqueous phase absorbed into the rotating membrane and the organic phase in the stationary outer vessel; the opposite configuration to the RDC setup used by Bromley *et al* and used in the more recent studies undertaken for this thesis. Secondly, stripping experiments were performed whereby previously extracted Eu(III) or Am(III) in an organic phase containing TODGA is absorbed into the membrane and the outer vessel contains a low acidity nitric acid phase containing either SO₃-Ph-BTP or glycolic acid to *strip* the metal ion from the organic phase. This second configuration is akin to the RDC experiments of interest here, with the organic in the rotating membrane and the stationary aqueous phase beyond it in the outer vessel, however the direction of transfer of the metal ion is reversed since it is a stripping experiment and not an extraction. Thus, the former of the experiments described above, despite its phase inversion, is of more relevance to the TODGA-based extraction studies of interest here. Despite the drawbacks of the RMC in terms of its lack of ability to interrogate extraction process with *both* phases under high shear conditions, its use of a small volume membrane significantly reduces the amount of expensive ligand required in some experiments. This may not be an advantage for extractions, for which a larger volume of the organic phase containing the ligand is housed in the outer vessel but is highly advantageous when a much smaller volume of the same phase is absorbed into the membrane during stripping experiments.

In the RMC setup by Simonin *et al*, TODGA, which is known to migrate into the aqueous phase to undergo complexation, as is anticipated given its solubility, will not react within a Levichian aqueous diffusion region brought about by the hydrodynamics of a rotating disc but will be subject to a different set of forces acting within the membrane in which it is contained. If the main complexation occurs in the aqueous diffusion layer, which if present at all will be manifest *within* the membrane, then the rotation of the RMC will not vary the thickness of this layer as it does in the RDC. However, it *will* vary the rate at which fresh ligand is supplied to the aqueous phase in the membrane to become absorbed into it. Following absorption, the ligand complexes with the metal within the membrane then desorbs, returning to the organic phase as a complex. If the complexation event is not rate determining, then the overall extraction will be controlled by the convection/diffusion of the ligand in the organic phase, which can be described by Levichian hydrodynamics. Thus, the faster the rotation speed, the smaller the thickness of the diffusion layer, by an inverse square root relationship in accordance with Equation 2.6.1, and the faster the rate of supply of ligand to the membrane. This will lead to an extraction rate *directly* proportional to the rotation speed which is what is indeed observed in RMC studies by Simonin *et al*, but not in RDC studies by Bromley *et al*. Therefore, the literature produced by Simonin does not offer a direct comparison with the work presented here, even though the same extraction system is being investigated. Furthermore, the *direct* dependence of extraction rate on RMC rotation speed does *not* contradict the *inverse* dependence found in the RDC work since the two experimental setups are different in the manner described above; both findings could be valid.

This created the fundamental investigation area of this work. The question posed is which models can be found or derived to predict the extraction inverse dependency on rotation speed reported here and how can validity be proven. Ultimately, what can be deduced from this literature review is that RDC studies conducted in the manner of the work presented here represent a novel variation in operating conditions and resultant data. This in turn presents a challenge to adopt a new way to interpret extraction without drawing from two-film theory in the conventional manner.

2.7 Scope of the Thesis

In this thesis, the principal experimental work has investigated the mass transfer and chemical kinetics of tetra- and tri-valent metal ion extractions performed using TBP and TODGA, respectively. The former is the key ligand in the existing PUREX process, and the latter is the key ligand in the newer i-SANEX and EUROGANEX systems. Studies of the established TBP system were conducted primarily to inform RDC model development, although new values for unknown constants relevant to the lanthanide extractions are obtained. Although PUREX, i-SANEX and EUROGANEX are processes for extracting radioactive isotopic elements such as plutonium, americium and curium from nitric acid, the work described here is conducted on non-active simulants for reasons of radiological safety.

Chapter 3: Experimental

3.1 The Rotating Diffusion Cell Method

The Rotating Diffusion Cell (RDC) utilised for the studies shown here is a compartmental diffusion apparatus consisting of two concentrically arranged solution vessels separated by a defined area membrane filter. The range of rotation speeds which the RDC is capable of is 1-10 Hz. The inner rotating cylinder is made of piece of Perspex piping with an internal diameter of 45 mm and a wall thickness of 2.0 mm. The outer cylinder is a standard Pyrex 250 cm³ laboratory beaker. In all experiments performed here as well as the data gathered by Bromley *et al*, an organic phase volume of 35 cm³ and an aqueous phase volume of 75 cm³ were used. The equalisation of the liquid levels of both phases is necessary during operation to avoid a hydrostatic pressure difference becoming manifest across the membrane.

The membrane attached to the base of the inner cylinder is a GSWP04700 nitrocellulose membrane filter, with a 47 mm diameter and pore size of 0.22 μm , made by Millipore, purchased from Merck (Gillingham, Dorset, UK). It is attached to the base of the inner cylinder by pipetting a small quantity of dichloromethane along the rim of the cylinder causing the plastic to sparingly dissolve in the solvent and begin to polymerise. The membrane is placed on the still wetted rim of the cylinder and patted down with a gloved finger ensuring the polymerisation process effectively glues the membrane's circular edge to the rim of the cylinder. Once the cylinder rim is dry, the membrane adhesion to the surface of the plastic cylinder rim is inspected and any gaps are filled by re-applying small amounts of dichloromethane followed by pressing down, again, with a gloved finger.

Once the membrane is attached, a central, circular, defined area interface is produced via selectively collapsing the outlying membrane pores with a solvent of 1,4-dioxane (33%), 1,2-dichloroethane (33%), hexane (33%) and water (1%). This solvent can be applied with a small paintbrush or pipette. The diameter of the central porous area of the membrane, d_{mem} , in these studies is 2.0 cm. This method for fabricating a robust interface is based on many published rotating cell studies (Hughes & Biswas, 1991; Albery, Burke, Leffler, & Hadgraft, 1976). All chemicals described in this paragraph are Analar grade or higher and purchased from Merck.

Once the RDC inner cylinder is filled with organic phase it must be left for 1-2 minutes for the membrane to become fully saturated by organic phase. Thus, once the inner cylinder containing the organic phase is lowered into the outer vessel containing the aqueous phase, the liquid/liquid interface is manifest on the outer surface of the inner cylinder during RDC operation. The GSWP04700 nitrocellulose membrane filter described above is hydrophilic, however it is not oleophobic and allows for organic phase saturation. This is evident when observing the membrane after the organic phase saturation has taken place; the organic phase begins to drip from the outer surface of the membrane. This indicates the possibility of organic saturation despite the membrane's hydrophilicity.

For the organic phases situated in the inner cylinder of the RDC during the experiments, TBP, octanol and odourless kerosene was purchased from Merck in Analar grade purity or higher, TODGA was purchased from Technocomm Ltd. (Falkland, Scotland, UK) in 99% purity and n-dodecane was purchased from Alfa-Aesar (Heysham, Lancashire, UK) in 99% purity. For the aqueous phases situated in the outer cylinder of the RDC during the experiments, the nitric acid, neodymium(III) nitrate hexahydrate ($\text{Nd}(\text{NO}_3)_3 \cdot 6\text{H}_2\text{O}$) and cerium(IV) sulphate ($\text{Ce}(\text{SO}_4)_2$) was purchased from Merck in Analar grade or higher. The water used is ultrapure, doubly de-ionised water from a Direct-Q 3 UV Millipore water purification system with a resistivity of 18.2 M Ω .cm. All organic and aqueous phases are made freshly within a day of the experiment taking place and phases do not undergo pre-contacting.

3.1.1 Sampling Protocol

The concentration over time of the organic metal ion is measured via the taking of organic phase samples through a hole down the centre of the static baffle using a pipette. The sample is then placed in a cuvette and the UV-visible light absorbance spectrum recorded. More details about this method of spectroscopy can be found in Section 3.3.1. After the UV-visible light absorbance spectrum is obtained, the sample is returned to the RDC inner cylinder, through the sample hole, to maintain a constant organic phase volume for the entirety of the experiment. The reason for maintaining a constant organic phase volume is that the distribution coefficient of a given metal ion in an organic/aqueous extraction system are in terms of concentration, which is clear in Equation 2.2.2 from Section 2.2. Thus, if the volume of organic phase decreases over the experimental time period, and if samples taken are disposed and not returned to the RDC inner vessel, the total amount of metal ion required to

be transferred from the aqueous phase to the organic is less than if the organic phase remained constant, in order to reach equilibrium concentrations. Furthermore, if the organic phase volume decreased over time, the *rate* of transfer would likewise decrease over time due to this phenomenon, obscuring any information pertaining to the rate of extraction due to diffusive and chemical kinetic properties; the intended research outcome.

3.2 Liquid-liquid Mixer-Centrifuge Method

Some experiments, additional to the RDC, in this thesis required the contacting of relevant aqueous and organic phases in an Eppendorf Thermomixer, a standard apparatus available from Eppendorf Ltd. (Stevenage, UK) followed by a phase separation in a centrifuge.

Typical experimental conditions are as follows. 1.0 cm^3 samples of organic phase are pipetted into a standard 2.0 cm^3 Eppendorf tube (also purchased from Eppendorf Ltd.) along with 1.0 cm^3 of metal ion aqueous solution in acid. Each tube is shaken vigorously for one minute then placed in the Eppendorf Thermomixer for twenty minutes at 25°C with the rotary mixing speed set to 33.3 Hz. Following mixing, the samples are centrifuged for five minutes resulting in a separated aqueous phase sitting below the organic in each tube. UV-visible light absorbance spectra are then taken for each of the two phases in each sample.

3.3 Methods of Detection

3.3.1 Quantitative Metal Ion Detection with UV-visible Light Absorbance Spectroscopy

Samples of the aqueous or organic phase known to contain the solute are placed in a quartz cuvette with a path length of 1.0cm, purchased from Thorlabs (Exeter, UK), which is then slotted into the sample chamber of a Gamry UV-visible light spectrometer, purchased from Gamry Instruments (Warminster, Pennsylvania, USA). The apparatus is set up as shown by Figure 3.3.1.1. The UV-visible light spectrum can then be recorded using this instrument.

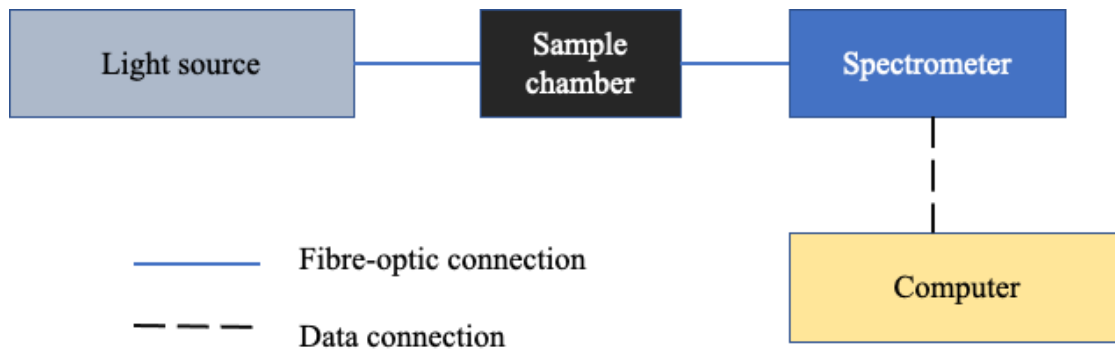


Figure 3.3.1.1: Diagram showing the UV-visible light spectrometer apparatus set up.

To avoid external light interference, the sample chamber has an opaque cap which is secured before the spectra are recorded. Thus, the only light which passes through the sample emanates from the deuterium/tungsten bulb situated in the light source unit shown in Figure 3.3.1.1 and the fibre-optic cables are aligned so as to ensure the light signal passing through the sample travels in a straight line before it is detected by the spectrometer. The readings which the spectrometer transfers via a data connection with the computer are the light intensity, I , in units of flux, $(\text{mol photons})\cdot\text{m}^{-2}\cdot\text{s}^{-1}$, or photon counts, measurements for all the wavelengths of light from 200 nm to 850 nm incident on the spectrometer CCD (charge coupled device), which detects the light.

Concentration of a solute, $[S]$, of a particular species in solution is proportional to its absorbance, A , at a given characteristic wavelength via the Beer-Lambert Law: $A = \epsilon l[S]$, where ϵ is the extinction coefficient and l is the path length of the sample. Absorbance of the species of interest in solution is calculated based on the theory that light intensity at a particular wavelength passing through the sample may be expressed by $I = I_0 e^{-A}$, where I_0 is the light intensity of a ‘blank’ or transparent sample and A is the wavelength-specific absorbance (Gamry Instruments, 2021). The blank sample is not simply a spectrum reading in the case where no sample is present in the spectrometer. Instead, a blank light intensity spectrum is recorded using an identical solvent to the sample of interest, but *without* the species of interest dissolved in it. The absorbance spectrum of the species of interest is then found using $A = -\log\left(\frac{I}{I_0}\right)$; the resulting spectrum is that of our species of interest with respect to its blank. Figure 3.3.1.2 shows example spectra of this procedure.

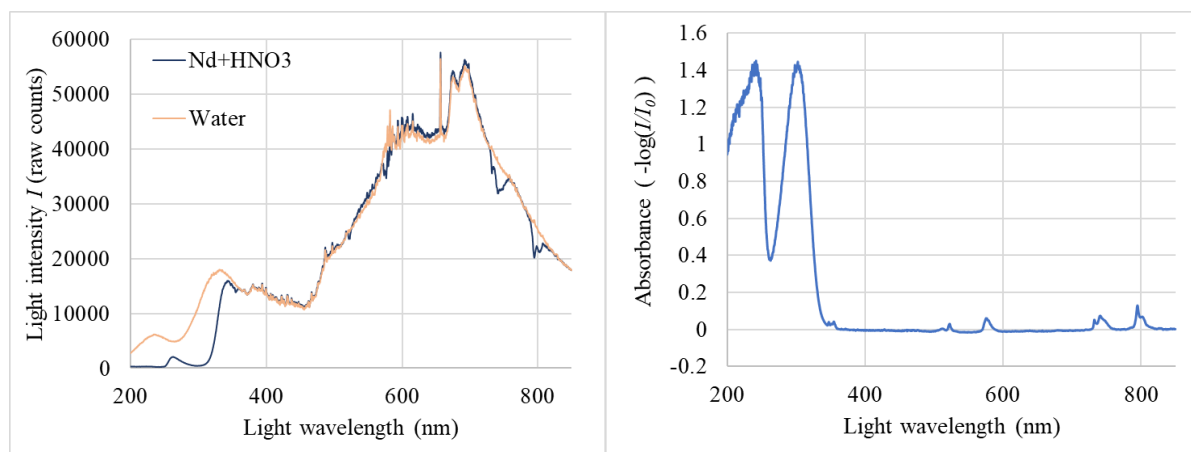


Figure 3.3.1.2: Example graphs showing the light intensity/raw counts spectra for neodymium(III) dissolved in nitric acid on top of pure water (left) and the absorbance spectrum of nitric acid and neodymium(III) ions in solution with respect to water as the chosen blank sample (right).

One final intricacy of UV-visible light absorbance spectroscopy is base-line (or base) correction. Due to the noise associated with fibre-optic connections, tiny variations of contaminants and/or bubbles in solution or scratches in the glassware, absorbance may shift in the y-axis direction. This phenomenon results in absorbance peaks being exaggerated or diminished and therefore can lead to inaccurate concentration readings being recorded. The absorbance of interest at 585 nm, shown in Figure 3.3.1.2, is measured with respect to the base-line shift at approximately 550 nm and 605 nm, in Figure 3.3.1.3, where the absorbance of the species of interest is expected to be zero. The y-axis shift is not consistent across all wavelengths.

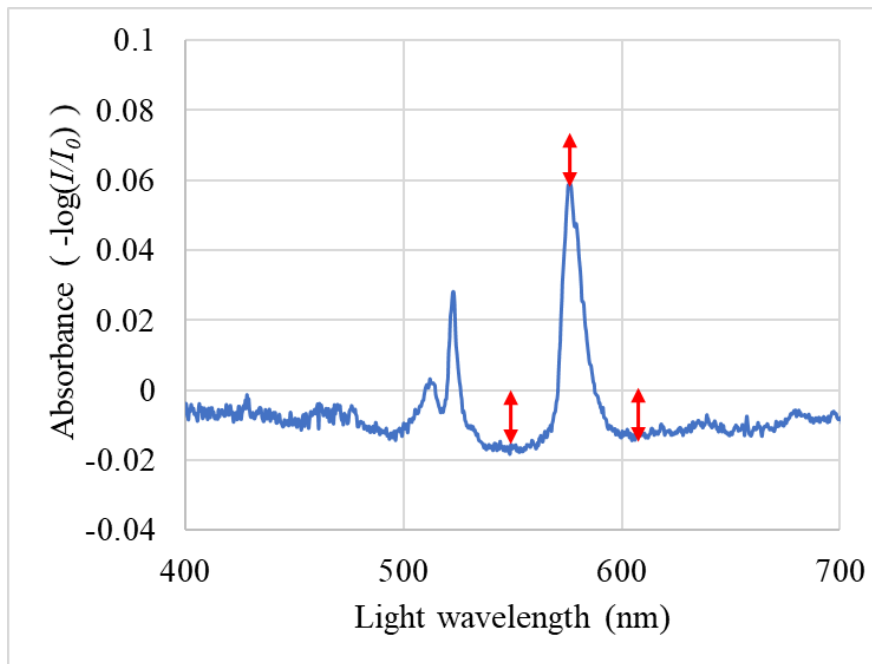


Figure 3.3.1.3: Illustration of base-line correction effects on a zoomed in section of Figure 3.3.1.2. By addition of the amount by which the absorbance base-line is shifted in the spectrum, shown by the red arrows, the parts of the spectrum which should be zero become zero and the characteristic peak adopts its slightly higher, true magnitude.

3.4 Computational Modelling in gPROMS

The principal modelling platform used in the work presented here is PSE gPROMS, available from Process Systems Enterprise (Hammersmith, London, UK). This is a declarative⁴ modelling environment suitable for numerically solving systems of linear and ordinary differential equations (ODEs). Furthermore, it has a facility for importing experimental data for the purposes of optimising unknown experimental constants which feature in the set of model equations. gPROMS is used for a wide range of process modelling tasks in the literature and, because the numerical solvers are in-built, i.e. the user is not required to explicitly write their own finite elements code, it is the industry standard tool (Woodhead, McLachlan, Taylor, Müllich, & Geist, 2019; Edwards, et al., 2019; Chen, Taylor, Jobson, Woodhead, & Masters, 2016).

⁴ A declarative model is one which does not require the line-by-line instructions of the task or calculation to be written. Instead, this line-by-line instructional code is preconfigured and all that is required of the modeller is to provide or “declare” the model in the required higher level coding language. This declared model is then run to provide a solution by being input and interpreted by the preconfigured code.

The following subsections outline some of the mathematical and statistical tools available in gPROMS, which are referred to in the results chapters of this thesis.

3.4.1 Confidence Intervals

90%, 95% and 99% confidence intervals relate to the amount which an unknown constant can vary for a 90%, 95% or 99% probability of being a true value. Confidence intervals are calculated numerically within gPROMS by inputting into the model equations values for each of the unknown constants of interest, within a given range the user has specified, and comparing the value of the resulting dependent variable(s) for which there exist experimental data.

3.4.2 t-value

The t-value test is a statistical test which poses as its null hypothesis that an estimated value for an unknown constant is likely, at a given confidence level, to be no different to zero, in other words, the constant has no effect on the model. In gPROMS the default confidence level for the t-value test is 95%. Accordingly, a 95% t-value for each estimated constant, X , is computed using the equation $X = \frac{\bar{X}-0}{\delta_{95\%}}$ with the numerator denoting the difference between the estimated value of the unknown constant, \bar{X} , and zero, which originates from the mathematical interpretation of the null hypothesis described above. The denominator denotes the 95% confidence interval, $\delta_{95\%}$. The next step is to compare this with the reference t-value produced by in one-tailed t-distribution table (Boslaugh, 2012). Only if the t-value for the estimation of the unknown constant is *greater* than the reference t-value can the null hypothesis be rejected; in which case the estimated value of the unknown constant *is* different from zero and therefore important in the model fit.

3.4.3 Standard Deviation

Standard deviation is defined as $\sigma = \sqrt{\frac{\sum_{i=1}^N (X_i - \mu_i)^2}{N}}$ where X_i and μ_i are the variable set and the experimental data, respectively, with N being the number of experimental data.

3.4.4 Chi-squared Test for Goodness of Fit

The definition of the χ^2 test for goodness of fit can be found in Data Reduction and Error Analysis for the Physical Sciences by Bevington and Robinson: “the [χ^2] method of least

squares is based on the hypothesis that the optimum description of a set of data is one that minimises the weighted sum of the squares of the deviation of the data $[X_i]$ from the [points which can be defined by a] fitting function $[f_i]$ " (Bevington & Robinson, 1994).

In all instances in this report where a χ^2 test for goodness of fit is used, a fitting function f , which can be (but is not always) a linear function f (i.e. $f = mx + c$) defines experimental data X_i . The experimental data additionally carry an experimental uncertainty, the standard deviation, σ_i . With this information a variance function s^2 can be computed which is described by Equation 3.4.4.1. N is the number of experimental data and n is the number of fitting parameters being used to make the fit, for example in a linear fit m and c are these fitting parameters, ergo $n = 2$ in this case. w_i is the weighting function which is defined by Equation 3.4.4.2.

$$s^2 = \frac{1}{N - n} \sum w_i (X_i - f_i)^2 \quad (3.4.4.1)$$

$$w_i = \frac{1/\sigma_i^2}{(1/N) \sum (1/\sigma_i^2)} \quad (3.4.4.2)$$

s^2 can then be used to calculate χ^2 via Equation 3.4.4.3. The goodness of fit is then found by comparing the produced χ^2 with a χ^2 -critical value which can be found in a standard statistical table. A χ^2 -critical, or a χ_v^2 (which is the reduced form of χ^2 , see Equation 3.4.4.3) value for a particular fit is defined in the standard table by its degrees of freedom and the desired alpha level. Alpha level is a measure of the level of confidence in the experimental data and is 0.05 in all estimations for this thesis, which corresponds to a confidence level of 95%. An example χ^2 -critical table is shown by Table 3.4.4.1. In Equation 3.4.4.3, ζ is the number of degrees of freedom defined as $\zeta = N - n$ and $\langle \sigma_i^2 \rangle$ is the weighted average of the individual variances defined by Equation 3.4.4.4. As aforementioned, χ_v^2 is the reduced form of the χ^2 value which is sometimes tabulated instead of χ^2 -critical.

$$\frac{\chi^2}{\zeta} = \frac{s^2}{\langle \sigma_i^2 \rangle} = \chi_v^2 \quad (3.4.4.3)$$

$$\langle \sigma_i^2 \rangle = \left[\frac{1}{N} \sum \frac{1}{\sigma_i^2} \right]^{-1} \quad (3.4.4.4)$$

Table 3.4.4.1: Standard table of χ^2 -critical values.

Degrees of freedom (ζ)	Alpha level		
	0.1 (90% confidence)	0.05 (95% confidence)	0.01 (99% confidence)
1	2.71	3.84	6.64
2	4.61	5.99	9.21
3	6.25	7.82	11.3
4	7.78	9.49	13.3
5	9.24	11.1	15.1
6	10.6	12.6	16.8
7	12.0	14.1	18.5
8	13.4	15.5	20.1
9	14.7	16.9	21.7
10	16.0	18.3	23.2

If χ^2 is found to be less than the χ^2 -critical value, the conclusion is that the function used to model the experimental data is a good fit. Finding a fit which minimises χ^2 is computed in gPROMS automatically and for data processed in MS Excel, the minimisation of χ^2 is achieved manually through use of the equations specified in this section.

Chapter 4: RDC Extractions of Ce(IV) by TBP Part 1: Experiments which Underpin the Theory

In this section, a study of the extraction of Ce(IV) by TBP within the RDC will be presented. This includes work undertaken by Bromley *et al*, previously reported (Bromley & Boxall, 2015), as well as additional experiments conducted by the author. It was the work of Bromley *et al* that first determined that, within the RDC, the rate of metal ion extraction counter-intuitively increases with the inverse of the RDC rotation speed – rather than increasing with the rotation speed directly.

4.1 Published Absorbance Data

Bromley *et al* followed the extraction of Ce(IV) by TBP within the RDC by measurement of the UV-visible light absorbance of extracted Ce(IV) in the organic phase as a function of time at a range of rotation speeds between and 1 and 10 Hz (Bromley & Boxall, 2015). Figure 4.1.1 shows the data for the ingrowth of the UV-vis spectrum of the Ce(IV)-TBP complex with increasing extraction time at an RDC rotation speed of 1 Hz.

From Figure 4.1.1, a strong peak with an absorbance maximum at a wavelength of 338 nm grows in with increasing extraction time. Consequently, Bromley *et al* used this peak as a measure of the concentration of the extracted Ce(IV)-TBP in the organic phase as a function of time at all RDC rotation speeds studied. It should be noted from Figure 4.1.1 that it is likely that the true maximum of this peak, λ_{\max} , occurs at a wavelength less than 338 nm. This is suggested by the lack of symmetry in the peak and that the intensity of the absorbance drops off sharply with decreasing wavelength at $\lambda < 330$ nm. Bromley *et al*. attribute this to a significant absorbance feature associated with the solvent phase at wavelengths < 330 nm. This absorbance saturates the detector of the spectrometer, resulting in useful information being cut-off in this range. As a result, the absorbance at 338 nm was used as a measure of extracted Ce(IV)-TBP complex concentration, mindful of it most likely being a tail in the higher wavelength range of the true absorbance maximum at λ_{\max} .

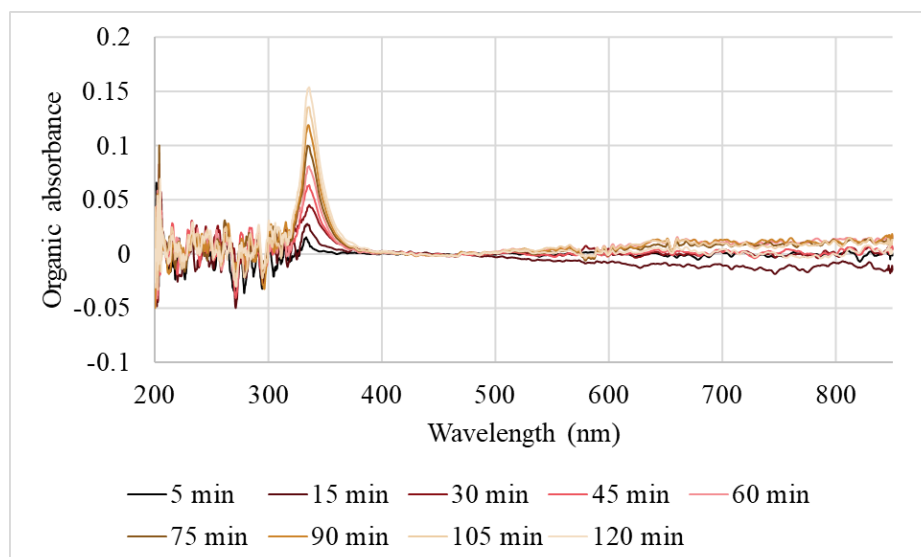


Figure 4.1.1: Example RDC spectra of Ce(IV) extraction by TBP/OK for a rotation speed of 1 Hz. Base corrected with respect to a wavelength region of 400-500 nm. Data gathered by Bromley *et al* (Bromley & Boxall, 2015).

Plots of UV-visible absorbance of Ce(IV) at a wavelength of 338 nm in the organic phase as a function of extraction time at a range of RDC rotation speeds are shown in Figure 4.1.2. In the original publication of this data (Bromley & Boxall, 2015), the absorbance at 338 nm appeared to be negative during extraction times of <20 minutes at all RDC rotation speeds studied – typically with a small maximum negative value of -0.03 absorption units. Of relevance here is that time 0 minutes refers to the point when RDC rotation is first engaged and not when the two phases first undergo contact. The two phases first undergo static contact for a period of approximately one minute prior to the RDC beginning its rotation due to apparatus setup requirements.

Thus, a likely explanation for the negative absorbance seen at extraction times from 0 – 20 min is the stripping of a small amount of TBP from $0.2 \text{ mol}\cdot\text{dm}^{-3}$ TBP in OK organic phase into the aqueous phase during the initial static contact period. TBP is known to have a weak absorption tail at 338 nm in dodecane (the main component of OK) (Wongsawa, et al., 2018) and an aqueous solubility of $1.46 \text{ mmol}\cdot\text{dm}^{-3}$ in nitric acid (Velavendan, et al., 2013). The low but finite value of the latter, plus the large concentration of TBP in the organic phase, may result in the kinetics of the transfer of TBP being fast enough to be both observable and near-complete during the initial contact period of any RDC extraction experiment – resulting in a small decrease in the absorbance seen at 338 nm in the organic phase and thus the

negative absorbance values seen in the vicinity of that wavelength at short extraction times. Given the likelihood of this rapid approach to completion of the transfer of TBP to the aqueous phase, it is not unreasonable to assume that the TBP transfer is effectively complete before any substantial transfer of Ce(IV) has occurred – a transfer that takes place over the timescale of several hundred minutes, see Figure 4.1.1. In other words, we can reasonably assume that the change in absorbance at 338 nm due to TBP stripping can be treated as being effectively not time-dependent during Ce(IV) extraction. Thus, at RDC experiment times longer than 20 mins, the absorbance due to Ce(IV) extraction at 338 nm may be obtained by baselining against the absorbance recorded at 0 minutes. This issue of baseline subtraction notwithstanding, it can be seen from Figure 4.1.2 that absorbance appears to be linearly proportional to extraction time at each rotation speed studied.

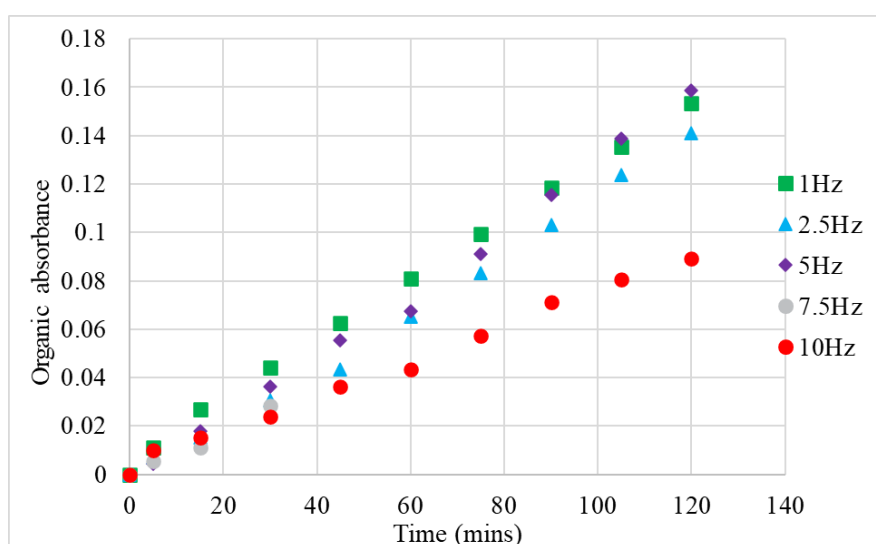


Figure 4.1.2: RDC extraction of Ce(IV) into the organic phase of $0.2 \text{ mol}\cdot\text{dm}^{-3}$ TBP in OK from an initial aqueous phase of $10 \text{ mmol}\cdot\text{dm}^{-3}$ Ce(IV) in $1.0 \text{ mol}\cdot\text{dm}^{-3}$ nitric acid, as a function of time. The organic absorbance was taken at a λ_{max} peak of 338 nm. Data originate from experiments conducted by Bromley *et al* (Bromley & Boxall, 2015).

One RDC experiment was performed per rotation speed which is the reason why Figure 4.1.2 does not have any error bars. As the development of the kinetic model (see Section 5) and the generation of new RDC data were the principal aim of this author's work, repeats of the Bromley data were not pursued.

It is clear from Figure 4.1.2 that the increase with time of the absorbance associated with Ce(IV)-TBP complex in the organic phase is slower at the higher RDC rotation speeds

studied, i.e. 7.5 and 10 Hz, than at its lower speeds, i.e. 1, 2.5 and 5 Hz. It should be noted that the data for 7.5 Hz only extend into the first thirty minutes of extraction time due to a malfunction in the RDC membrane (Bromley M. , 2021). Despite this, given that it is the initial rate of extraction which is of principal interest to these studies, the data are used alongside those that extended to longer extraction times in the analysis below. From the five rotation speeds studied, the general trend is that extraction rate is inversely proportional to rotation speed – an exception being the extraction rate at 2.5 Hz, which is lower than at 5 Hz. We shall return to this point below.

4.2 Obtaining the Organic Ce(IV) Extinction Coefficient

The Ce(IV) extraction data of Figure 4.1.2 is expressed in terms of changes in the UV-visible light absorbance of extracted Ce(IV) in the organic phase as a function of time, rather than as the more analytically useful molar concentration of Ce(IV) in the organic phase as a function of time. However, this data may be readily converted to plots of organic Ce(IV) concentration versus time by dividing the absorbance values by the extinction coefficient, $\epsilon_{\text{Ce(IV),org,338nm}}$ for Ce(IV) in the organic phase at the measurement wavelength used, λ_{338nm} . To determine a value of this extinction coefficient, a mixer/centrifuge-based small batch extraction experiment was set up using the same apparatus outlined in Section 3.2.

In this experiment, the two phases were made up as follows: an organic phase containing 0.2 mol.dm^{-3} TBP in OK; and an aqueous phase containing 10 mmol.dm^{-3} Ce(IV)(SO₄)₂ in 1.0 mol.dm^{-3} nitric acid. Equal volumes of each were then pipetted into Eppendorf tubes and mixed using a temperature-controlled Eppendorf rotary thermomixer at a temperature of 25°C. They were typically mixed for a period of fifteen minutes and then centrifuged to achieve phase separation. Figure 4.2.1 shows the pre- and post-mixing aqueous phase absorbance spectra, each recorded with respect to a nitric acid blank, with dilution by a factor of ten of both the blank and the sample. Figure 4.2.2 again shows the pre- and post-mixing aqueous phase spectra, this time with each having been recorded with respect to a pure water blank, with dilution by a factor of ten; it also shows a spectrum of a 1.0 mol.dm^{-3} nitric acid diluted by a factor of ten (thus the spectrum reflects a nitric acid concentration of 0.1 mol.dm^{-3}) also recorded with respect to a pure water blank, for comparison. Figure 4.2.3 shows the post-mixing organic phase absorbance spectrum recorded with respect to a pure organic phase (i.e. 0.2 mol.dm^{-3} TBP in OK) blank.

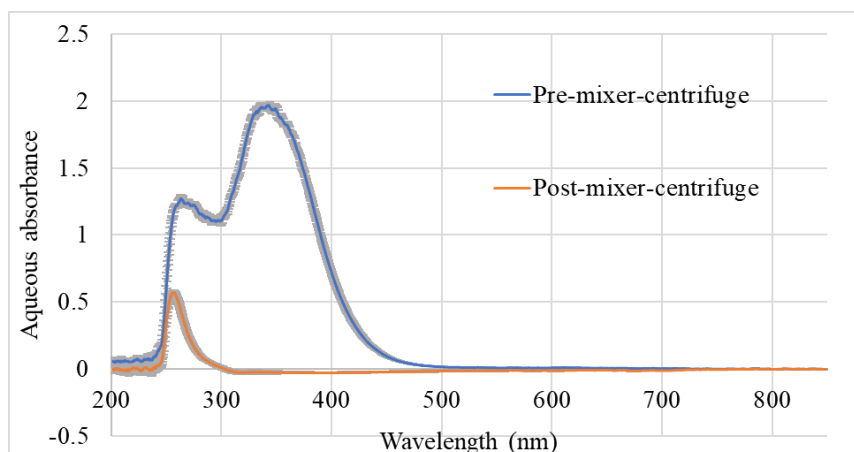


Figure 4.2.1: Aqueous UV-visible light spectra for pre- and post-mixer-centrifuged samples of aqueous 10 mmol.dm^{-3} Ce(IV) in 1.0 mol.dm^{-3} nitric acid. The samples were contacted with an organic phase of 0.2 mol.dm^{-3} TBP in OK in the thermomixer. Absorbance computed with respect to a blank of 1.0 mol.dm^{-3} nitric acid with both the sample and the blank diluted by a factor of ten in 0.5 mol.dm^{-3} sulphuric acid. Base corrected with respect to absorbance at 800-850 nm.

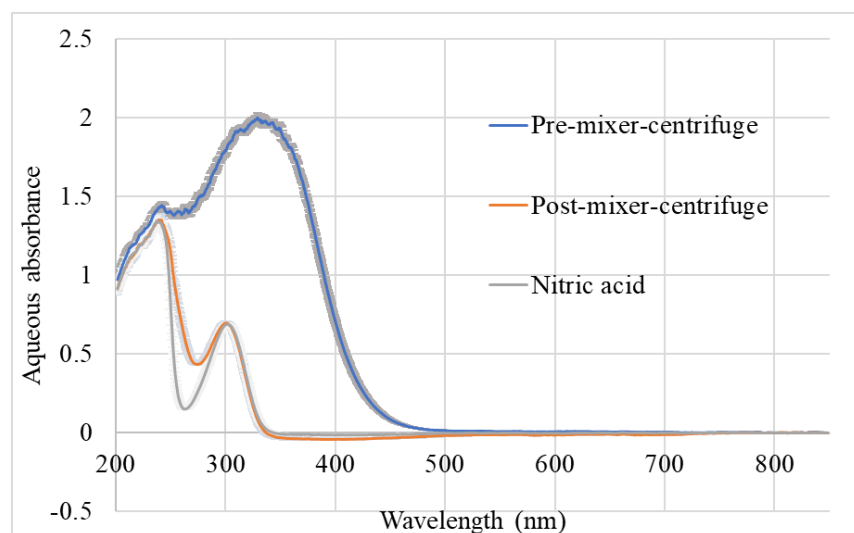


Figure 4.2.2: Aqueous UV-visible light spectra for pre- and post-mixer-centrifuged samples of aqueous 10 mmol.dm^{-3} Ce(IV) in 1.0 mol.dm^{-3} nitric acid. The samples were contacted with an organic phase of 0.2 mol.dm^{-3} TBP in OK in the thermomixer. Plotted alongside is a pure nitric acid spectrum for comparison. Absorbance in all cases computed with respect to a blank of water with the two samples as well as the nitric acid diluted by a factor of ten in 0.5 mol.dm^{-3} sulphuric acid. Base-corrected with respect to absorbance at 800-850 nm.

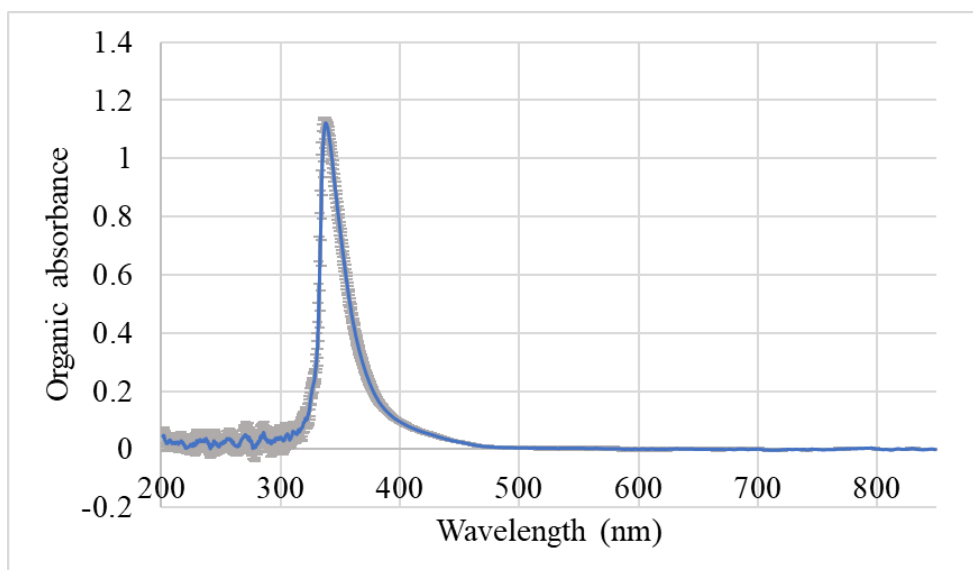


Figure 4.2.3: Organic UV-visible light spectra for post-mixer-centrifuged samples of aqueous 10 mol.dm^{-3} Ce(IV) in 1.0 mol.dm^{-3} nitric acid. The samples were contacted with an organic phase of 0.2 mol.dm^{-3} TBP in OK in the thermomixer. Absorbance computed with respect to a blank of the organic phase before it was mixed-centrifuged with the Ce(IV) loaded aqueous. Base corrected with respect to absorbance at 800-850 nm.

The dilutions by a factor of ten of the aqueous phase performed in obtaining the data of Figures 4.2.1 and 4.2.2 were performed using 0.5 mol.dm^{-3} H_2SO_4 rather than pure water. The reason for diluting the aqueous phase samples before recording their UV-visible light absorbance spectra is that 1.0 mol.dm^{-3} nitric acid strongly absorbs at a wavelength centred at 300nm to the point of detector saturation. Thus, bringing the concentration of acid down by a factor of ten prevents this saturation behaviour from occurring. This is especially important given the proximity of the Ce(IV) absorbance at 300-400 nm, see Figures 4.2.1 and 4.2.2, to the nitric acid absorbance centred at 300 nm. Use of 0.5 mol.dm^{-3} acid as the diluting medium ensures the proton concentration is maintained at approximately 1.0 mol.dm^{-3} . When water is used for dilution, a cloudy precipitate is formed. This is because the use of water as the diluting medium raises the pH of the solution. As pH increases, Ce(IV) ions are known to precipitate as an insoluble oxide/hydroxide, causing the solution to become cloudy (Gschneidner, Bünzli, & Pecharsky, 2006). Thus, using acid rather than water to dilute Ce(IV) in nitric acid addresses this problem as the diluent maintains the pH of the solution. Use of sulphuric acid specifically to perform this dilution has an additional advantage in that it does not have a UV-visible light absorbance peak in the absorbance region of interest, ~250-450 nm (data not shown).

In the pre-mixer-centrifuge data of Figure 4.2.1, the principal Ce(IV) peak in the aqueous phase when recorded with reference to nitric acid is shown to be centred at approximately 340 nm and, despite the absorbance emerging at approximately 260 nm, exhibits good symmetry. In the pre-mixer-centrifuge data of Figure 4.2.2, the analogous spectrum recorded with reference to water exhibits a principal Ce(IV) peak in the aqueous phase with the same peak wavelength of 340 nm, as well as the same magnitude of absorbance. Given that the spectra of Figures 3.2.1 and 3.2.2 were recorded with respect to nitric acid and water references respectively this indicates that, at wavelengths in the vicinity of 340 nm, absorbance associated with nitric acid is not interfering with that of Ce(IV); we shall return to this point below. It should be noted, however, that the absorbance peak at 340 nm in Figure 4.2.2 is not as symmetrical as it is in Figure 4.2.1. This is again related to the fact that Figure 4.2.1 contains spectra referenced to nitric acid and Figure 4.2.2 contains spectra referenced to water, and thus the latter spectral data shows the absorbance peak of Ce(IV), centred at 340 nm, overlapping with that of nitric acid, centred at 300 nm.

Figure 4.2.1 may be used to discern the quantity of aqueous Ce(IV) that has been transferred from the aqueous phase to the organic phase. As aforementioned, due to the fact that the absorbance shown by Figure 4.2.1 is calculated with respect to a pure nitric acid blank, the spectra for pre- and post-mixer-centrifuge relates *only* to presence of Ce(IV). The most prevalent peak at 340 nm in the pre-mixer-centrifuge curve is around 2.0 absorbance units in magnitude but has diminished to the zero baseline in the post-mixer-centrifuge curve in Figure 4.2.1. This is an indication that the Ce(IV) has been *entirely* extracted by the TBP/OK organic phase. There is a smaller, secondary absorbance peak, visible in both pre- and post-mixer-centrifuge curves in Figure 4.2.1, at a wavelength around 260 nm. This peak may be ignored due to the UV-visible light absorbance at wavelengths <280 nm being regarded as the cut-off point for the spectrometer when interrogating nitric acid systems due to the intense absorbance saturation of the acid in this wavelength region.

Figure 4.2.3 shows the Ce(IV) absorbance spectrum in the organic phase with a peak at 338 nm; the same as was observed in the RDC data of Figure 4.1.1. We can be sure that nitric acid does not interfere with the UV-vis absorbance at this wavelength because a previous study found no absorbance peak for nitric acid in a TBP organic phase at 338 nm (Woodhead J. L., 1965). Based on the above observation from Figure 3.2.1 that all of the Ce(IV) has been extracted from the aqueous phase during the mixer-centrifuge experiment, it can be deduced

that, due to the equivalent volume of the organic and aqueous phases which underwent the mixing/centrifuge process, this absorbance peak corresponds to an organic phase Ce(IV) concentration of 10 mmol.dm^{-3} . Given a cuvette path-length l of 1.0 cm , a value of $\epsilon_{\text{Ce(IV),org,338nm}}$ of $0.11 \pm 0.002 \text{ mol}^{-1}.\text{m}^3.\text{cm}^{-1}$ may then be calculated by simple application of the Beer-Lambert law.

4.3 RDC Experimental Results in Units of Concentration

Using this extinction coefficient value, the data of Figure 4.1.2 may now be converted to show the ingrowth of the concentration of Ce(IV) in the TBP/OK organic phase as a function of time during RDC extraction experiments at rotation speeds of 1-10 Hz (Bromley & Boxall, 2015), Figure 4.3.1. Even though an experimental error is associated with the extinction coefficient, this error has not been propagated to the data in Figure 4.3.1 because the original RDC experiments were not repeated by Bromley at each rotation speed. Uncertainty is associated with Figure 4.3.1, but it shall not be discussed here. As the Bromley data were principally used to underpin the derived kinetic theory for application to the author's experiments, for TODGA/Nd(III) which were repeated, this was considered justifiable.

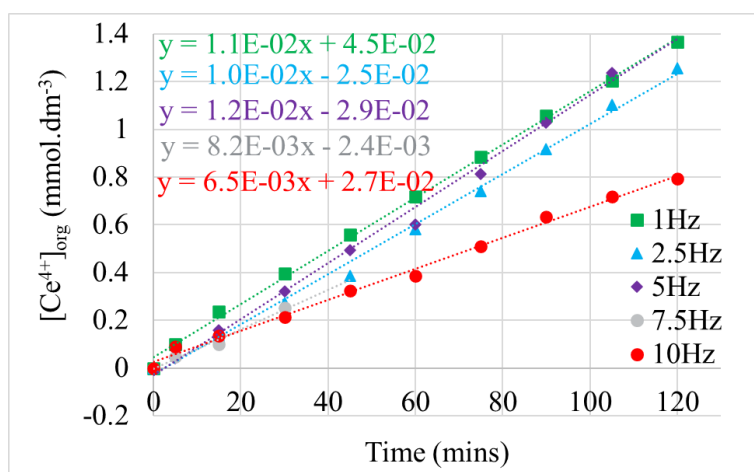


Figure 4.3.1: Concentration of organic Ce(IV) as a function of experimental time period for the RDC at several rotation speeds. Organic phase consists of 0.2 mol.dm^{-3} TBP in OK and aqueous phase initially consists of 10 mmol.dm^{-3} Ce(IV) in 1.0 mol.dm^{-3} nitric acid. Base correction calculated with respect to the wavelength region 400-500 nm.

As might be expected, this shows that the rate of concentration increase of Ce(IV) in the TBP/OK organic phase as a function of time is constant over the entire experimental time period studied. This also implies that saturation loading of Ce(IV) in the organic phase has

not been reached, even up to the maximum $[\text{Ce}^{4+}]_{\text{org}}$ value of 1.4 mmol dm^{-3} seen in Figure 4.3.1. This latter is observation in agreement with the mixer-centrifuge studies of Section 4.2, wherein it was found that all 10 mmol.dm^{-3} of the Ce(IV) initially in the aqueous phase can be extracted into the organic phase.

As was observed from the source data of Figure 4.1.2, Figure 4.3.1 again shows that the faster extraction rates are observed at the lower RDC rotation speeds. This trend is found throughout the RDC runs reported in this thesis wherein the organic phase is situated in the rotating inner cylinder extracting from a stationary aqueous acid phase containing the dissolved metal. Simple automatic linear trendlines in MS Excel were plotted instead of chi-squared fits. Chi-squared fits are more suitable for fits to data with experimental error. Using the slope of the curves shown in Figure 4.3.1, the flux of extraction may be calculated by taking into account the organic phase volume of 35 cm^3 and the interfacial area of $\frac{\pi d_{\text{mem}}^2}{4}$, where $d_{\text{mem}} = 2.0 \text{ cm}$, the diameter of the porous membrane at the base of the inner cylinder. From this calculation, Figure 4.3.2 may be produced, showing RDC extraction flux as a function of inverse square root RDC rotation speed, $\omega^{-0.5}$.

In Figure 4.3.2, there is a positive correlation between extraction flux, j , and inverse square root of rotation speed, $\omega^{-0.5}$, in the region $<0.45 \text{ Hz}^{-0.5}$, i.e. at RDC rotation speeds $>5 \text{ Hz}$. However, in the inverse square root of rotation speed region $>0.45 \text{ Hz}^{-0.5}$, i.e. at rotation speeds $<5 \text{ Hz}$, the datapoints plateau and indicate a Ce(IV) extraction into the organic phase which becomes not dependent on rotation speed. This behaviour will remain a feature of subsequent data later in this thesis and also be expanded upon in Chapter 5. It was unfortunate that the RDC experiments by Bromley were not repeated enough times to obtain reliable uncertainties, and this is why Figure 4.3.2 does not have associated error bars.

A wide range of extraction fluxes has been reported in the literature for experiments conducted using an RDC or RDC-related system. These values of the fluxes reported are strongly dependent on the system under study. An extraction flux of $0.1 - 1.0 \text{ mol.m}^{-2}.\text{s}^{-1}$ has been observed in D2EHPA/Mn(II) and D2EHPA/Vn(IV) extractions (Hughes & Biswas, 1991; Hughes & Biswas, 1993) and an extraction flux of $\sim 1 \times 10^{-4} \text{ mol.m}^{-2}.\text{s}^{-1}$ has been observed in copper/oxime extractions (Albery, Choudhery, & Fisk, 1984; Albery & Choudhery, 1988). The most similar chemical system to the Ce(IV)/TBP RDC extraction system presented in Figure 4.3.2 is Fe(III) extraction by TBP (Meng, Yu, & Chen, 1996)

which has an approximate flux of extraction of $\sim 4 \times 10^{-7} \text{ mol.m}^{-2}.\text{s}^{-1}$. Thus, the order of magnitude of the flux encountered in the Ce(IV)/TBP RDC extraction system under study here, Figure 4.3.2, in the order of $\sim 1 \times 10^{-5} \text{ mol.m}^{-2}.\text{s}^{-1}$ can be placed within that of the literature range, which supports its validity.

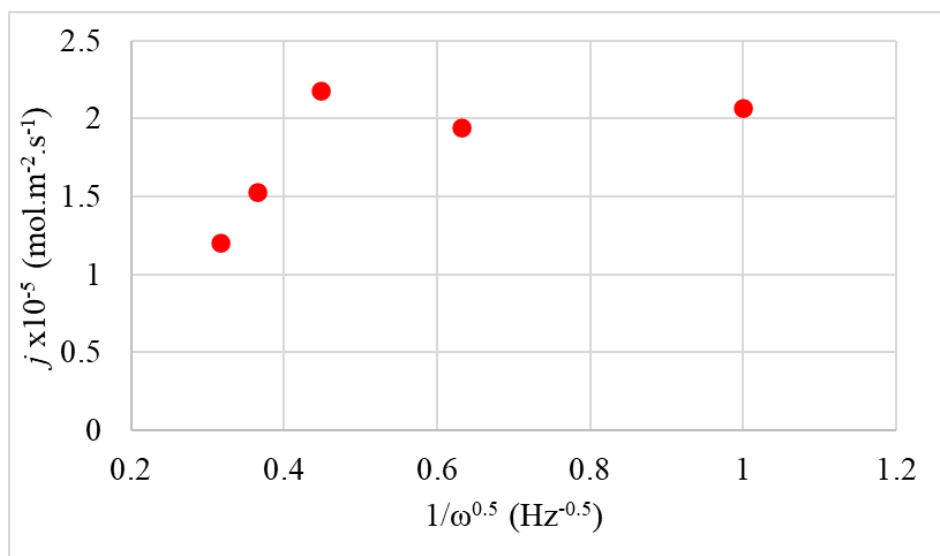


Figure 4.3.2: RDC extraction flux, j , of Ce(IV) into the organic phase of 0.2 mol.dm^{-3} TBP in OK from an initial aqueous phase of 10 mmol.dm^{-3} Ce(IV) in 1.0 mol.dm^{-3} nitric acid, as a function of RDC inverse square root of rotation speed, $\omega^{-0.5}$. Original data gathered by Bromley *et al.*

Even though the approximate magnitude of the flux reported here is comparable to those reported in other mass transfer studies, it is difficult to compare the observed RDC experimental flux inverse dependency on rotation speed shown by Figure 4.3.2 with that found in the literature. This is because, in conventional two-film theory, the relationship between extraction flux and the rotation speed of a rotating diffusion cell is expressed via an equation which is comprised of a mass transfer coefficient and the concentration gradient of a species over the stagnant film or diffusion region between two phases. Flux, j , is thus classically expressed via Equation 4.3.1 where $K_{\text{MT,aq}}$ is the aqueous phase mass transfer coefficient and $([S]_i - [S]_{\text{bulk}})$ is the concentration gradient of a solute S across the diffusion region bounded by the interfacial solute concentration $[S]_i$ and the bulk concentration $[S]_{\text{bulk}}$; both constants at steady state.

$$j = K_{MT,aq}([S]_i - [S]_{bulk}) = \frac{D_S}{X_D}([S]_i - [S]_{bulk}) = \frac{1.56D_S\omega^{\frac{1}{2}}}{v^{\frac{1}{6}}D_S^{\frac{1}{3}}}([S]_i - [S]_{bulk}) \quad (4.3.1)$$

In this context, the chemical reaction which allows a solute to be removed from the bulk solution entering the liquid phase on the opposite side of the interface is assumed to be occurring *at* the interface. Only under these conditions can the assumptions underpinning Equation 4.3.1 be made. $K_{MT,aq}$ is typically derived from the quotient $\frac{D_S}{X_D}$, where D_S is the diffusivity of the solute S and X_D is the diffusion region thickness with respect to that solvent. Crucially, all parts of Equation 4.3.1 are constants, apart from X_D , which is known to vary with the inverse square root of rotation speed (rotation speed in Hz being expressed by ω), from the Levich Equation shown by Equation 2.6.1. Thus, by this derivation, j is found to be *directly* proportional to rotation speed to the power a half, $\omega^{\frac{1}{2}}$, which is the case encountered in many RDC studies in the literature, but *not* the case for the experimental data in the work presented here.

This analysis has raised a number of questions as to the applicability of simple two-film theory illustrated by Equation 4.3.1, to the RDC-based Ce(IV)/TBP extractions under study here. Firstly, as has already been briefly described in Section 2.6, the complexed entity extracted, as a result of complexation between the sparingly soluble aqueous TBP, and Ce(IV), must *not* be created solely at the interface. As discussed above, it is more plausible that the diffusion layer *itself* is the reaction zone within which the complexing TBP ligand diffuses through, giving rise to a new solute via chemical complexation with Ce(IV); the TBP/Ce(IV) complex. Hence, we can conclude that the model underpinning Equation 4.3.1 is derived from a case which is *not* appropriate for the RDC studies of the TBP/Ce(IV) extraction presented here and a new model and associated analytical expressions must be developed based on an alternative understanding of the two-film model. This shall be the topic of the next chapter.

Chapter 5: Theory

As described in the previous chapter, initial experiments conducted in these laboratories focused on RDC-based studies of the liquid-liquid extraction by a TBP organic phase of Ce(IV) initially dissolved in nitric acid. The extraction rate of the Ce(IV) followed a counter-intuitive trend with respect to RDC rotation speed insofar as the greatest extraction rates were observed for rotation speeds <5 Hz and extraction rate decreased as rotation speed was increased above 5 Hz. As this observation is out with the classical twin-film interpretation of liquid-liquid extraction described in Figure 2.3.1 above, it is necessary to produce an alternative theory to explain the observed results.

Following the identification that the locus of the ligand/metal ion complexation reactions in the RDC is the aqueous diffusion layer, an analytical model, drawing on existing models for analogous devices such as the photoelectrochemical Optical Rotating Disc Electrode (see below) (Albery, Archer, & Edgell, 1977), forms the basis of the theory presented in this chapter.

5.1 RDC Parallels with Optical Rotating Disc Electrode Theory

The Optical Rotating Disc Electrode, ORDE, Figure 5.1.1, is a photoelectrode-based device for the study of photoelectrochemically active species in the solution phase. It was initially developed by Albery, Archer and Edgell (Albery, Archer, & Edgell, 1977) who subsequently used it for the study of thionine-based dyes for use in photogalvanic cells (Albery, Bowen, Fisher, & Turner, 1980) and colloidal semiconductors for use as photocatalysts (Boxall & Albery, 2000; Boxall & Albery, 2000). It consists of a cylindrical light guide, such as a quartz rod, one end of which has been coated with a thin layer of a transparent electrical conductor, such as doped tin oxide. The coated end may then be used as a disc-shaped working electrode to interrogate the electrochemistry of a sample electrolyte in an otherwise conventional three electrode (working/reference/counter) system in an electrochemical cell.

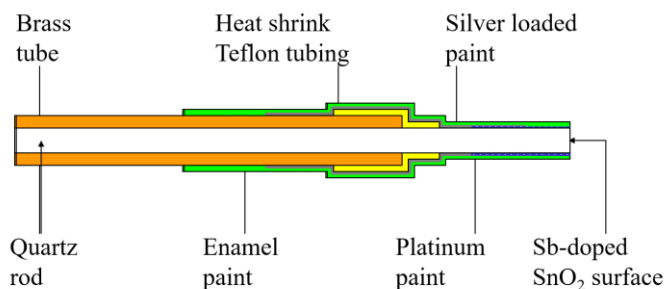


Figure 5.1.1: Diagram of an Optical Rotating Disc Electrode (Boxall, 2022).

The feature that differentiates the ORDE from a standard metal disc electrode in such a cell is that light may be passed down the lightguide, from which it enters the electrolyte by passing through the transparent disc electrode. If the electrolyte contains a species that may be photoexcited by the light entering the solution – such as a dye or a particulate semiconductor – then the ORDE may be used to study the electrochemistry of the photoexcited species as long as it is electrochemically active. Such species are said to be photoelectrochemically active.

Importantly, the intensity of the penetrating light as a function of distance from the electrode surface varies in accordance with the Beer-Lambert Law. Consequently, the rate of photoexcitation of the photoelectrochemically active species obeys a similar dependence. The photoexcited species in solution may then undergo mass transfer back to the surface of the electrode through which the light entered the solution - where it undergoes electrochemical oxidation or reduction so generating a current, commonly called a photocurrent, whose magnitude is directly proportional to the rate of that electrooxidation or electroreduction.

However, the mass transfer process may be occurring in competition with a relaxation of the photoexcited species – essentially a loss reaction. Species that have undergone the competing relaxation process are then not detected at the electrode surface, resulting in a suppression in the size of the photocurrent detected. As outlined in Section 2.6, the hydrodynamics of a liquid phase near to a rotating disc is well defined and, via the measurement of the electrode current at a range of ORDE rotation speeds, the kinetic rate of the photogeneration and relaxation of photoelectroactive species can be determined.

The ORDE possesses similarities to the RDC system presented in Chapter 4 in that both systems have species formed in the bulk solution phase near to a rotating disc – be that a transparent electrode or a porous membrane – and beyond the interface of the disc with the solution in which it is immersed. In the case of the ORDE this is the generation of

photoexcited species, and in the case of the RDC, this is the generation of extractable metal-ligand complexes. Furthermore, the delivery of light into the bulk solution from the aperture of the ORDE, causing photoexcitation, is comparable with the diffusion of the ligand into the aqueous phase through the porous membrane of the RDC, which causes complexation. Loss of photoexcited species occurs in two ways in the ORDE; because of relaxation from the species photoexcited state back to its ground state as a result of it residing for too long in the bulk solution far from the interface as described above, or as a result of undergoing electrochemistry at the electrode surface. These two phenomena are also similar to phenomena which occur in the RDC. The complex is removed from the aqueous solution either when a decomplexation event occurs for complexed molecules at large distances from the interface or when meeting the membrane surface, at which point it is subsumed by the organic phase contained in the RDC inner cylinder. Table 5.1.1 provides a summary of the comparisons between the ORDE and the RDC.

Table 5.1.1: RDC theory correspondence with the ORDE (Jackson, Boxall, Bromley, Taylor, & Woodhead, 2019).

ORDE process	RDC correspondence
Delivery of light from transparent electrode surface through aqueous diffusion layer into aqueous bulk	Partitioning of ligand from organic bulk through membrane surface and aqueous diffusion layer
Aqueous reaction involving photoexcitation of electroactive species in aqueous diffusion layer, convection layer and bulk	Metal-ligand complex formation in aqueous diffusion layer, convection layer and bulk
Diffusion of electroactive photoexcited species back to electrode surface for interfacial deexcitation reaction	Diffusion of complex back to membrane surface for extraction into the organic phase
Back reaction of electroactive photoexcited species if it is formed too far from the electrode surface and photoexcitation is lost during transit to electrode surface	Back reaction if metal-ligand complex is too far from the membrane surface whereby a decomplexation reaction occurs producing again the free ligand and metal ion

Despite the similarities identified above, a key difference between the RDC and the ORDE is that the concentration profile of the ligand species which is transferred from the rotating inner cylinder of the RDC is affected by the hydrodynamics of the receiving electrolyte, whereas the light emanating from the ORDE is not. Due to this difference, it is not possible to *directly* apply the to the RDC the roots to convection-diffusion equations derived for the ORDE literature (Boxall & Albery, 2000; Boxall & Albery, 2000). However, this literature provides

the fundamental ordinary differential equations (ODEs) which may be modified to suit the RDC application and re-solved under more appropriate conditions.

The hydrodynamic environment at and close to the surface of the rotating disc in an ORDE system closely matches that of the RDC, whereby transfer of the photoelectroactive species, in the case of the ORDE, and the ligand-complexed metal ion, in the case of the RDC, occurs via a combination of diffusion and convection from its point of origin, through the aqueous phase and to the electrode or membrane surface (again, for the ORDE and RDC respectively). Diffusion will dominate in the effectively stagnant layer of solution at the disc electrode or membrane surface and convection will gradually become more dominant at distances greater than X_D , the diffusion region thickness, until the speed of fluid towards and perpendicular to the disk/membrane ceases to vary with distance from the rotating disc surface. The original steady-state ODE of diffusion, convection and photoexcitation for the ORDE is given by Equation 5.1.1 where D_S is diffusion coefficient of a solute S ($\text{m}^2.\text{s}^{-1}$), v_x is the convection current speed ($\text{m}.\text{s}^{-1}$) as a function of distance from the interface x and $[S^*]/[S]$ are the concentrations of photoexcited/ground state species in solution ($\text{mmol}.\text{dm}^{-3}$).

$$D_S \frac{d^2[S^*]}{dx^2} - v_x(x) \frac{d[S^*]}{dx} + \phi \epsilon_e [S] I_0 e^{-\epsilon_\lambda [S] x} - k^*[S^*] = 0 \quad (5.1.1)$$

The only term in Equation 5.1.1 which is not valid when applying the theory to the RDC is the third term which tracks the generation of photoexcited solute $[S^*]$ via a Beer-Lambert law, where I_0 is the flux of light at the electrode surface ($(\text{mol photons}).\text{m}^{-2}.\text{s}^{-1}$), ϵ_e is the photoactivity absorption coefficient ($\text{m}^2.\text{mol}^{-1}$) and ϕ is the quantum efficiency of the absorbance process (no units). As described above, the ligand present in the aqueous phase will not vary via the Beer-Lambert Law in the same way. However, the first, second and fourth terms in Equation 5.1.1, representing diffusion, convection and deexcitation, respectively, may be directly imported from the ORDE model as they are all processes which either occur directly (diffusion and convection) or are analogous (deexcitation/decomplexation) in the context of the RDC.

5.2 Derivation of the RDC Diffusion-reaction model

With the starting point being Equation 5.1.1, modifications have been made to ensure a greater level of correspondence of the theory with that of the extraction processes occurring in the RDC.

The chemical reaction scheme for the ORDE is a single reversible reaction, the forward process corresponding to photoexcitation whilst the reverse process corresponding to relaxation of the photoexcited species back to its ground state. This is shown by Equation 5.2.1.



In contrast, the RDC complexation mechanism follows the reaction scheme shown by Equations 5.2.2 to 5.2.5 where L is the ligand, M is the metal ion, C is the full complex, with $C_{1:1}$ being the initially formed 1:1 L:M complex. The subscript org denotes species in the organic phase whilst no subscript denotes species in the aqueous phase. γ refers to the stoichiometry with respect to the ligand of the final formed complex.



A key assumption made with this reaction scheme, shown by Equations 5.2.2 to 5.2.5, is that the formation of the complex in a 1:1 stoichiometry with respect to L and M is the *rate determining step*. Thermodynamically, the final complex consists of between two to four ligands (Zhu, Sasaki, Suzuki, Suzuki, & Kimura, 2004), however, as the model derived here is principally concerned with kinetics, and given that the formation of the initial 1:1 species is

likely to be the rate determining step in the formation of the final complex, this reaction scheme, shown by Equations 5.2.2 to 5.2.5, is reasonable given its application. Table 2 in Hammerstein *et al* has shown that the 1:1 complexation step in a two-step divalent cation chelation process (in an EDTA-like complexation process) has a rate constant which is three orders of magnitude slower than the 2:1 complexation step; thus the 1:1 step is rate determining (Hammerstein, Shin, & Bayley, 2010).

The reaction whereby additional ligands complex to the 1:1 complex, shown by the forwards reaction of Equation 5.2.4, is assumed to be a fast equilibrium process, occurring on a faster timescale than either the preceding formation of the 1:1 complex or any subsequent mass transfer process, hence no reaction constant has been included. The decomplexation of the full complex, shown overall by the reverse reactions of Equation 5.2.4 then 5.2.3, in that order, *is* considered in the theory developed here; however k_b represents the reaction constant for *full* decomplexation i.e. the overall process described by both Equations 5.2.4 then 5.2.3 together, not each reaction considered in isolation.

As mentioned in Table 5.1.1, tracking the concentration of the photoexcited species in the ORDE is analogous to tracking the ligand/metal ion complex C in the RDC, however in the ORDE theory, there is no analogous equation to appropriately track the ligand concentration L in the aqueous phase. As such, there is a requirement for two distinct ODEs to be solved simultaneously, one describing the coupled chemical-mass transfer processes controlling the ligand concentration [L] and one describing the coupled chemical-mass transfer processes controlling the spatial dependence of the complex concentration [C]. These are represented by Equations 5.2.6 and 5.2.7. D_L and D_C are respectively the ligand and complex diffusion coefficients ($\text{m}^2.\text{s}^{-1}$) and v_x (as in the ORDE model) is the convection current speed ($\text{m}.\text{s}^{-1}$) as a function of distance from the interface x . The first two terms of Equations 5.2.6 and 5.2.7 represent diffusion and convection of species, respectively. The third and fourth terms Equations 5.2.6 and 5.2.7 are first order chemical kinetic rate laws where k_f and k_b are the forward and reverse complexation reaction constants, respectively, and γ is the ligand/metal ion stoichiometry.

$$D_L \frac{d^2[L]}{dx^2} - v_x \frac{d[L]}{dx} - \gamma k_f [M][L][\text{NO}_3^-] + \gamma k_b [C] = \frac{d[L]}{dt} \quad (5.2.6)$$

$$D_C \frac{d^2[C]}{dx^2} - v_x \frac{d[C]}{dx} + k_f[M][L][NO_3^-] - k_b[C] = \frac{d[C]}{dt} \quad (5.2.7)$$

Assumptions which may be applied to Equations 5.2.6 and 5.2.7 in order to obtain the roots are as follows:

- The overall macroscopic extraction process has yet to achieve equilibrium. However, at the scale of the interface, the extraction process is assumed to be occurring under steady state conditions i.e. the ligand and concentration profiles at the interface are effectively constant and we can write that $\frac{d[L]}{dt} = \frac{d[C]}{dt} = 0$.
- M and NO_3^- , reactants in Equation 5.2.3, are in excess and do not deplete significantly over the experimental time period. Thus, they do not have a large impact on the kinetics of reaction in this system because 10 mmol.dm^{-3} of metal ion and 1.0 mol.dm^{-3} of nitric acid is at least an order of magnitude larger than [L] and [C], the former of which in the aqueous phase has been found to saturate at $1.46 \text{ mmol.dm}^{-3}$ (Velavendan, et al., 2013) in the case of TBP (discussed in the last chapter) and $0.042 \text{ mmol.dm}^{-3}$ (Sasaki, Sugo, Suzuki, & Tachimori, 2001) in the case of TODGA (to be discussed in the later chapters). A pseudo-reaction constant k_f' , taking [M] and $[NO_3^-]$ as implicit is deployed in the kinetic rate law.
- Since diffusion dominates within the diffusion regions, $x < X_{D,L}$ and $x < X_{D,C}$ for the ligand and complex, respectively, convection can be considered to be negligible in these regions i.e. $v_x = 0$ at $x < X_{D,L}$ and $x < X_{D,C}$.
- In the context of Equation 5.2.6, the term containing $k_b[C]$ represents the regeneration/release of ligand due to the decomplexation of C. However, due to the low concentration of C generated in the aqueous phase over the short extraction times used to calculate the extraction flux, the term associated with the loss of C can be neglected in the convective-diffusion equation for the ligand i.e. we can write that $k_b[C] \approx 0$ in Equation 5.2.6, making that equation homogeneous in L.

The above assumptions applied result in the generation of Equations 5.2.8 and 5.2.9.

$$D_L \frac{d^2[L]}{dx^2} - \gamma k_f'[L] = 0 \quad (5.2.8)$$

$$D_C \frac{d^2[C]}{dx^2} + k_f'[L] - k_b[C] = 0 \quad (5.2.9)$$

The roots for [L] and [C] as given by by Equations 5.2.10 and 5.2.11, were obtained by solving Equations 5.2.8 and 5.2.9 in accordance with the following boundary conditions:

- At $x = 0$, $[L] = [L]_i$ and $[C] = [C]_i$, which are the concentrations of ligand and complex at the interfacial membrane, respectively.
- At $x = X_{D,L}$ and $x = X_{D,C}$, the concentration boundary conditions are $[L] = [L]_D$ and $[C] = [C]_D$, respectively, which represent the concentrations at the edge of the diffusion regions.

Equations 5.2.12 to 5.2.15 describe the constant terms implicit in Equations 5.2.10 and 5.2.11.

$$[L] = Ae^{\left(\frac{\gamma k_f'}{D_L}\right)^{\frac{1}{2}}x} + Be^{-\left(\frac{\gamma k_f'}{D_L}\right)^{\frac{1}{2}}x} \quad 0 \leq x \leq X_{D,L} \quad (5.2.10)$$

$$[C] = Ge^{\left(\frac{k_b}{D_C}\right)^{\frac{1}{2}}x} + He^{-\left(\frac{k_b}{D_C}\right)^{\frac{1}{2}}x} - \frac{k_f' D_L}{\gamma k_f' D_C - k_b D_L} [L] \quad 0 \leq x \leq X_{D,C} \quad (5.2.11)$$

$$A = [L]_i - B \quad (5.2.12)$$

$$B = \frac{[L]_D - [L]_i e^{\left(\frac{\gamma k_f'}{D_L}\right)^{\frac{1}{2}} X_{D,L}}}{e^{-\left(\frac{\gamma k_f'}{D_L}\right)^{\frac{1}{2}} X_{D,L}} - e^{\left(\frac{\gamma k_f'}{D_L}\right)^{\frac{1}{2}} X_{D,L}}} \quad (5.2.13)$$

$$G = [C]_i - H + \frac{k_f' D_L}{\gamma k_f' D_C - k_b D_L} [L]_i \quad (5.2.14)$$

$$H = \frac{[C]_D - [C]_i e^{\left(\frac{k_b}{D_C}\right)^{\frac{1}{2}} X_{D,C}} - \frac{k_f' D_L}{\gamma k_f' D_C - k_b D_L} \left([L]_i e^{\left(\frac{k_b}{D_C}\right)^{\frac{1}{2}} X_{D,C}} - [L]_D \right)}{e^{-\left(\frac{k_b}{D_C}\right)^{\frac{1}{2}} X_{D,C}} - e^{\left(\frac{k_b}{D_C}\right)^{\frac{1}{2}} X_{D,C}}} \quad (5.2.15)$$

By inspecting Equations 5.2.10 to 5.2.15, and taking into consideration the boundary conditions used in their derivation, it is possible to derive indicative sketches of the concentration profiles for each of the ligand, complex and free metal ion in the vicinity of the interface. These are shown in Figure 5.2.1.

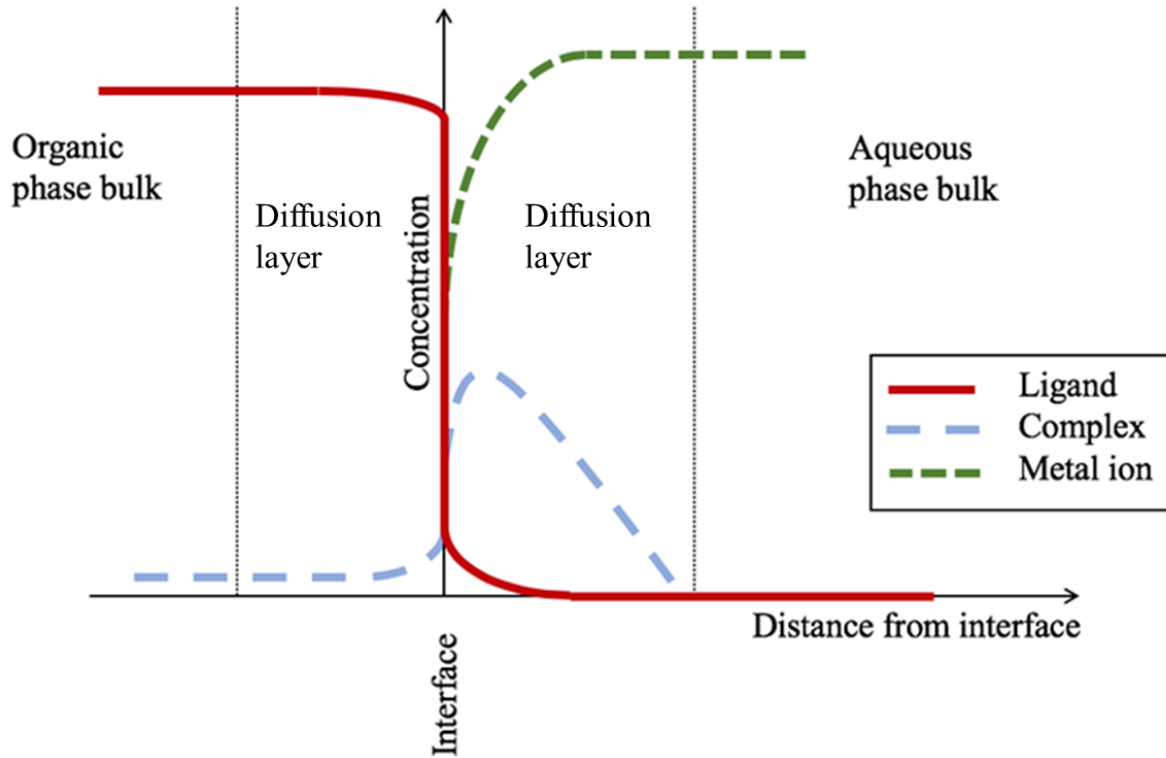


Figure 5.2.1: Theoretical two-film model based on derived RDC theory. The general shape of the curves for the ligand and complex profiles shown originate from Equations 5.2.10 and 5.2.11. The metal ion curve is deduced from the fact that it diminishes close to the interface as it becomes complexed by the ligand.

The extraction flux, j , may be acquired via a mathematical manipulation of the concentration profile of the complex $[C]$, Equation 5.2.11; specifically, differentiating this expression with respect to x , then evaluating this differential at the membrane surface i.e. at $x = 0$; $\left. \frac{d[C]}{dx} \right|_{x=0}$.

Equation 5.2.16 explicitly describes this relationship between C and j according to Fick's

Law and Equation 5.2.17 is the $\left. \frac{dC}{dx} \right|_{x=0}$ component of this expression.

$$j = -D_C \left. \frac{d[C]}{dx} \right|_{x=0} \quad (5.2.16)$$

$$\left. \frac{d[C]}{dx} \right|_{x=0} = \left(\frac{k_b}{D_C} \right)^{\frac{1}{2}} (G - H) - \frac{k_f'^{\frac{3}{2}} \gamma^{\frac{1}{2}} D_L^{\frac{1}{2}}}{\gamma k_f' D_C - k_b D_L} (A - B) \quad (5.2.17)$$

In the following sections, a range of specific forms of the analytical model are presented. They differ only in the boundary conditions assumed for $[C]_i$, the concentration of complex at the interface. The literature provides values for $[L]_i$ (Velavendan, et al., 2013; Sasaki, Sugo, Suzuki, & Tachimori, 2001). $[L]_D$ and $[C]_D$ can be assumed to be zero since the volume of the aqueous phase is large enough to render the bulk concentrations for the experimental time period of the ligand and complex, and thus the concentrations at distance X_D from the interface, negligible. Therefore, the only boundary condition for which no information currently exists is $[C]_i$, hence a range of options for its assignment were attempted.

5.3 Boundary condition where $[C]_i$ is equal to zero

This section outlines the version of the analytical model when $[C]_i = 0$. This corresponds to the case where the complex transfers into the organic phase as soon as it contacts the membrane surface. To allow for ease of simplification of Equations 5.2.10 to 5.2.15 with this boundary conditions, they are first recast into dimensionless form using Equations 5.3.1 to 5.3.3.

$$\xi = X_D/X_f \quad (5.3.1)$$

$$\kappa = X_D/X_k \quad (5.3.2)$$

$$\chi = x/X_D \quad (5.3.3)$$

Note that $X_f = \sqrt{D_L/k_f'}$ and $X_k = \sqrt{D_C/k_b}$, present in Equations 5.3.1 and 5.3.2, represent the forwards and backwards reaction *lengths* of complexation, respectively. In this preliminary analysis, two further assumptions are made additional to those underpinning the derivation of Equations 4.10 to 4.15:

- The diffusion coefficients for ligand and complex are assumed to be equal, $D_L = D_C = D$, allowing for the casting of X_D in 5.3.1 to 5.3.3 above, avoiding the use of solute-specific diffusion layer thicknesses, e.g. $X_{D,L}$.
- Ligand stoichiometry has been assumed to be one, i.e. $\gamma = 1$.

Equation 5.3.4 is produced using the above equations and assumptions, where N is the flux efficiency. The flux efficiency describes the fraction of the encountered/measured flux of

complex incident at the interface with respect to the total possible flux of complex if *all* ligand entering the aqueous phase were to form a complex that was then extracted without a back-reaction/decomplexation occurring. The relationship of extraction flux, j , to N is described by Equation 5.3.5.

$$N = \xi \left(\frac{\xi \coth \xi - \kappa \coth \kappa}{\xi^2 - \kappa^2} \right) \quad (5.3.4)$$

$$j = N \frac{D[L]_i}{X_f} \quad (5.3.5)$$

As discussed, implicit in the $[C]_i = 0$ boundary condition model are three characteristic lengths, X_D which is the diffusion layer thickness as a function of RDC rotation speed, X_f which is the average distance which L must travel in the aqueous phase before 1:1 complexation, and X_k which is the average distance which C travels in the aqueous phase before decomplexation occurs.

As can be seen from Equation 5.3.1, ξ adopts a large value under two conditions; when X_D increases under low RDC rotation speeds and when X_f is small, corresponding to a greater kinetic rate of complexation. Similarly, it can be seen from Equation 5.3.2 that κ will be larger at greater X_D and smaller X_k values, the latter corresponding to a greater kinetic rate of decomplexation. Asymptotes for the flux efficiency equation, Equation 5.3.4, that obtain at a range of values of ξ and κ , i.e. at different relative values for X_D , X_f and X_k are presented in Figure 5.3.1 as a case diagram wherein, to aid visualisation as to the conditions under which each asymptote applies, those asymptotes are mapped in a logarithmic ξ - κ space. The principal approximate conditions considered in deriving Figure 5.3.1 are when ξ is much greater or less than κ and when either is much greater than or less than 1.

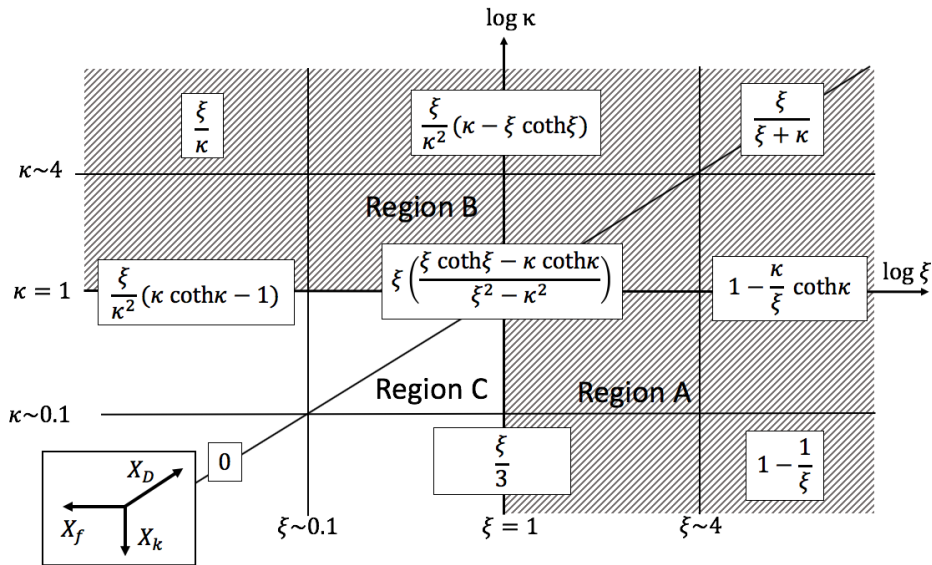


Figure 5.3.1: Case diagram of RDC flux efficiency, N , for the analytical model solved with $[C]_i=0$ boundary condition as a function of X_D , X_f and X_k ($\xi = X_D/X_f$, $\kappa = X_D/X_k$, $X_f = (D_L/k_f')^{1/2}$ and $X_k = (D_C/k_b)^{1/2}$).

The case diagram shown by Figure 5.3.1 has three main regions, A, B and C. Region A corresponds to the highest, most efficient, extraction flux with fast kinetics of complexation, with the majority, or all, of the complex forming within the diffusion region bounded by X_D . Since all of the complex is generated within a small distance close to the interface, which the diffusion region thickness far exceeds, these extractions are typically not dependent on rotation speed. This rotation speed independence is manifest in both the high κ area of Region A where $N = \frac{\xi}{\xi + \kappa}$ and so X_D fully cancels, and the low κ area of Region A where $N = 1 - \frac{1}{\xi}$ term, which is approximately unity. The asymptote at intermediate values of κ , where $N = 1 - \frac{\kappa}{\xi} \coth \kappa$, retains some X_D dependency within the $\coth \kappa$ term, but this diminishes in dominance as ξ becomes larger resulting in *overall* extraction flux that is not dependent on the rotation speed of the RDC.

Region B corresponds to extraction systems whereby decomplexation dominates over complexation, i.e. the generation of long-lasting complex is inhibited by the decomplexation reaction. In the low ξ range of Region B, $N = \frac{\xi}{\kappa}$. As in Region A, the extraction flux is then not dependent on rotation speed as X_D cancels in the $\frac{\xi}{\kappa}$ term. Similarly, at intermediate values

of ξ in Region B, where $N = \frac{\xi}{\kappa^2} (\kappa - \xi \coth \xi) = \frac{\xi^2}{\kappa^2} \left(\frac{\kappa}{\xi} - \coth \xi \right)$, the dependence on rotation speed associated with $\coth \xi$ diminishes to insignificance as κ increases in the $\left(\frac{\kappa}{\xi} - \coth \xi \right)$ term.

Region C corresponds to extraction systems where X_D is small, i.e. for high RDC rotation speeds. In this case, ligand may be lost to the bulk aqueous solution as X_D decreases to become smaller than the complex generation length X_f , decreasing the volume of solution where complexation can occur. Thus, in Region C, extraction flux is *dependent*, inversely, on RDC rotation speed i.e the lower the rotation speed, the larger X_D and so the greater the solution in which complexation may occur and consequently diffuse back to the membrane / interface. On the boundary of Region C with Region A, the asymptote for the flux efficiency is given by $N = \frac{\xi}{3}$, the right-hand side of which contains an X_D term which may not be cancelled. The same is true for the asymptote that obtains at the boundary of Region C with Region B where $N = \frac{\xi}{\kappa^2} (\kappa \coth \kappa - 1)$. Note that when $N = \frac{\xi}{3}$, N is *proportional* to X_D and thus *inversely proportional* to the (square root of the) rotation speed of the RDC, according to the Levich Equation. Conversely, when $N = \frac{\xi}{\kappa^2} (\kappa \coth \kappa - 1)$, N is approximately equal to $\frac{-1}{\kappa}$, and so *inversely proportional* to X_D and *proportional* to the (square root of the) rotation speed of the RDC, according to the Levich Equation.

To summarise, the transition from Region C into either Region A or Region B represents a shift from the flux efficiency dependence on rotation speed, which is the region *not shaded* in Figure 5.3.1, to the flux efficiency independence, which is the region *shaded* in Figure 5.3.1. Specifically at the transition point between Regions C and A, extraction flux *increases* as RDC rotation speed *decreases*. In contrast, at the transition point between Regions C and B, the extraction flux *increases* as RDC rotation speed *increases*.

Given the inverse proportionality of extraction flux on rotation speed seen experimentally in the RDC extractions of Ce(IV) by TBP it is not unreasonable to conclude, based on the above analysis, that the operating point for this system is at or close to the boundary between Regions C and A. This conclusion is supported by the additional observation from the Ce(IV)/TBP system that the RDC extraction flux becomes independent at lower rotation speeds – see Figure 4.3.2 (Bromley & Boxall, 2015). Thus, it is reasonable to conclude that

the operating point of the system studied in Figure 4.3.2 traverses the boundary between Regions C and A, crossing from the former to latter as X_D increases.

The case diagram is useful in illustrating general trends. However, the boundary condition of $[C]_i = 0$, assumed at the start of its derivation is not the most likely condition to obtain. Rather, a non-zero interfacial complex concentration is more likely to be manifest when operating at steady state. With $[C]_i = 0$ a concentration gradient over the membrane would not be manifest and thus there would be no driving force for extraction (this is expanded upon below). Furthermore, the assumptions that $\gamma = 1$ and that there is a common diffusion coefficient value for both the ligand and complex is not the case as it is known that multiple ligands, between 2 and 4, complex to a single metal ion in TBP- and TODGA-based extraction systems. As a result, the $[C]_i = 0$ boundary condition model described in this section does not form part of the subsequent version of the model of the RDC described below and is presented only to aid understanding.

5.4 Boundary condition where $[C]_i$ is a non-zero constant

The relaxation of the $[C]_i = 0$ boundary condition results in a system that accords exactly with the initially-derived general model given by Equations 5.2.10 to 5.2.17 in Section 5.2.

In this system, the complex is again generated in the aqueous diffusion layer near to the interface and, again, the complex which diffuses towards the interface is extracted by the organic phase at the moment of contact with the interface. However, on the organic side of the interface, there is first a membrane which is permeated with the organic extracting phase beyond which lies the bulk organic phase itself. The organic phase permeating the membrane will necessarily be unstirred, i.e. stagnant, whilst the organic phase beyond the membrane will be assumed to be stirred by the convective flows established in the interior of the RDC during its operation (see Figure 2.6.6, Section 2.6). Given that

- (i) the concentration of the extracting complex in the organic phase will be zero at the start of an RDC experiment, and
- (ii) the interior of the cell is well stirred resulting in any extracted complex being swiftly carried away from the organic-facing side of the membrane to the organic phase bulk,

it is reasonable to assume that, on the timescale of the experiments reported here, the concentration of the complex at the surface of the membrane facing towards the organic phase will very closely approximate zero. In light of this, it is then unlikely that $[C]_i$, the concentration of complex at the interface between the organic and aqueous phases at the aqueous phase-facing surface of the membrane, must not be zero at steady state as assumed in the previous section; this would imply either that the diffusion of complex through the membrane occurs infinitely fast, or that it occurs under the influence of a zero concentration gradient within the membrane, or both – none of which are physically possible.

Consequently, though it may be true that the interfacial complex concentration is very close to zero, modelling with the assumption $[C]_i$ is a non-zero and a constant, within any one RDC run (i.e. as a function of rotation speed) provides some reassurance that the model is able to reflect experimental reality – and one approach we adopt in Chapter 6 assumes just this. However, for reasons discussed in the next section, $[C]_i$ may vary within any one RDC run.

5.5 Boundary Condition where $[C]_i$ is a distinct constant at each RDC rotation speed

Building on the previous section, it is possible that the $[C]_i$ boundary condition is not the same constant at all RDC rotation speeds but is a different constant value at each of them. As the complex crosses the aqueous/organic interface, the rate at which the complex containing the metal ion extracted is assimilated into the bulk organic phase must, at steady state, be the same as the rate of transfer *to* the membrane on the aqueous side and thence *through* the membrane.

On the organic side of the membrane, at $x = -X_{\text{mem}}$, where X_{mem} is the thickness of the membrane, the complex concentration at short extraction times will be zero due to the well-mixed nature of the bulk organic phase. The complex concentration will be so dilute in the organic bulk phase that the concentration gradient of complex *through the membrane* must be bounded at $x = -X_{\text{mem}}$ by a $[C]_{\text{org}} = 0$ boundary condition where $[C]_{\text{org}}$ denotes the organic complex concentration.

Since the linear concentration gradient of complex *through the membrane* is proportional to flux j via Fick's second law, then $[C]_i$, the complex concentration at the aqueous/organic interface ($x = 0$), must vary proportional to j if $[C]_{\text{org}} = 0$ at $x = -X_{\text{mem}}$. Since the membrane thickness, X_{mem} , unlike the aqueous diffusion layer, does not vary with RDC

rotation speed, $[C]_i$, is the sole determinant of the concentration gradient of complex through the membrane. Consequently, $[C]_i$ is the single unknown constant which must possess an implicit dependence on extraction flux. Such a dependency is expressed via a general extraction constant k_{ex} as shown by Equation 5.5.1.

$$j = k_{ex}[C]_i \quad (5.5.1)$$

Although the model which has a distinct $[C]_i$ constant for each RDC rotation speed described here offers a more robust description of the extraction mechanism in the RDC, *both* models provide insight in the subsequent chapters of this thesis. Both are models provide insights into the system under study and have led to a much better explanation of the underlying extraction mechanisms at play. Thus, the implementation of constant, non-zero $[C]_i$ boundary condition version of the model in the roots of the equations describing RDC extractions is described in (i) section 6.1.1 for the Ce(IV)/TBP system and (ii) section 7.4.1 for the Nd(III)/TODGA system. The implementation of the model where $[C]_i$ is a distinct constant at each rotation speed is described in (i) section 6.1.2 for the Ce(IV)/TBP system and (ii) section 7.4.2 for the Nd(III)/TODGA system.

5.6 Integrating Theory with Computational Modelling

The mathematics derived in this chapter allows the theory which underpins the RDC extraction flux behaviour to be tested. Up to this point the model has been entirely analytical in nature requiring no computational methods to obtain the roots. However, PSE gPROMS, a computational software package, was used in conjunction with the analytical expressions in these studies to calculate the optimal values for the unknowns such as the kinetic rate constants k'_f and k_b as defined in Section 5.2.

5.6.1 Degrees of Freedom Analysis

A Degrees of Freedom (DoF) analysis was performed for the RDC analytical models to provide assurance that the set of equations are solvable, numerically or otherwise. In a set of linear equations, containing four unknown constants, for example, four equations containing all four unknown constants at least once are required to find the roots. If the value of one unknown constant is known beforehand, it may be removed from the pool of unknowns, leaving one less equation required to completely solve for all unknown constants.

Consequently, the unknown constants introduced into the RDC model, such as the kinetic rate constants, must be determined either by one or multiples of the model equations or be assigned to a value based on pre-existing information. The RDC analytical model from Section 5.2, with the boundary condition where $[C]_i$ is one distinct constant at all RDC rotation speeds, is presented in the form of a DoF analysis in Table 5.6.1.1. The number of equations equals the number of variables in Table 5.6.1.1. This indicates that the model is robustly defined and solvable. As mentioned above, solving of the equations comprising the model for the Ce(IV)/TBP and Nd(III)/TODGA systems is given in Chapters 6 and 7, respectively.

Table 5.6.1.1: Degrees of Freedom (DoF) analysis for the RDC analytical model, with constant $[C]_i$ boundary condition.

Constants	Equations	New unknown variables	Number of new equations	Number of new variables
$D_L, D_C, \gamma, k_f', k_b$	$\frac{d[C]}{dx} \Big _{x=0} = \left(\frac{k_b}{D_C}\right)^{\frac{1}{2}} (G - H) - \frac{k_f'^{\frac{3}{2}} \gamma^{\frac{1}{2}} D_L^{\frac{1}{2}}}{\gamma k_f' D_C - k_b D_L} (A - B)$	$\frac{d[C]}{dx} \Big _{x=0}, A, B, G, H$	1	5
	$-D_C \frac{d[C]}{dx} \Big _{x=0} = j$	j	1	1
$[L]_i$	$A = [L]_i - B$		1	0
$[L]_D$	$B = \frac{[L]_D - [L]_i e^{\left(\frac{\gamma k_f'}{D_L}\right)^{\frac{1}{2}} X_{D,L}}}{e^{-\left(\frac{\gamma k_f'}{D_L}\right)^{\frac{1}{2}} X_{D,L}} - e^{\left(\frac{\gamma k_f'}{D_L}\right)^{\frac{1}{2}} X_{D,L}}}$	$X_{D,L}$	1	1
$[C]_i$	$G = [C]_i - H + \frac{k_f' D_L}{\gamma k_f' D_C - k_b D_L} [L]_i$		1	0
$[C]_D$	$H = \frac{[C]_D - [C]_i e^{\left(\frac{k_b}{D_C}\right)^{\frac{1}{2}} X_{D,C}} - \frac{k_f' D_L}{\gamma k_f' D_C - k_b D_L} \left([L]_i e^{\left(\frac{k_b}{D_C}\right)^{\frac{1}{2}} X_{D,C}} - [L]_D \right)}{e^{-\left(\frac{k_b}{D_C}\right)^{\frac{1}{2}} X_{D,C}} - e^{\left(\frac{k_b}{D_C}\right)^{\frac{1}{2}} X_{D,C}}}$	$X_{D,L}$	1	1
ω, v, D_L	$X_{D,L} = 0.643 \omega^{-\frac{1}{2}} v^{\frac{1}{6}} D_L^{\frac{1}{3}}$		1	0
D_C	$X_{D,C} = 0.643 \omega^{-\frac{1}{2}} v^{\frac{1}{6}} D_C^{\frac{1}{3}}$		1	0
Total			8	8

In the next section, we return to the analysis of the unknown kinetic rate constants which define the TBP/Ce(IV) RDC extractions.

Chapter 6: RDC Extractions of Ce(IV) by TBP Part 2: Unknown Kinetic Constant Estimation

In this chapter we revisit the RDC extraction data for the Ce(IV)/TBP system presented in part in Chapter 4. The theory outlined in the previous chapter, used in conjunction with the gPROMS modelling environment, was able to estimate values for the unknown kinetic constants relevant to the Ce(IV)/TBP extraction process. The details of this analysis are presented in this section.

6.1 Unknown Kinetic Constant Estimation Using Semi-analytical gPROMS Model

The unknown constants are the complexation and decomplexation rate constants, k'_f and k_b , respectively, and $[C]_i$, the interfacial complex concentration at the aqueous/organic interface and membrane surface. Using the data of Chapter 4, these unknown constants have been estimated using the gPROMS parameter estimation toolkit and the results are presented in this section.

Values of the known constants were sourced or estimated as follows:

- $[L]_i$ is known and is the TBP ligand solubility of $1.46 \text{ mmol.dm}^{-3}$ in nitric acid (Velavendan, et al., 2013).
- $[L]_D / [C]_D$ are also known to be the concentrations of species at the edge of their effective diffusion layers and may be set to zero given the large volume of the bulk aqueous phase and the well-mixed nature of the convection layer.
- *Aqueous* diffusion coefficients of free TBP and TBP/Ce(IV) complexes are not defined in the literature. Typically, diffusion coefficients in the aqueous phase are observed for the metal ion/nitrate $\text{Ce}^{4+}(\text{NO}_3^-)_4$ complex, not for the TBP/Ce(IV)/nitrate ion complex which is assumed to exist only in the *organic* phase as $\text{Ce}^{4+}(\text{NO}_3)_4.2\text{TBP}$, despite the solubility of TBP suggesting otherwise (Nikolaev, Afanas'ev, Durasov, & Ryabinin, 1963). The diffusion coefficient of the organic complex $\text{Ce}^{4+}(\text{NO}_3)_4.2\text{TBP}$ has been cited as being $2.5 \times 10^{-10} \text{ m}^2.\text{s}^{-1}$ by Nikolaev *et al* (Nikolaev, Afanas'ev, Durasov, & Ryabinin, 1963). The diffusion coefficient of free TBP is typically cited in organic solvent with a value of $4.7 \times 10^{-10} \text{ m}^2.\text{s}^{-1}$ being given by Singh *et al* from experiments conducted using 0.5 mol.dm^{-3} TBP in dodecane

(Singh, Nayak, Kanthe, Patil, & Gaikar, 2017). This value is in close agreement with the study by Nikolaev *et al* which reports a diffusion coefficient for TBP in a 30% (by volume) solution in dodecane as $4.3 \times 10^{-10} \text{ m}^2 \cdot \text{s}^{-1}$ (Nikolaev, Afanas'ev, Durasov, & Ryabinin, 1963).

According to the Stokes-Einstein Equation described by Equation 2.6.2 in Section 2.6, diffusivity is inversely proportional to dynamic viscosity. In the absence of diffusion information for the free ligand and complex in the acidic *aqueous* phase, as an approximation, aqueous diffusivities have been scaled from the organic diffusivities using the dynamic viscosity difference between aqueous and organic phases. Table 6.1.1 gives the dynamic and kinematic viscosities of OK and water as well as their densities. Water is 25% less viscous (dynamic) than OK, which produces, after scaling using the Stokes-Einstein equation, aqueous diffusivities of TBP, denoted by D_L , of $5.6 \times 10^{-10} \text{ m}^2 \cdot \text{s}^{-1}$, and $\text{Ce}^{4+}(\text{NO}_3)_4 \cdot 2\text{TBP}$, denoted by D_C , of $3.1 \times 10^{-10} \text{ m}^2 \cdot \text{s}^{-1}$.

Table 6.1.1: Table containing viscosity and density information for odourless kerosene and water.

Solvent	Kinematic viscosity ($\text{m}^2 \cdot \text{s}^{-1}$)	Density at 25°C and 1 bar ($\text{kg} \cdot \text{m}^{-3}$)	Dynamic viscosity at 25°C and 1 bar (Pa.s)	Reference
Odourless kerosene	1.6×10^{-6}	769	1.2×10^{-3}	(LabChem, 2021)
Water	8.9×10^{-7}	997	8.9×10^{-4}	(NIST, 2021)

The ligand stoichiometry γ is set to 2.0 as this is the final ratio between TBP and Ce(IV) in the final complex commonly given in the literature. See, for example Healy *et al* and Nikolaev *et al* (Healy & McKay, 1956; Nikolaev, Afanas'ev, Durasov, & Ryabinin, 1963).

6.1.1 Estimating Unknown Constants Where $[C]_i$ is a Constant Across All RDC Rotation Speeds

A fit was obtained using the model where $[C]_i$ is a constant; the model is described in Section 5.4. k'_f , k_b and $[C]_i$ which achieve the fit are shown in Tables 6.1.1.1 and 6.1.1.2. Table 6.1.1.1 describes the estimations when D_L and D_C are set to the literature values of their diffusivities in the *organic* phase and Table 6.1.1.2 describes the estimations when D_L and D_C are set to Stokes-Einstein-derived estimates for the *aqueous* diffusivities. Figure 6.1.1.1 shows the graphical fits. For these fits, an arbitrary error of 5% was applied in the absence of

experimental error – due to the fact that no repeats were performed by Bromley. See Section 4 for details.

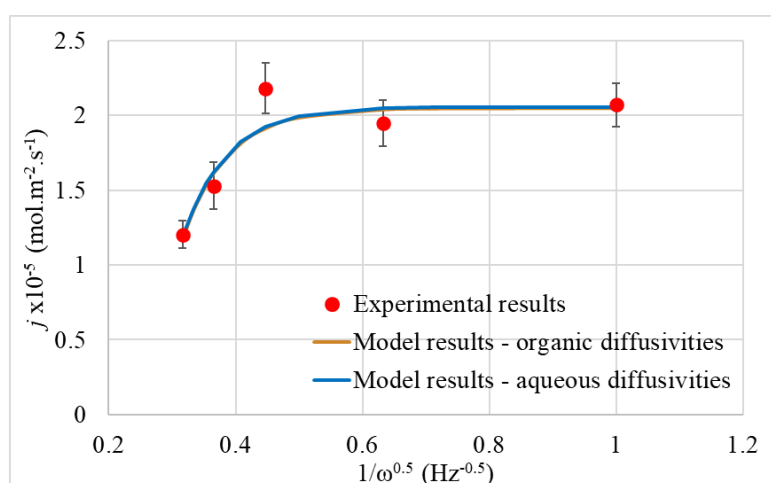


Figure 6.1.1.1: RDC experimental extraction flux as a function of RDC inverse square root of rotation speed, $\omega^{-0.5}$. Flux of Ce(IV) into the organic phase of 0.2 mol.dm⁻³ TBP in OK from an initial aqueous phase of 10 mmol.dm⁻³ Ce(IV) in 1.0 mol.dm⁻³ nitric acid. Organic diffusivities are obtained directly from the literature and aqueous diffusivities are derived via the Stokes-Einstein relation. Best fit found using the model where $[C]_i$ is a constant in gPROMS.

The unknown constants which have been estimated and presented in Tables 6.1.1.1 and 6.1.1.2 both show a good fit in Figure 6.1.1.1 due to the χ^2 values being lower than the χ^2 -critical values (see Section 3.4.4). Despite the goodness of the fits, the confidence intervals, and the standard deviations of the unknown constants (k'_f , k_b and $[C]_i$), are larger than their estimated values, implying that there is a large amount of uncertainty in the mean values obtained. This is supported by the t-value test results in both Tables 6.1.1.1 and 6.1.1.2 which fail for every unknown constant (see Section 3.4.2).

Table 6.1.1.1: Constants associated with the optimum model fit of TBP/Ce(IV) system shown by the organic diffusivities model results shown in Figure 6.1.1.1. The χ^2 value being smaller than the χ^2 -critical value indicates a good model fit.

	D_L ($m^2.s^{-1}$)	D_C ($m^2.s^{-1}$)	γ	k'_f (s^{-1})	k_b (s^{-1})	$[C]_i$ ($mmol.dm^{-3}$)
Value	4.5×10^{-10}	2.5×10^{-10}	2.0	860	9.8	11
Standard deviation	-	-	-	4400	10	26
90% confidence interval	-	-	-	13000	30	77
95% confidence interval	-	-	-	19000	44	110
99% confidence interval	-	-	-	44000	100	260
95% t-value	-	-	-	0.046	0.22	0.10
Reference t-value (95%)	2.9					
χ^2	3.0					
χ^2 -critical	6.0 (5 data - 3 fitting parameters = 2 d.o.f.)					

Table 6.1.1.2: Constants associated with the optimum model fit of TBP/Ce(IV) system shown by the aqueous diffusivities model results shown in Figure 6.1.1.1. The χ^2 value being smaller than the χ^2 -critical value indicates a good model fit.

	D_L ($m^2.s^{-1}$)	D_C ($m^2.s^{-1}$)	γ	k'_f (s^{-1})	k_b (s^{-1})	$[C]_i$ ($mmol.dm^{-3}$)
Value	5.6×10^{-10}	3.1×10^{-10}	2.0	640	11	9.2
Standard deviation	-	-	-	3300	11	22
90% confidence interval	-	-	-	9600	33	64
95% confidence interval	-	-	-	14000	49	94
99% confidence interval	-	-	-	33000	110	220
95% t-value	-	-	-	0.045	0.22	0.097
Reference t-value (95%)	2.9					
χ^2	3.0					
χ^2 -critical	6.0 (5 data - 3 fitting parameters = 2 d.o.f.)					

The data in Tables 6.1.1.1 and 6.1.1.2 were derived assuming the value of $[C]_i$ is the same at all rotation speeds studied as well as the assumption made in the simplification of Equations 5.2.6 and 5.2.7 in Section 5.2. One of these assumptions is that the concentration of the extracting metal ion in the aqueous phase, $[M]$, does not deplete significantly over the time period of the experiment and thus may be treated as being not dependent on distance from the membrane into the aqueous phase. I.e. it exhibits the bulk concentration of Ce(IV) in the aqueous phase right up to the membrane surface and for the data being modelled here, this concentration is 10 mmol.dm^{-3} . The estimated values of $[C]_i$ in Tables 6.1.1.1 and 6.1.1.2 are 11 and 9.2 mmol.dm^{-3} , respectively, implying that, given the 1:1 stoichiometry of metal to complex that the concentrations of metal ions at the membrane surface are -1.0 and 0.8 mmol.dm^{-3} , respectively. Not only is the former physically impossible, both values clearly violate the assumption made about the spatial non-variation of $[M]$ in the aqueous phase that underpins the simplification of Equations 5.2.6 and 5.2.7. One way to address this issue is to fix $[C]_i$ in the unknown constant estimation process.

In a series of follow-up estimations of the unknown constants presented in Table 6.1.1.3 and in Figure 6.1.1.2, the $[C]_i$ constant is set to a range of concentrations representing 5%, 10% and 25% of the initial Ce(IV) aqueous load. Under these conditions, the Ce(IV) lost to complexation in the aqueous diffusion region can be assumed to adhere to the assumption that the metal ion concentration is unperturbed. The diffusion coefficients for the estimation of the unknown constants to follow have been set to their aqueous Stokes-Einstein derived values *only* due to the fact that varying the diffusivities of the ligand and complex has a minimal impact on the estimation of the kinetic and $[C]_i$ constants.

The model fit in the case where $[C]_i$ is set to 0.5 mmol.dm^{-3} in Figure 6.1.1.2 is the worst fit of the three $[C]_i$ concentrations investigated. Furthermore, the 95% t-values for k'_f and k_b shown in Table 6.1.1.3 increase as $[C]_i$ increases indicating an increasing confidence in the unknown constant estimation obtained as interfacial complex concentration gets larger.

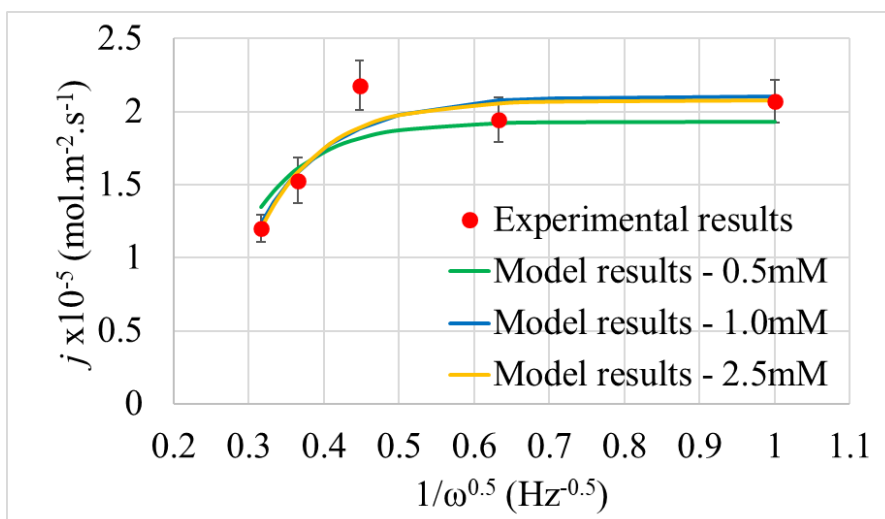


Figure 6.1.1.2: RDC experimental extraction flux, j , of Ce(IV) into the organic phase of 0.2 mol.dm^{-3} TBP in OK from an initial aqueous phase of 10 mmol.dm^{-3} Ce(IV) in 1.0 mol.dm^{-3} nitric acid, as a function of RDC inverse square root of rotation speed, $\omega^{-0.5}$. $[C]_i$ fixed at 5%, 10% and 25% of the initial Ce(IV) concentration. Best fit achieved using the model where $[C]_i$ is a constant in gPROMS.

Table 6.1.1.3: Constants associated with the optimum model fit of TBP/Ce(IV) system shown by the aqueous diffusivities model results shown in Figure 6.1.1.2. $[C]_i$ boundary condition set to a range of values; 5%, 10% and 25% the initial Ce(IV) concentration. Other constants: $D_L=5.6 \times 10^{-10} \text{ m}^2.\text{s}^{-1}$, $D_C=3.1 \times 10^{-10} \text{ m}^2.\text{s}^{-1}$, $\gamma=2.0$.

	k'_f (s^{-1})			k_b (s^{-1})			$[C]_i$ (mmol.dm^{-3})		
	10	14	47	7.2	4.7	5.7	0.50	1.00	2.5
Standard deviation	1.5	1.3	4.4	1.9	0.72	0.68	-	-	-
90% confidence interval	3.6	3.1	10	4.4	1.7	1.6	-	-	-
95% confidence interval	4.8	4.1	14	5.9	2.3	2.2	-	-	-
99% confidence interval	8.9	7.6	25	11	4.2	3.9	-	-	-
95% t-value	2.1	3.3	3.4	1.2	2.0	2.7	-	-	-
χ^2	-						8.2	4.0	3.5
Reference t-value (95%)	2.4								
χ^2 -critical	7.8 (5 data - 2 fitting parameters = 3 d.o.f.)								

Following the assignment of a value for $[C]_i$, as shown in Table 6.1.1.3, much smaller confidence intervals for the remaining unknown constants, k'_f and k_b , are obtained compared to when $[C]_i$ was not predefined as was the case in Tables 6.1.1.1 and 6.1.1.2. Furthermore, the standard deviation of k'_f in Table 6.1.1.3 is approximately 10% of the final value in each case and the standard deviation for k_b is 10-20%. This is a vast improvement on the equivalent errors in Tables 6.1.1.1 and 6.1.1.2 which in some cases exceeded 100%.

Having modelled the data of Figures 4.3.1 and 4.3.2 using the assumption that $[C]_i$ is non-zero and not dependent on RDC rotation speed, the next section now builds on these findings by modelling the data with these constraints relaxed, i.e. the modelling is conducted, in the context of its more likely scenario, that $[C]_i$ varies as a function of RDC rotation speed.

6.1.2 Estimating Unknown Constants Where $[C]_i$ is a Distinct Constant at Each RDC Rotation Speed

In the context of the model where $[C]_i$ is a distinct constant at each rotation speed, derived in Section 5.5 and deployed in this section, the unknown kinetic constants requiring estimation are the same as before; k'_f and k_b . k_{ex} , present in the model as described by Equation 5.5.1 in Section 5.5 requires estimation in place of $[C]_i$.

The initial results of the estimation process are shown in Table 6.1.2.1. Only the unknown constants estimated using the fixed aqueous diffusivities will be presented in this section as there was found to be minimal difference in the estimated values when using organic diffusivities. Figure 6.1.2.1 gives the optimal model fits obtained when the unknown constants are set to the optimal values alongside the experimental extraction flux data for comparison.

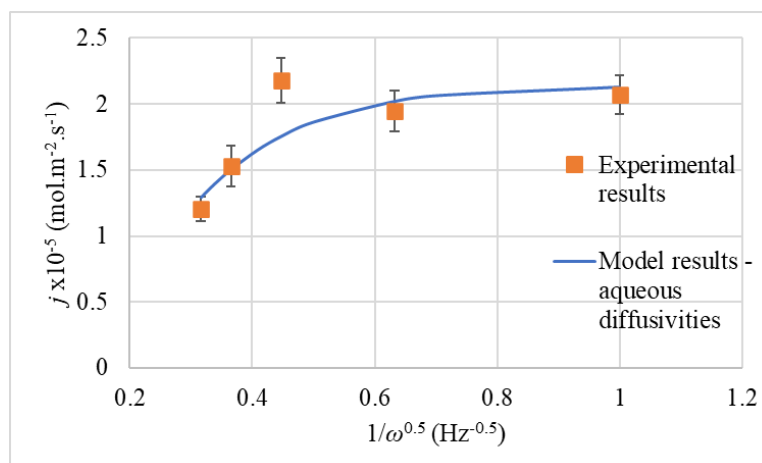


Figure 6.1.2.1: RDC experimental extraction flux as a function of RDC inverse square root of rotation speed, $\omega^{-0.5}$. j of Ce(IV) into the organic phase of 0.2 mol.dm^{-3} TBP in OK from an initial aqueous phase of 10 mmol.dm^{-3} Ce(IV) in 1.0 mol.dm^{-3} nitric acid. Best fit achieved using the model where $[C]_i$ is a distinct constant at each RDC rotation speed in gPROMS.

Table 6.1.2.1: Constants associated with the optimum model fit of TBP/Ce(IV) system shown by the aqueous diffusivities model results shown in Figure 6.1.2.1. The χ^2 value being larger than the χ^2 -critical value indicates a poor model fit.

	D_L ($\text{m}^2.\text{s}^{-1}$)	D_C ($\text{m}^2.\text{s}^{-1}$)	γ	k'_f (s^{-1})	k_b (s^{-1})	k_{ex} ($\text{m}.\text{s}^{-1}$)
Value	5.6×10^{-10}	3.1×10^{-10}	2.0	5.6	1.8	3.0×10^{-5}
Standard deviation	-	-	-	6.67	2.65	9.0×10^{-5}
90% confidence interval	-	-	-	20	7.7	2.6×10^{-4}
95% confidence interval	-	-	-	29	11	3.9×10^{-4}
99% confidence interval	-	-	-	67	26	9.0×10^{-4}
95% t-value	-	-	-	0.19	0.16	0.077
Reference t-value (95%)	2.9					
χ^2	7.6					
χ^2 -critical	6.0 (5 data - 3 fitting parameters = 2 d.o.f.)					

Inspection of Figure 6.1.2.1 reveals the following. First, the fits obtained using the model where $[C]_i$ is a distinct constant at each rotation speed is not as good as the fits using the model where $[C]_i$ is constant shown by Figure 6.1.1.2. This is especially apparent at low

rotation speeds where the experimental flux becomes not dependent on the decreasing RDC rotation speed. The model fits generated using the constant $[C]_i$ condition provides good matches to this behaviour. However, those generated using the model where $[C]_i$ is a distinct constant at each rotation speed over-estimate the flux at low RDC rotation speed. The lower validity of these fits is further supported by the χ^2 values being greater than the χ^2 -critical values in Table 6.1.2.1, which indicates a poor model fit. Secondly, the confidence intervals and standard deviations are far greater than the values of the unknown constants estimated implying a poor confidence in the mean values produced. Finally, as with the results shown in Tables 6.1.1.1 and 6.1.1.2 in the previous section, the t-value tests for each unknown constant in Table 6.1.2.1 from *this* section all fail.

However, following the approach adopted in the case of the application of the constant $[C]_i$ condition to the modelling of the data, it may be possible to improve the errors on the remaining constants which are the fitting parameters by assigning a value to one of them, so reducing the number of unknown constants that need to be estimated. In the case of this model where $[C]_i$ is a distinct constant at each rotation speed, the most obvious unknown constant to fix is k_{ex} as it is desirable to obtain estimated values of k'_f and k_b from the data. Again, adopting a similar approach analogous to that deployed in the last section, k_{ex} can be assigned to a value that ensures that, at all rotation speeds studied, $[C]_i$ is never greater than a small percentage (<25% for example) of the bulk initial concentration in the aqueous phase. As can be seen in Figure 6.1.2.2, the mean value of k_{ex} of $3.0 \times 10^{-5} \text{ m.s}^{-1}$ results in a maximum $[C]_i$ in concurrence with the assumption of metal ion non-perturbance. Figure 6.1.2.2 shows the variation of $[C]_i$ being between $0.4\text{-}0.7 \text{ mmol.dm}^{-3}$ which, given the 1:1 conversion of metal ion to complex results in only a fraction of the 10 mmol.dm^{-3} Ce(IV) being depleted at the interfacial membrane.

Figure 6.1.2.1 already shows the fit obtained when $k_{ex} = 3.0 \times 10^{-5} \text{ m.s}^{-1}$ and aqueous diffusivities are deployed, thus the graph will not be replotted. Table 6.1.2.2 shows the resulting estimations of unknown constants which, though identical to that shown in Table 6.1.2.1 in terms of their values, reveal better quality error data and confidence information.

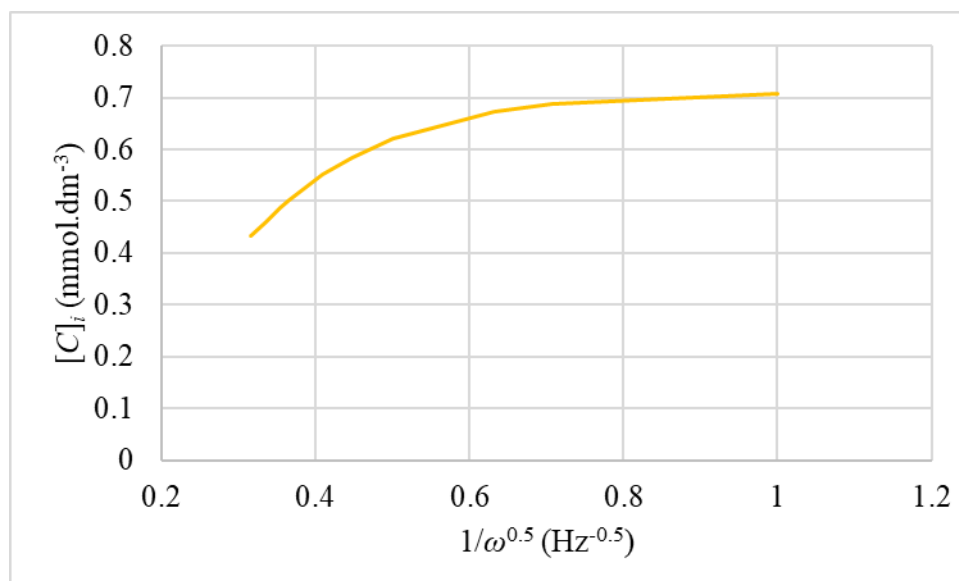


Figure 6.1.2.2: The variation of interfacial complex concentration $[C]_i$ as a function of inverse square root of rotation speed $\omega^{-0.5}$ corresponding to the estimations of the unknown constants shown in Table 6.1.2.1.

Table 6.1.2.2: Constants associated with the optimum model fit of TBP/Ce(IV) system shown by the organic diffusivities model results shown in Figure 6.1.2.1. k_{ex} boundary condition set at $3.0 \times 10^{-5} \text{ m.s}^{-1}$. The χ^2 value being smaller than the χ^2 -critical value indicates a good model fit.

	D_L ($\text{m}^2.\text{s}^{-1}$)	D_C ($\text{m}^2.\text{s}^{-1}$)	γ	k'_f (s^{-1})	k_b (s^{-1})	k_{ex} (m.s^{-1})
Value	5.6×10^{-10}	3.1×10^{-10}	2.0	5.6	1.8	3.0×10^{-5}
Standard deviation	-	-	-	0.60	0.54	-
90% confidence interval	-	-	-	1.4	1.3	-
95% confidence interval	-	-	-	1.9	1.7	-
99% confidence interval	-	-	-	3.5	3.2	-
95% t-value	-	-	-	2.9	1.0	-
Reference t-value (95%)	2.4					
χ^2	7.6					
χ^2 -critical	7.8 (5 data - 2 fitting parameters = 3 d.o.f.)					

The standard deviation of the k'_f value in Table 6.1.2.2 is approximately ~10% and for k_b it is ~30%, which is a large improvement on the previous results in Table 6.1.2.1, where k_{ex} was allowed to converge. Furthermore, as with the constant $[C]_i$ model, the t-value for k'_f is greater than the reference t-value whereas the opposite is true for k_b revealing that k'_f is a dominant kinetic constant when determining the overall model fit and k_b is not.

k'_f and k_b values described in Table 6.1.2.2 for the application of the model where $[C]_i$ is a distinct constant at each rotation speed are marginally lower than these constants as found in Section 6.1.1 where the constant $[C]_i$ condition was applied, however k'_f remains approximately five times greater than k_b , implying that the rate of complexation is greater than that of decomplexation.

Employing the estimations found for the unknown constants in the original model equations from Section 5.2 allows us to accurately plot the expected concentration profiles of the TBP ligand and the TBP/Ce(IV)/nitrate complex over the aqueous diffusion layer. This is the subject of the next section.

6.2 Analysis of Ligand and Complex Concentration Profiles

In this section concentration profiles, shown by Figures 6.2.1 and 6.2.2, for all key species, L and C, have been generated using the estimated kinetic rate constants derived using both models; for which $[C]_i$ is a constant and for which $[C]_i$ is a distinct constant at each RDC rotation speed. Table 6.1.1.3 and Table 6.1.2.2 contain the estimations for the unknown constants used to plot the concentration profiles obtained using each model.

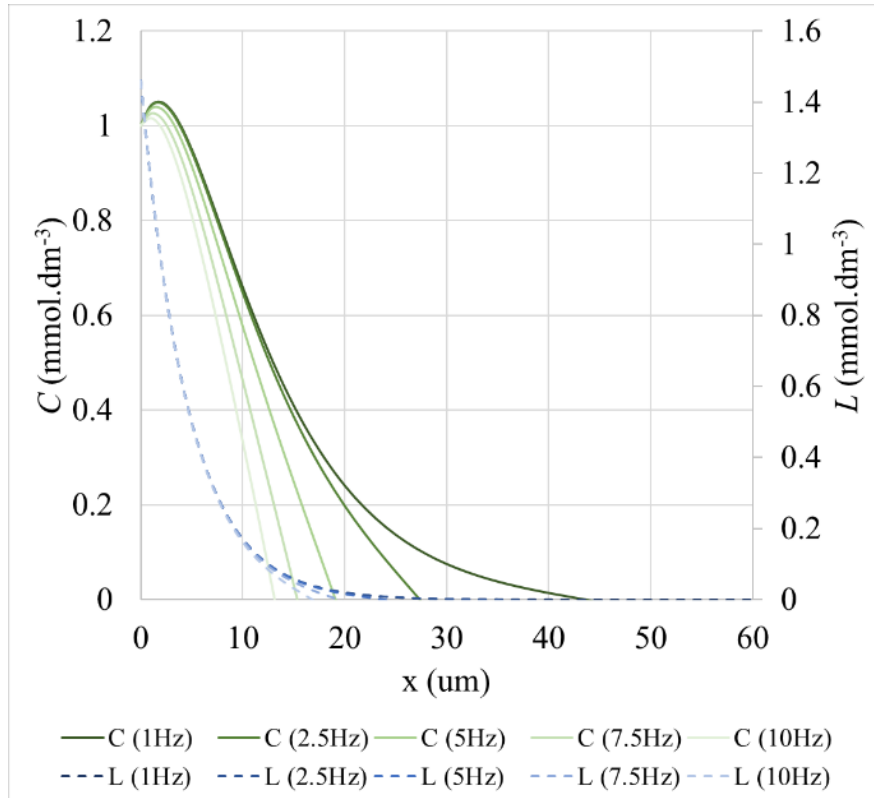


Figure 6.2.1: Aqueous phase diffusion layer concentration profiles resulting from the constant $[C]_i$ model of TBP (shown by L) and Ce(IV)/TBP complex (shown by C) with diffusivities derived via the Stokes-Einstein equation. List of constants: $D_L = 5.6 \times 10^{-10} \text{ m}^2 \cdot \text{s}^{-1}$, $D_C = 3.1 \times 10^{-10} \text{ m}^2 \cdot \text{s}^{-1}$, $\gamma = 2.0$, $k_f' = 14 \text{ s}^{-1}$, $k_b = 4.7 \text{ s}^{-1}$, $[C]_i = 1.0 \text{ mmol} \cdot \text{dm}^{-3}$.

Based on the results of Table 6.1.2.2 and Figure 6.2.1, the values of $[C]_{\max}$ and X_D can be considered to be controlled by the competition between three things:

- (i) the rate of reaction of TBP with Ce(IV) in the aqueous phase as TBP extracts into the aqueous from the organic phase/membrane;
- (ii) once formed, diffusion of the complex to the membrane surface prior to extraction into the organic phase;
- (iii) a competing diffusion process whereby the formed complex diffuses to the outer edge of the diffusion layer at $x = X_D$ prior to it being lost to the convectively stirred bulk solution at $x > X_D$.

Thus, at higher rotation rates the value of $\frac{d[C]}{dx}$ at $x = X_D$ is steep and large and a significant fraction of complex generated is lost to the solution bulk at $x > X_D$. However, as the rotation speed is decreased, $\frac{d[C]}{dx}$ at $x = X_D$ becomes less steep with the consequence that the fraction

of complex lost to the bulk decreases. This results in an increase in $[C]_{\max}$ within the diffusion layer which in turn gives rise to an increase in $\frac{d[C]}{dx}$ at $x = 0$ and thus the extraction flux.

In Figure 6.2.1, at the higher RDC rotation speeds, phase-transferred TBP is lost to the solution bulk before it can complex with Ce(IV). However, at lower rotation speeds, X_D becomes large enough that the concentration profile for TBP is contained wholly within the diffusion layer – meaning that the TBP is lost to the solution bulk at $x > X_D$ and that all TBP that is phase-transferred is then reacting to form complex in the diffusion layer. Once this point of maximum complex generation is reached, any further decreases in rotation speed, and thus increases in X_D , will have no further effect on the amount of complex generated in the diffusion layer. This has the consequence that the extraction flux will become not dependent on decreasing RDC rotation speed, as is seen in the experimental data of Figure 6.1.1.2.

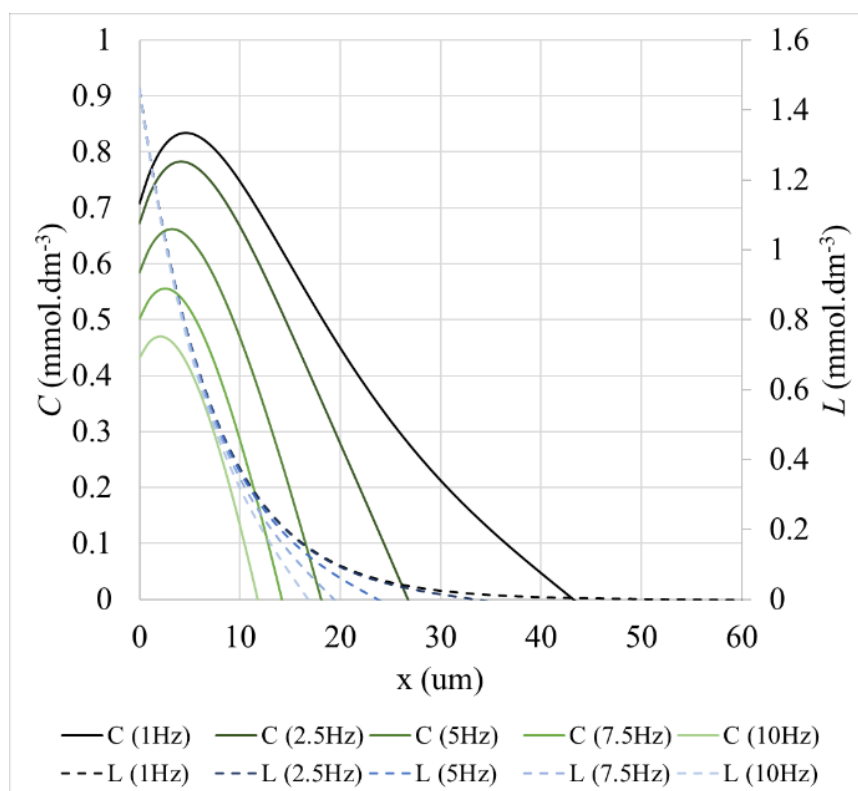


Figure 6.2.2: Aqueous phase diffusion layer concentration profile resulting from the model where $[C]_i$ is a distinct constant at each rotation speed of TBP (shown by L) and Ce(IV)/TBP complex (shown by C) with diffusivities derived via the Stokes-Einstein equation. List of constants: $D_L = 5.6 \times 10^{-10} \text{ m}^2 \cdot \text{s}^{-1}$, $D_C = 3.1 \times 10^{-10} \text{ m}^2 \cdot \text{s}^{-1}$, $\gamma = 2.0$, $k_f' = 5.6 \text{ s}^{-1}$, $k_b = 1.8 \text{ s}^{-1}$, $k_{ex} = 3.0 \times 10^{-5} \text{ m} \cdot \text{s}^{-1}$.

The same explanation for the form of the concentration profiles given above for Figure 6.2.1 also generally applies for Figure 6.2.2. However, some differences between the profiles calculated for the two systems do exist.

The principal key difference between the concentration profiles in Figure 6.2.2, calculated using the model where $[C]_i$ is a distinct constant at each rotation speed, compared to that calculated using the model where $[C]_i$ is constant in Figure 6.2.1 is that the ligand concentration profile exhibits a slightly greater dependence on RDC rotation speed in the case where the former model is applied. Specifically, at lower rotation speeds the ligand concentration is greater at larger distances into the aqueous phase resulting in a greater $[C]_{\max}$. However, several similarities also exist between Figures 6.2.1 and 6.2.2. Under both $[C]_i$ conditions, the $[C]_{\max}$ point is manifest closer to the interface at greater rotation speeds when the diffusion layer thickness X_D is smallest. Despite this, the value of $[C]_{\max}$ decreases

with increasing RDC rotation speed, which results in a decreased concentration gradient of complex directed towards the interface and a lower overall extraction flux.

6.3 Summary

For the TBP/Ce(IV) extraction system, which looks at simulating a PUREX extraction the fits using the model where $[C]_i$ is a constant produced the values of k'_f as 12 - 14 s^{-1} and k_b as 3 - 4 s^{-1} , whereas the fits using the model where $[C]_i$ is a distinct constant at each RDC rotation speed produced the value of k'_f as 5 - 6 s^{-1} and k_b as 1 - 2 s^{-1} . There is some discrepancy between the results, however the magnitude of estimated values is small and furthermore, in both cases, the forwards rate constant of complexation is approximately five times greater than the decomplexation rate. The relatively low values of kinetic rate constants indicate that TBP systems are controlled by both diffusive *and* kinetic forces, rather than by diffusion alone.

The next RDC study will be presented next which is concerned with TODGA extraction of Nd(III). More conclusions of the work from this section, alongside the others, will be presented in Section 8.

Chapter 7: RDC Extractions of Nd(III) by TODGA

This section presents an RDC study of the mass transfer and chemical kinetics of the i-SANEX process using neodymium(III) as a surrogate for the extracted trivalent actinides. The distribution coefficient of Nd(III) in 1.0 mol.dm⁻³ nitric acid systems is ~450 which is the same order of magnitude to the known distribution coefficient of ~600 for Am(III), the trivalent actinide in i-SANEX (Geist, et al., 2012; NEA, 2021). At 0.5 mol.dm⁻³ nitric acid, Cm(III) has a distribution coefficient of ~170 (Geist, et al., 2012; NEA, 2021), which, if extrapolated to systems at 1.0 mol.dm⁻³ nitric acid concentration, is expected to be very similar to that of Nd(III) and Am(III). As such, Nd(III) is a good surrogate metal ion for both trivalent minor actinides of interest; Am(III) and Cm(III).

However, Nd(III) also has the advantage of presenting four compound peaks in its UV-visible light absorbance spectrum that are well separated from the wavelength region where nitrate strongly absorbs, $\lambda < 350$ nm. All of these four peaks at approximately 524, 578, 740 and 795 nm are strongly absorbing in the aqueous and organic phase, allowing for accurate spectrophotometric quantification of metal ion solution concentrations in both. Before such studies may begin, calibration curves of absorbance vs. Nd(III) concentration must be obtained at the wavelength used and this is the subject of the next section.

7.1 Nd(III) Calibration Curves of UV-visible Light Absorbance with Organic and Aqueous Concentrations

Accordingly, mixer/centrifuge experiments of Nd(III) bearing nitric acid phases and TODGA bearing organic phases were conducted prior to RDC study of the Nd(III)-TODGA extraction. Varying the initial ligand and metal ion concentrations within the Thermomixer then provided data that could be used to construct a calibration curve allowing for the conversion of UV-visible light absorbance data for Nd(III) during RDC experiments into the more analytically useful unit of concentration.

Figure 7.1.1 shows the UV-visible light absorbance of dissolved neodymium(III) nitrate salt, at a range of concentrations, in 1.0 mol.dm⁻³ nitric acid, with the absorbance measured with respect to a blank spectrum of pure water.

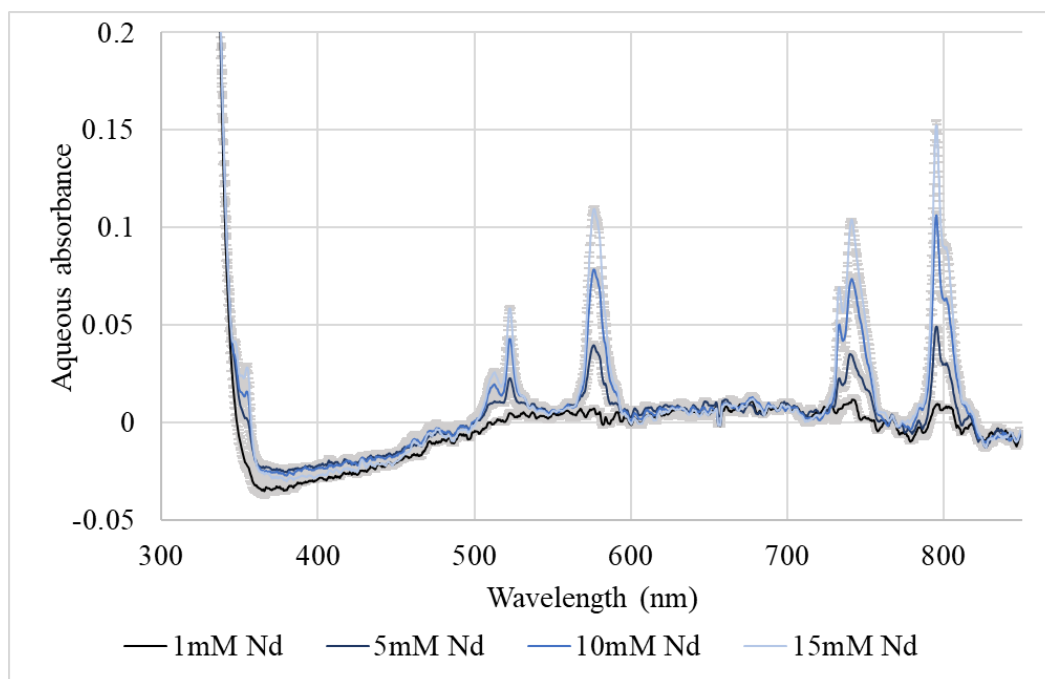


Figure 7.1.1: Aqueous UV-visible light absorbance spectra of Nd^{3+} dissolved in 1.0 mol.dm^{-3} nitric acid, measured with respect to a blank water reference. As-obtained spectra have been smoothed using a 7-point moving average and base corrected as described in the text. Error bars have been calculated based on the two readings taken per concentration. The use of unit mM is shorthand for mmol.dm^{-3} .

Key points to note from the spectra shown in Figure 7.1.1 include the following.

- A strong absorbance envelope is observed at wavelengths less than 350nm, known to be caused by nitrate ions.
- The spectra have been baseline corrected using the average absorbance measured in regions of the spectra in the vicinity of the peaks of interest but where no peaks are observed – specifically between 680-700 nm and 830-850 nm. This results in an anomalous negative absorbance in the range 350-490 nm. However, this negative absorbance is (i) well separated from the peaks of interest (ii) small at ~ -0.025 absorbance units, and (iii) not dependent on Nd(III) concentration. The latter two observations therefore suggest that this is simply an experimental artefact derived from a gently sloping baseline within the instrument and so will be treated as such.
- Each spectrum contains four compound absorbance peaks centred at wavelengths of approximately 524, 578, 740 and 795 m. The intensities of all four vary with Nd(III) concentration and, being compound features, do not possess the form of a simple

single symmetrical absorbance peak. However, each compound feature does possess a single peak that is more prominent than others in each feature and so may be used to provide a measurement of concentration.

Thus, Figure 7.1.1 was used to obtain a calibration curve of aqueous absorbance of Nd(III) as a function of concentration at the four peak maxima of 524, 578, 740 and 795 nm – shown in Figure 7.1.2. Using the absorbance maxima of these compound peaks is an appropriate methodology for UV-vis spectroscopy. Extinction coefficients specific to each wavelength, which are shown by the gradients of the lines of best fit to each calibration curve, are given in Table 7.1.1. Each fit has an R^2 value greater than 0.99, suggesting that the approach to baseline subtraction employed for the data of Figure 7.1.2 is sensible. Automatic linear trendlines in MS Excel were plotted in Figure 7.1.2 rather than chi-squared best fits as there is minimal variation in the magnitude of the error bars. Experimental error on the best fit lines were obtained by manually varying the gradients so that the best fit line goes through the upper and lower limits of the error bars. The range between these two gradients divided by two is the error shown in Table 7.1.1. The same approach was used in Tables 7.1.2 and 7.1.3.

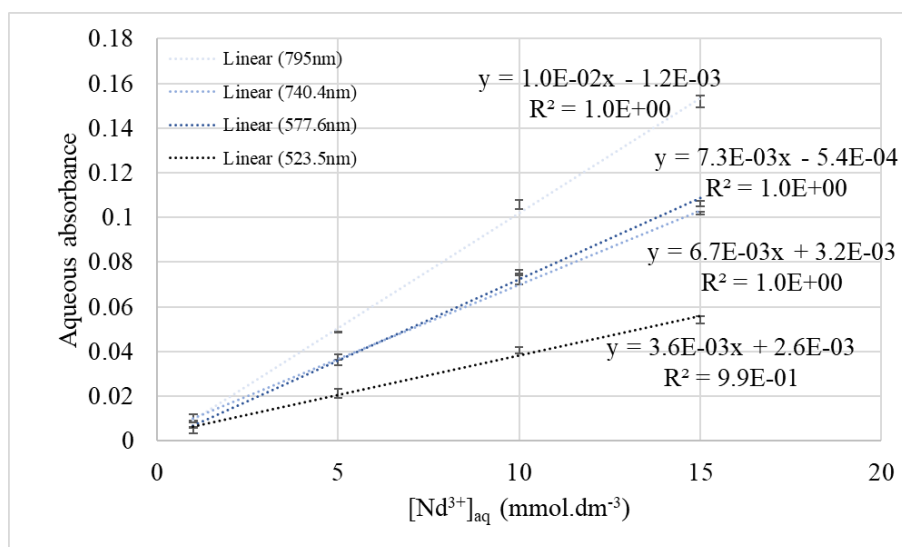


Figure 7.1.2: Aqueous neodymium(III) absorbance-concentration calibration curve for nitric acid concentration of 1.0 mol.dm^{-3} plotted in order to determine the UV-visible light absorbance extinction coefficients ($\epsilon_{\text{Nd, aq, } \lambda_{\text{max}}}$) at $\lambda_{\text{max}} = 524, 578, 740$ and 795 nm .

Table 7.1.1: UV-vis light absorbance extinction coefficients (ϵ) for aqueous Nd(III) ions at characteristic λ_{\max} peaks. Units defined per cm of path length l . Corresponding to Figure 7.1.2.

Aqueous absorbance peak λ_{\max} (nm)	$\epsilon_{\text{Nd,aq},\lambda_{\max}}$ ($\text{m}^3 \cdot \text{mol}^{-1} \cdot \text{cm}^{-1}$)
524	$3.6 \pm 0.2 \times 10^{-3}$
578	$7.3 \pm 0.3 \times 10^{-3}$
740	$6.7 \pm 0.2 \times 10^{-3}$
795	$1.0 \pm 0.03 \times 10^{-2}$

A second calibration curve of aqueous Nd(III) absorbance with concentration was obtained in $0.8 \text{ mol} \cdot \text{dm}^{-3}$ nitric acid, Figure 7.1.3. This was for a separate study not included in this thesis. However, it is included here as the Nd(III) concentration range studied, 0.1 - $20 \text{ mmol} \cdot \text{dm}^{-3}$, extends slightly beyond that shown in Figure 7.1.2, 1 - $15 \text{ mmol} \cdot \text{dm}^{-3}$. Extinction coefficients derived from the data of Figure 7.1.3 in the same manner as from Figure 7.1.2 are given in Table 7.1.2. It should be noted from these data that, at each wavelength studied, the extinction coefficients of Tables 7.1.1 and 7.1.2 are nearly identical – despite the differing nitric acid concentrations used and different Nd(III) concentration ranges studied – so cross-validating and giving confidence in both sets of results. Automatic linear trendlines in MS Excel were plotted in Figure 7.1.3 rather than the more robust chi-squared best fit line as the experimental error across all the data is similar.

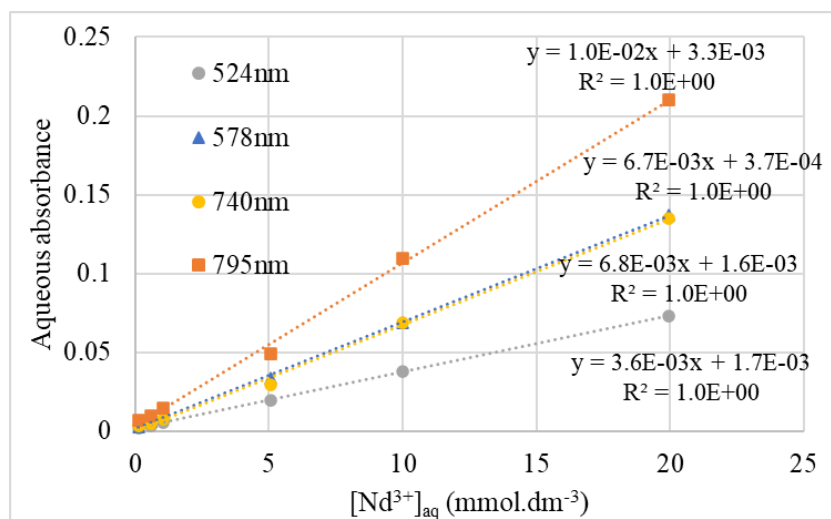


Figure 7.1.3: Aqueous neodymium(III) absorbance-concentration calibration curve for nitric acid concentration of 0.8 mol.dm^{-3} plotted for a study not presented, but included in order to validate the results shown in Figure 7.1.2.

Table 7.1.2: UV-vis light absorbance extinction coefficients (ϵ) for aqueous Nd(III) ions at characteristic λ_{max} peaks. Units defined per cm of path length l . Corresponding to Figure 7.1.3.

Aqueous absorbance peak λ_{max} (nm)	$\epsilon_{\text{Nd,aq},\lambda_{\text{max}}} (\text{m}^3 \cdot \text{mol}^{-1} \cdot \text{cm}^{-1})$
524	$3.6 \pm 0.2 \times 10^{-3}$
578	$6.7 \pm 0.2 \times 10^{-3}$
740	$6.8 \pm 0.3 \times 10^{-3}$
795	$1.0 \pm 0.03 \times 10^{-2}$

Four organic concentrations of TODGA, from 0.05 to 0.35 mol.dm^{-3} were contacted with an aqueous phase of 10 mmol.dm^{-3} Nd(III) in 1.0 mol.dm^{-3} nitric acid in the Thermomixer. Following this the samples were centrifuged prior to analysis to ensure full aqueous and organic phase separation. The organic spectra post-contact with the Nd(III)-loaded aqueous phase, shown in Figure 7.1.4, were calculated with respect to their corresponding blank organic phases (i.e. blank organic phases at different TODGA concentrations).

Key features of the spectra shown in Figure 7.1.4 include:

- A similar strong absorbance to the aqueous spectra (Figure 7.1.1) at wavelengths less than 350 nm. This is also due to the presence of nitrate ions which are co-extracted with Nd(III) by TODGA before being subsumed into the organic phase.
- Five compound peaks centred at wavelengths of approximately 350, 535, 584, 739 and 803 nm which vary with Nd(III) concentration. As was observed in the aqueous spectra, each peak feature possesses a single peak of prominence that may be used to calculate concentration. However, due to the lower magnitude absorbance peak maxima in the 350 and 535 nm collections of peaks, they are not used in further analysis.
- Another baseline shift in the negative direction at 350-500 nm is visible in the organic spectra, however it is less pronounced in Figure 7.1.4 compared to Figure 7.1.1. The same explanation as was described for the aqueous Nd(III) spectra stands regarding this spectral feature.

The 0.2 mol.dm^{-3} and 0.35 mol.dm^{-3} TODGA organic phase post-contact spectra, shown in Figure 7.1.4, are the same. Thus, at these two organic TODGA concentrations, same extent of extraction of Nd(III) occurs, indicating that at TODGA concentrations beyond 0.2 mol.dm^{-3} , there is no increase in the extent of extraction.

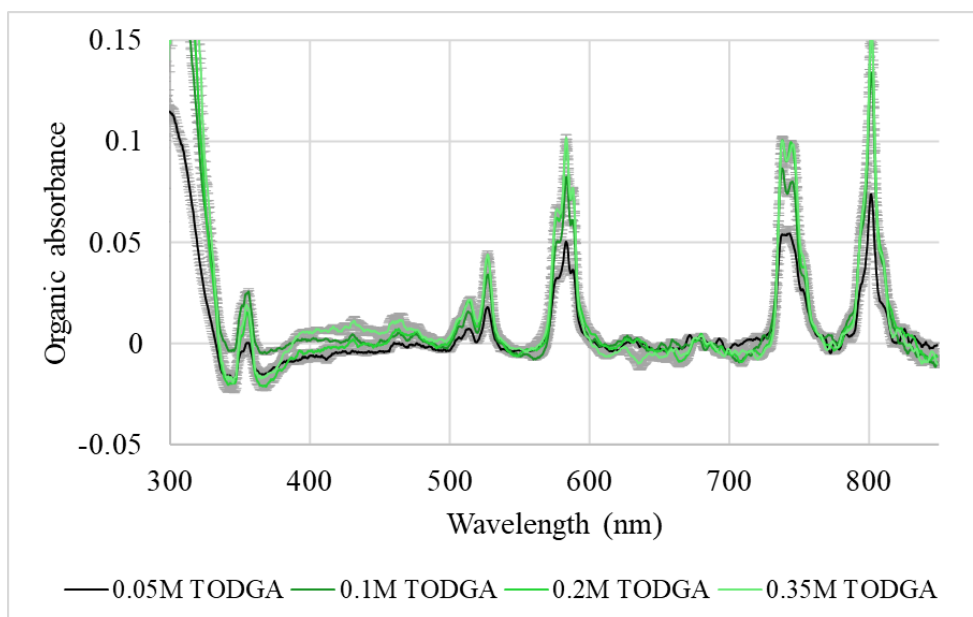


Figure 7.1.4: Organic UV-visible light absorbance spectra of Nd(III) extracted from an initial load of 10 mmol.dm^{-3} of Nd(III) in 1.0 mol.dm^{-3} nitric acid into varying concentrations of TODGA in n-dodecane (5% octanol). Absorbances calculated with respect to a blank organic phase. Spectra smoothed using a 9-point moving average and base corrected using the average absorbance between 600-700 nm. Error bars calculated based on the two readings taken per concentration. The use of unit M is shorthand for mol.dm^{-3} .

The concentration of organic Nd(III) which corresponds to each absorbance spectrum shown in Figure 7.1.4 has been calculated from the subtraction of the Nd(III) concentration in the aqueous phase, resulting from the contacting process, from the initial aqueous Nd(III) load of 10 mmol.dm^{-3} . The spectra of the aqueous phases produced after the contacting process, calculated with respect to a pure water blank phase, are shown by Figure 7.1.5; the aqueous pre-contacted aqueous phase is also shown for comparison. Aqueous concentrations of Nd(III) from these data could be obtained using *any* of the aqueous Nd(III) extinction coefficients shown in Table 7.1.1, however the extinction absorbance peak at 740nm was ultimately chosen out of convenience.

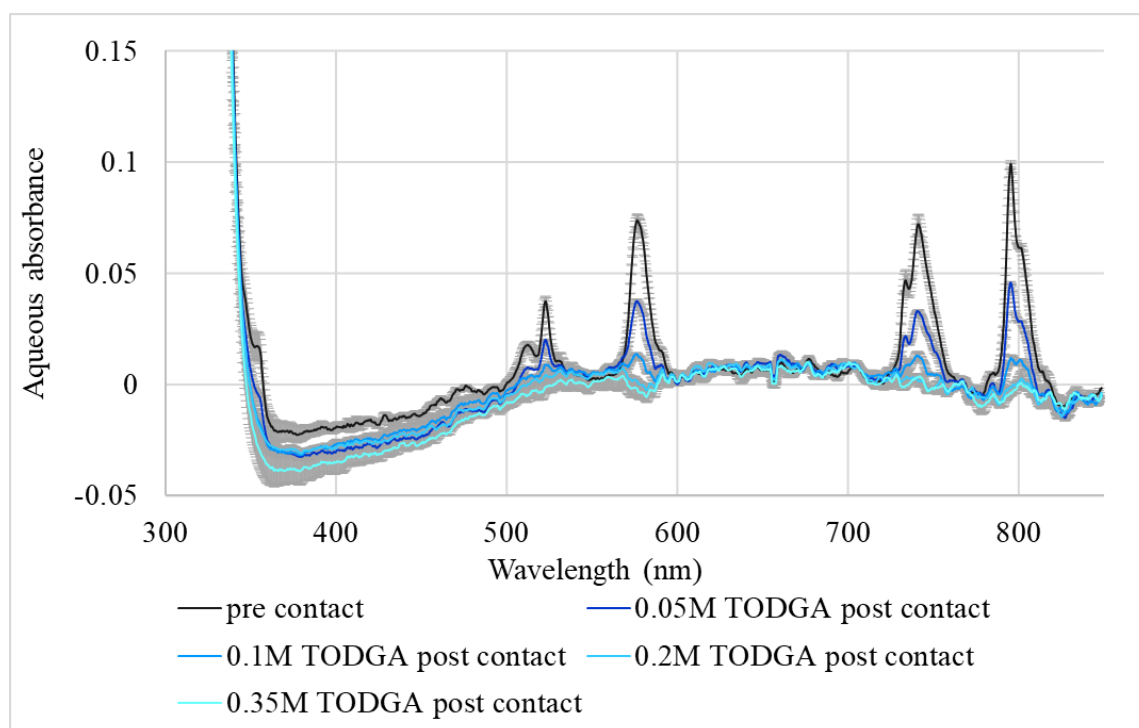


Figure 7.1.5: Aqueous UV-visible light absorbance spectra of Nd(III) following mixer-centrifuge with varying organic TODGA concentrations in n-dodecane, 5% octanol. Initial aqueous metal ion load is $10 \text{ mmol}\cdot\text{dm}^{-3}$ of Nd(III) in $1.0 \text{ mol}\cdot\text{dm}^{-3}$ nitric acid. Absorbances measured with respect to a blank spectrum of water. Spectra smoothed using a 9-point moving average and base corrected using the average absorbance between 600-700 nm and 820-850 nm. Error bars calculated based on the two readings taken per concentration. The use of unit M is shorthand for $\text{mol}\cdot\text{dm}^{-3}$.

The decrease in Nd(III) concentration in the aqueous phase corresponds to the organic Nd(III) concentration resulting in the absorbance spectra shown in Figure 7.1.4. A calibration curve at the three organic wavelengths, 584, 739 and 803 nm, is shown by Figure 7.1.6. Table 7.1.3 shows the extinction coefficients for organic neodymium(III) which are the gradients of the lines of best fit plotted in Figure 7.1.6. Automatic linear trendlines in MS Excel were plotted in Figure 7.1.6 rather than chi-squared best fits as the experimental error across all these data is similar.

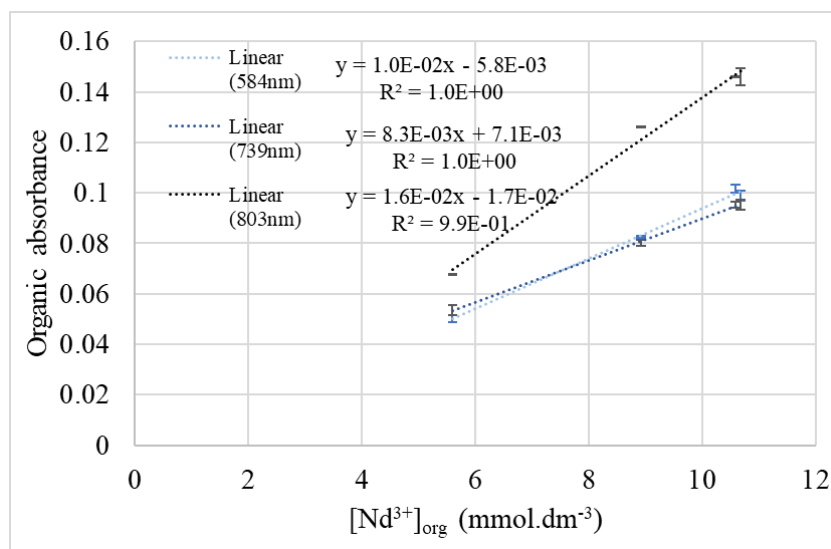


Figure 7.1.6: Organic Nd(III) absorbance-concentration calibration curve for nitric acid concentration of 1.0 mol.dm^{-3} plotted in order to determine the UV-visible light absorbance extinction coefficients ($\epsilon_{\text{Nd,org},\lambda_{\text{max}}}$) at $\lambda_{\text{max}} = 584, 739$ and 803 nm .

Table 7.1.3: UV-vis light absorbance extinction coefficients (ϵ) for organic Nd(III) ions at characteristic λ_{max} peaks. Units defined per cm of path length l .

Organic absorbance peak λ_{max} (nm)	$\epsilon_{\text{Nd,org},\lambda_{\text{max}}} (\text{m}^3.\text{mol}^{-1}.\text{cm}^{-1})$
584	$1.0 \pm 0.06 \times 10^{-2}$
739	$8.3 \pm 0.2 \times 10^{-3}$
803	$1.6 \pm 0.04 \times 10^{-2}$

The extinction coefficient information produced in this section is sufficient to analyse the RDC data which are of principal interest in this study. However, before this is attempted, one final analysis shall be presented: the determination of complexation stoichiometry. This is covered in the next section.

7.2 Stoichiometry of TODGA/Nd(III) Complex at Equilibrium

This section presents the calculation of the reaction stoichiometry of TODGA with respect to Nd(III) in the complexation process which is key to the overall extraction. For actinide and lanthanide ions, the TODGA/metal ion complex is known to exist in a 2:1, 3:1 and (sparingly) 4:1 ratio of TODGA molecules per metal ion (Whittaker, et al., 2018). The data analysis presented in this section identifies the complexation stoichiometry in the case where

Nd(III) is the target metal ion. As mentioned in Section 5.2, reaction stoichiometry is of interest not from a chemical kinetic point of view, as we have already assumed that the formation of the initial 1:1 ligand/metal ion complex is the rate determining step. Instead, the reaction stoichiometry, and the ligand/metal ion ratio of the fully formed complex is of interest for the overall mass balance.

Figure 7.2.1 shows the initial TODGA concentrations employed in the contactor experiments shown in Section 7.1, Figure 7.1.4, plotted against the distribution coefficient $D_{\text{dist,Nd(III)}}$ calculated in each case.

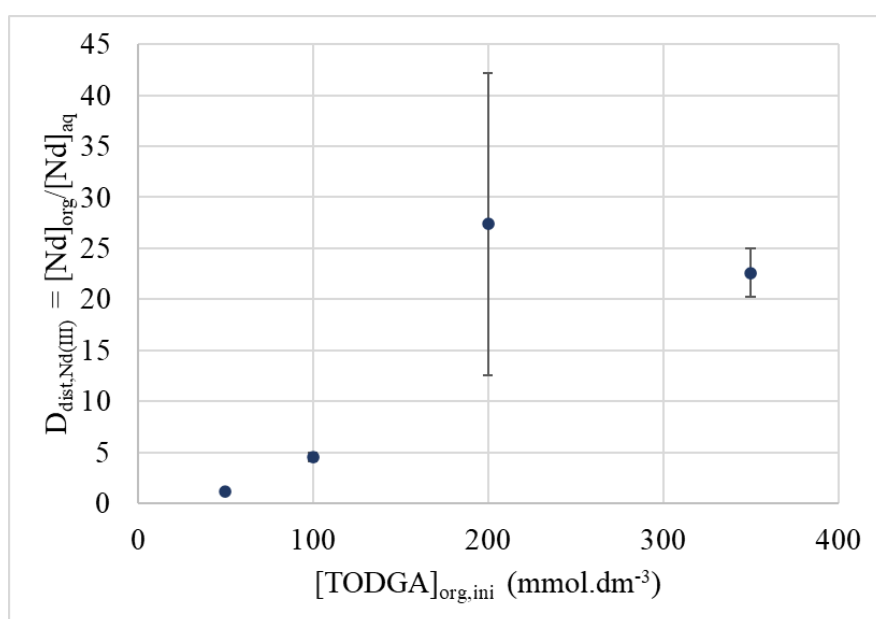


Figure 7.2.1: Distribution coefficient of Nd(III) in a TODGA/Nd(III) system as a function of initial TODGA concentration in the organic phase. Initial load of aqueous Nd(III) is 10 mmol.dm^{-3} .

$D_{\text{dist,Nd(III)}}$ is calculated from the quotient of the concentration of Nd(III) found to have been extracted into the organic phase over the concentration of Nd(III) remaining in the aqueous phase following the contacting process. For initial TODGA concentrations of $0.2\text{-}0.35 \text{ mol.dm}^{-3}$, the extent of extraction is approximately the same, and is at a maximum, which is why these data in Figure 7.2.1 have the two highest distribution coefficients. The error bars for the 0.2 mol.dm^{-3} initial TODGA concentration datum are very large (± 15) because the value of its denominator, $[\text{Nd}]_{\text{aq}}$, is found to be almost as small as its associated error. Consequently, the percentage error becomes very large for the distribution coefficient denominator and creates a large error in the final value of $D_{\text{dist,Nd(III)}}$ shown in Figure 7.2.1.

The nominal value of the maximum achievable distribution coefficient for a TODGA/Nd(III) extraction system is between 15 to 40, according to the analysis shown in Figure 7.2.1. This is around an order of magnitude less than the anticipated distribution coefficient of ~ 450 (Geist, et al., 2012; NEA, 2021). Due to time constraints, this discrepancy was not fully investigated during these studies. However, rather than rely on external studies conducted using different apparatus, detection methods and analytical processes, the D-value results *here* shown by Figure 7.2.1 are taken forwards.

Equation 7.2.1 exhibits the general form of the complexation reaction and its corresponding equilibrium equation is shown by Equation 7.2.2, where $K_{\text{Nd(III)},\text{eq}}^{\text{TODGA}}$ is the equilibrium constant.



$$K_{\text{Nd(III)},\text{eq}}^{\text{TODGA}} = \frac{[\text{Nd}^{3+}\text{TODGA}_\gamma(\text{NO}_3^-)_q]_{\text{org}}}{[\text{Nd}^{3+}]_{\text{aq}} [\text{NO}_3^-]_{\text{aq}}^q [\text{TODGA}]_{\text{org}}^\gamma} \quad (7.2.2)$$

Equation 7.2.2 is simplified by the substitution of the equation for $D_{\text{dist,Nd(III)}}$, shown by Equation 7.2.3. A rearranged form of the equilibrium equation following this substitution is shown by Equation 7.2.4.

$$D_{\text{dist,Nd(III)}} = \frac{[\text{Nd}^{3+}\text{TODGA}_\gamma(\text{NO}_3^-)_q]_{\text{org}}}{[\text{Nd}^{3+}]_{\text{aq}}} \quad (7.2.3)$$

$$D_{\text{dist,Nd(III)}} = K_{\text{Nd(III)},\text{eq}}^{\text{TODGA}} [\text{NO}_3^-]_{\text{aq}}^q [\text{TODGA}]_{\text{org}}^\gamma \quad (7.2.4)$$

Equation 7.2.5 is the product of taking the \log_{10} of Equation 7.2.4 and is plotted in Figure 7.2.2.

$$\log(D_{\text{dist,Nd(III)}}) = \log\left(K_{\text{Nd(III)},\text{eq}}^{\text{TODGA}}\right) + \gamma \log[\text{TODGA}]_{\text{org}} + q \log[\text{NO}_3^-]_{\text{aq}} \quad (7.2.5)$$

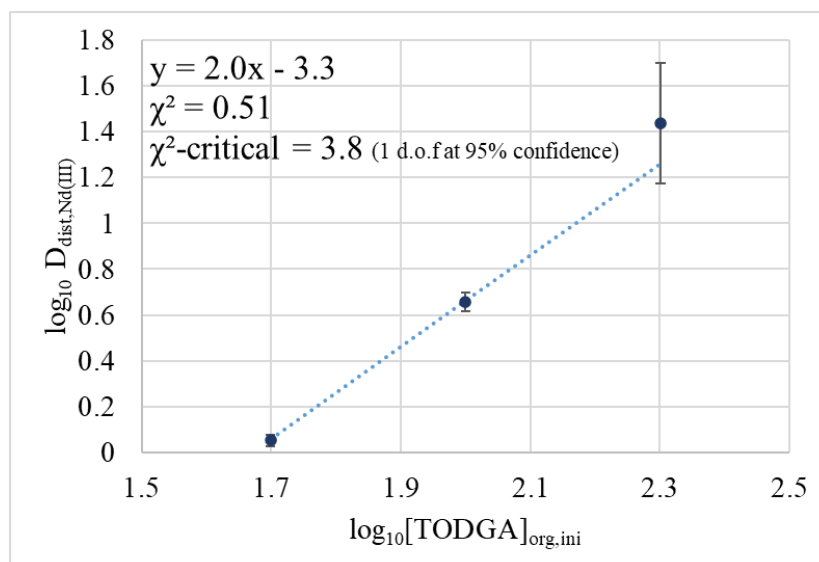


Figure 7.2.2: Log/log plot of Figure 7.2.1 which shows Nd(III) distribution coefficient as a function of initial organic TODGA concentration.

The gradient of the line of best fit in the log/log plot shown by Figure 7.2.2 corresponds to the stoichiometry constant γ , which is 2.0. This indicates that the stoichiometry of TODGA with respect to Nd(III) is on average 2.0. The best fit line in Figure 7.2.2 is not a standard MS Excel linear fit but a chi-squared best fit line due to the varying experimental error across the data.

7.3 RDC Experimental Results for Nd(III)/TODGA

An aqueous phase of $10\text{mmol}\cdot\text{dm}^{-3}$ Nd(III) in $1.0\text{mol}\cdot\text{dm}^{-3}$ nitric acid and an organic phase of $0.2\text{mol}\cdot\text{dm}^{-3}$ TODGA and 5% octanol (by volume) in n-dodecane was employed in each RDC run; the Nd(III)-containing aqueous phase situated in the stationary outer beaker and the extracting TODGA-containing organic phase situated in the rotating inner cylinder. Figures 7.3.1 to 7.3.5 show typical UV-visible light absorbance spectra over time for the organic phases contained within the RDC for each experiment conducted at a different inner cylinder rotation speed; 1, 2.5, 5, 7.5 and 10 Hz. Each absorbance spectrum is calculated with respect to a blank organic phase. As each RDC experiment progresses, shown by the time increments in the legends of Figures 7.3.1 to 7.3.5, Nd(III) peaks similar to that observed in Figure 7.1.4 emerge.

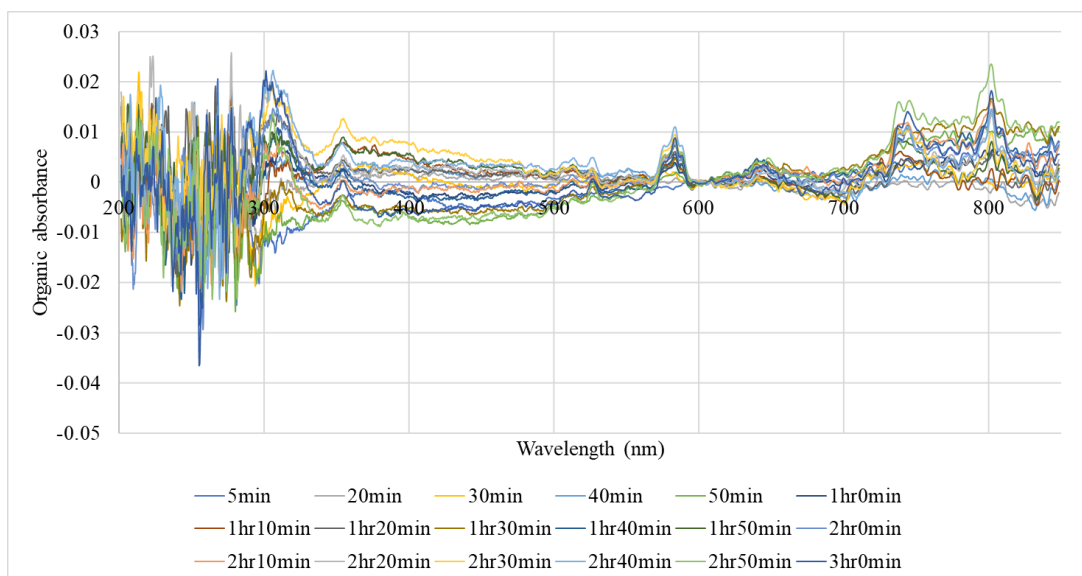


Figure 7.3.1: RDC spectra of Nd(III) extraction by TODGA/n-dodecane, with 5% octanol, for a rotation speed of 1 Hz. Base corrected calculated with respect to a wavelength region of 600-610 nm. Curve-smoothing via 9-point moving average.

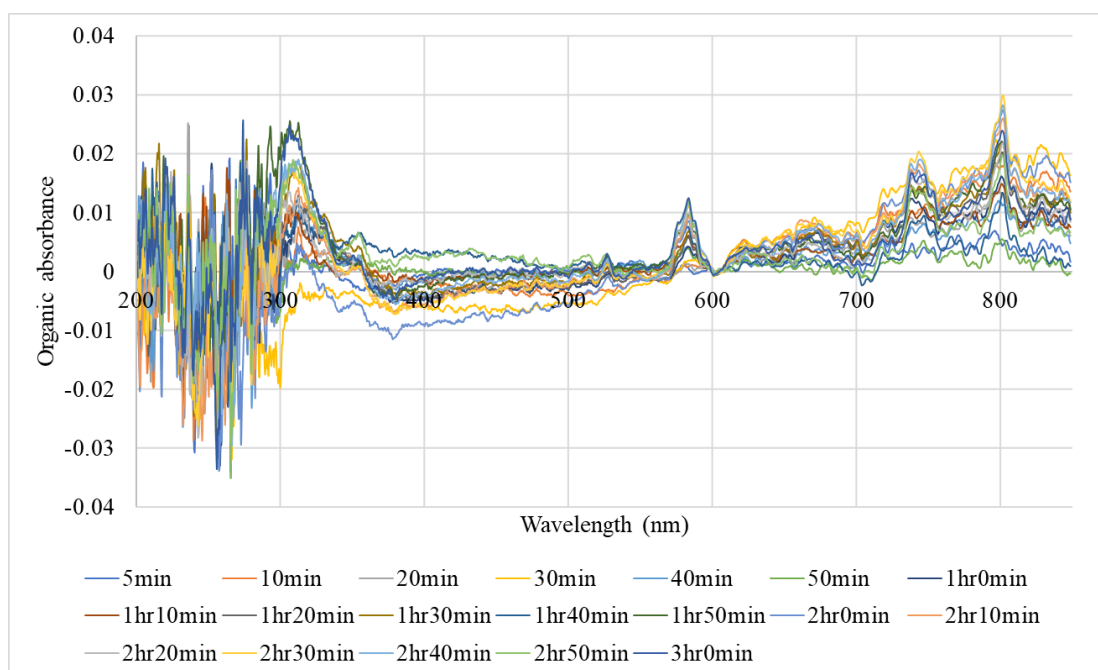


Figure 7.3.2: RDC spectra of Nd(III) extraction by TODGA/n-dodecane, with 5% octanol, for a rotation speed of 2.5 Hz. Base corrected calculated with respect to a wavelength region of 600-610 nm. Curve-smoothing via 9-point moving average.

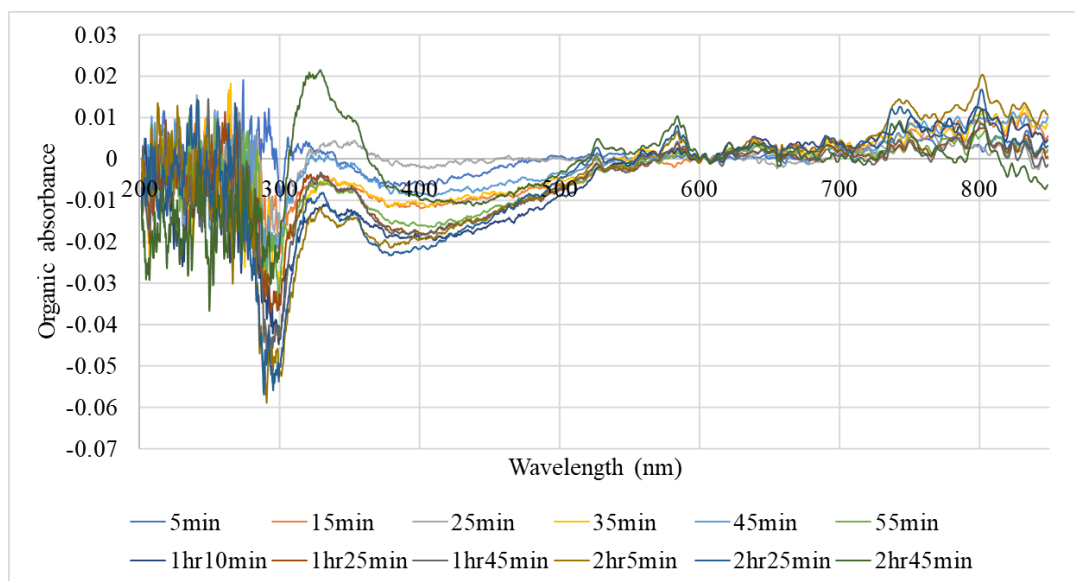


Figure 7.3.3: RDC spectra of Nd(III) extraction by TODGA/n-dodecane, with 5% octanol, for a rotation speed of 5 Hz. Base corrected calculated with respect to a wavelength region of 600-610 nm. Curve-smoothing via 9-point moving average.

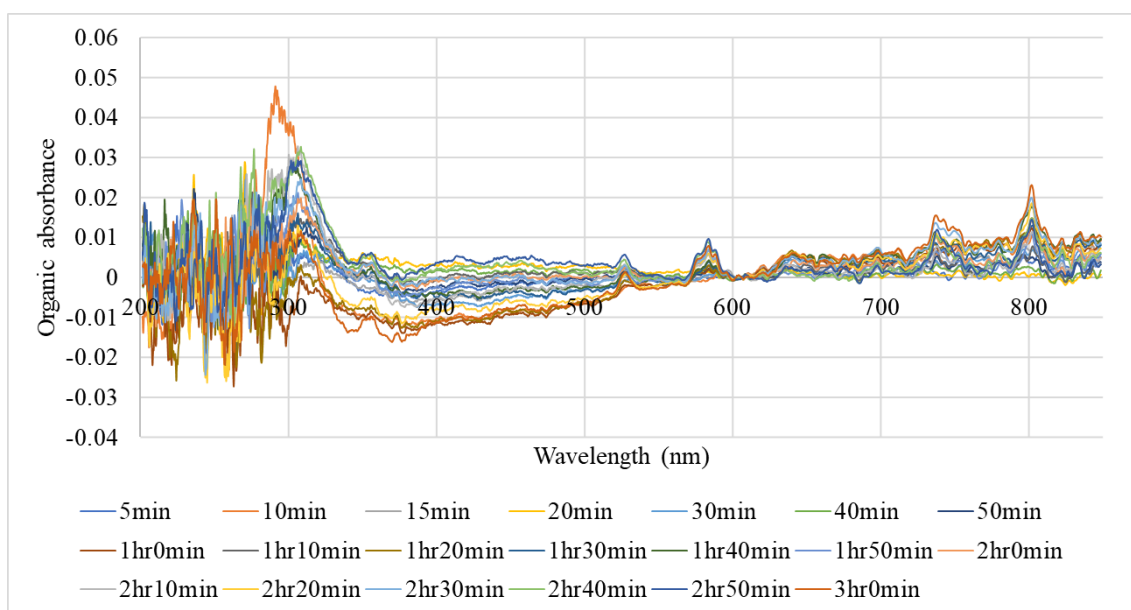


Figure 7.3.4: RDC spectra of Nd(III) extraction by TODGA/n-dodecane, with 5% octanol, for a rotation speed of 7.5 Hz. Base corrected calculated with respect to a wavelength region of 600-610 nm. Curve-smoothing via 9-point moving average.

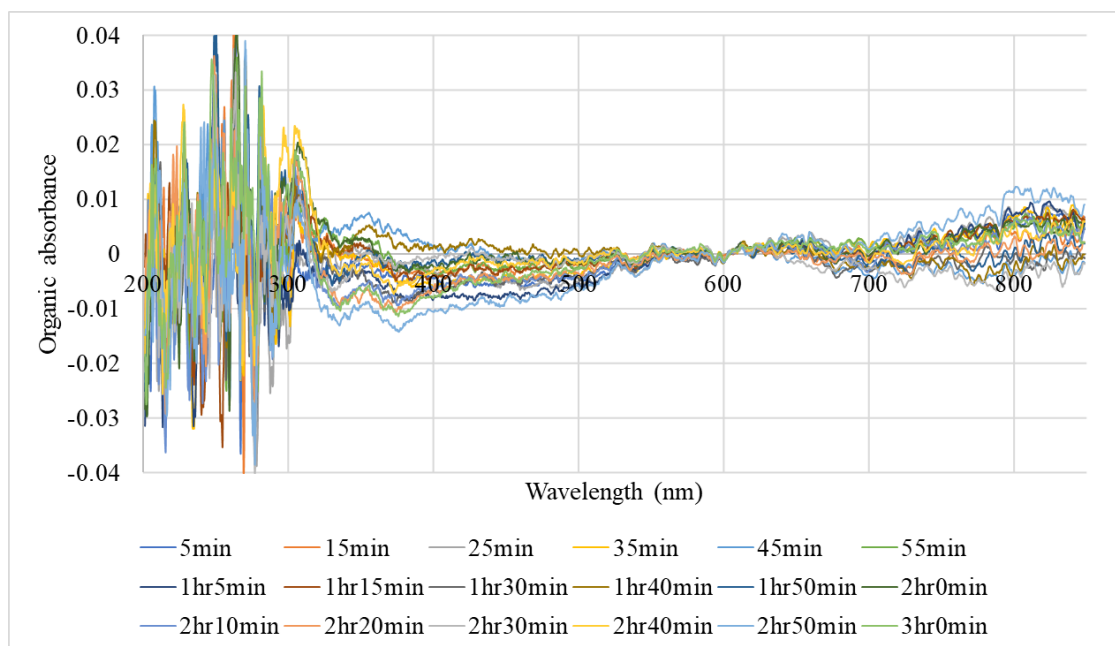


Figure 7.3.5: RDC spectra of Nd(III) extraction by TODGA/n-dodecane, with 5% octanol, for a rotation speed of 10 Hz. Base corrected calculated with respect to a wavelength region of 600-610 nm. Curve-smoothing via 9-point moving average.

The key features of the spectra shown in Figures 7.3.1 to 7.3.5 include:

- the characteristic organic Nd(III) ion absorbance behaviour whereby a collection of peaks emerge in the wavelength regions centred on 584, 739 and 803 nm.
- a distinct negative absorbance behaviour similar to what was observed for Figures 7.1.1 and 7.1.4 at 300-350 nm;
- large amounts of baseline noise attributable to the low concentrations of Nd(III), i.e. the signal to noise ratio is much larger for these data than for the TBP/Ce(IV) data analysed previously in this thesis;
- inconsistent nitrate extraction between runs – Figure 7.3.4 for example has a distinct peak in the nitrate absorbing region of ~300 nm, whereas Figure 7.3.3 in the same wavelength region has an absorbance dip.

The wavelength selected for the determination of the Nd(III) concentration is 584 nm. Thus, the absorbance at this wavelength was corrected with respect to the baseline shift at wavelengths 560 and 600 nm; wavelengths either side of the absorbance region of interest which register a zero absorbance for Nd(III). The absorbance at 584 nm was divided by the relevant extinction coefficient from Table 7.1.3 and the path length of the UV-visible light

measurement cell of 1.0 cm to obtain the concentration of Nd(III) at each time point. These data are shown by Figure 7.3.6. Best fit lines were obtained using the chi-squared theory outlined in Section 3.4.4.

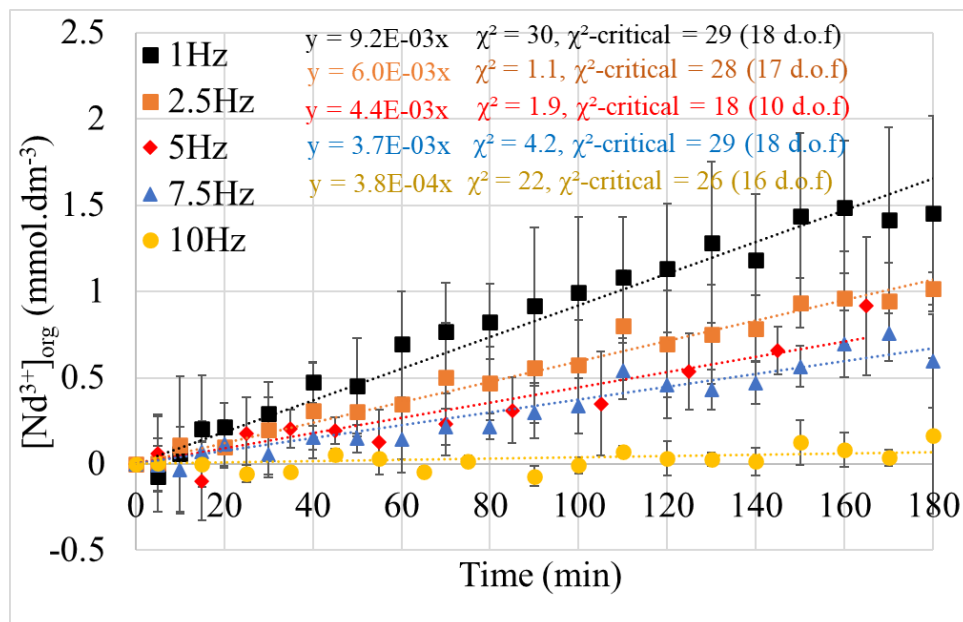


Figure 7.3.6: Concentration of organic Nd(III) as a function of experimental time period for the RDC at several rotation speeds. Organic phase consists of 0.2 mol.dm^{-3} TODGA in *n*-dodecane and aqueous phase initially consists of 10 mmol.dm^{-3} Nd(III) in 1.0 mol.dm^{-3} nitric acid. λ_{max} used is 584 nm. Base correction calculated with respect to the wavelengths at 560 and 600 nm.

As was observed with the TBP/Ce(IV) data from Section 6, Figure 7.3.6 exhibits a constant extraction rate of Nd(III) throughout the experimental time period, with no observable plateauing, indicating that the equilibrium concentration of organic Nd(III), determined by the distribution coefficient, has not been reached. The observed concentration of Nd(III) in the organic phase at the end of the RDC run at 1 Hz in Figure 7.3.6 is approximately 1.5 mmol.dm^{-3} , which equates to approximately 7% of the available molar stock of Nd(III) in the aqueous phase. This further indicates that equilibrium has not been reached at the end of the time period over which extraction was conducted.

The lines of best fit shown in Figure 7.3.6 have been used to calculate the Nd(III) extraction flux, j , taking into account the volume of the organic phase of 35 cm^3 and the interfacial area of the circular interfacial membrane, which has a diameter of 2.0 cm. Figure 7.3.7 shows the

flux plotted with respect to inverse square root of RDC rotation speed. The error bars reflect the extent to which each of gradients of the lines of best fit in Figure 7.3.6 may reasonably vary within the error bars accompanying the data. This process is shown by Figure 7.3.8.

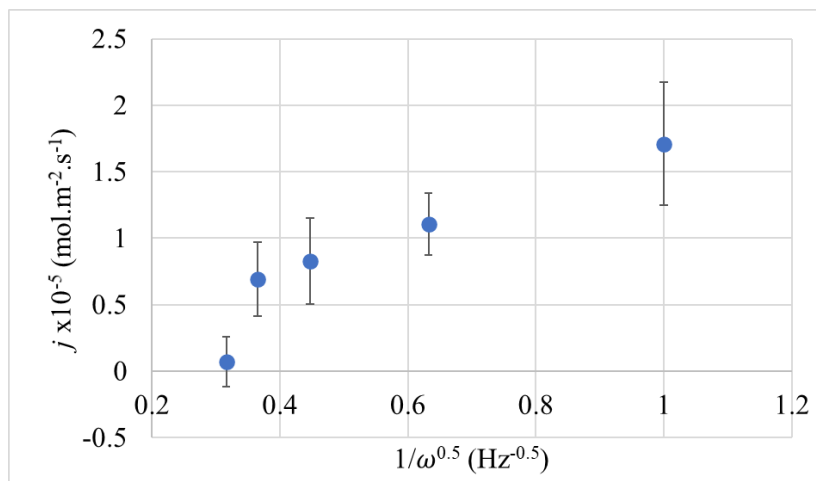


Figure 7.3.7: RDC extraction flux, j as a function of RDC inverse square root of rotation speed, $\omega^{-0.5}$. Extraction of Nd(III) into the organic phase of 0.2 mol.dm^{-3} TODGA in n-dodecane and 5% octanol from an initial aqueous phase of 10 mmol.dm^{-3} Nd(III) in 1.0 mol.dm^{-3} nitric acid.

The inverse proportionality of j with respect to inverse square root of rotation speed shown in Figure 7.3.7 is concordant with the previous TBP/Ce(IV) RDC study presented in Section 6. However, there is less of a tendency towards plateauing at the lower rotation speeds, i.e. at greater values of $\omega^{-0.5}$.

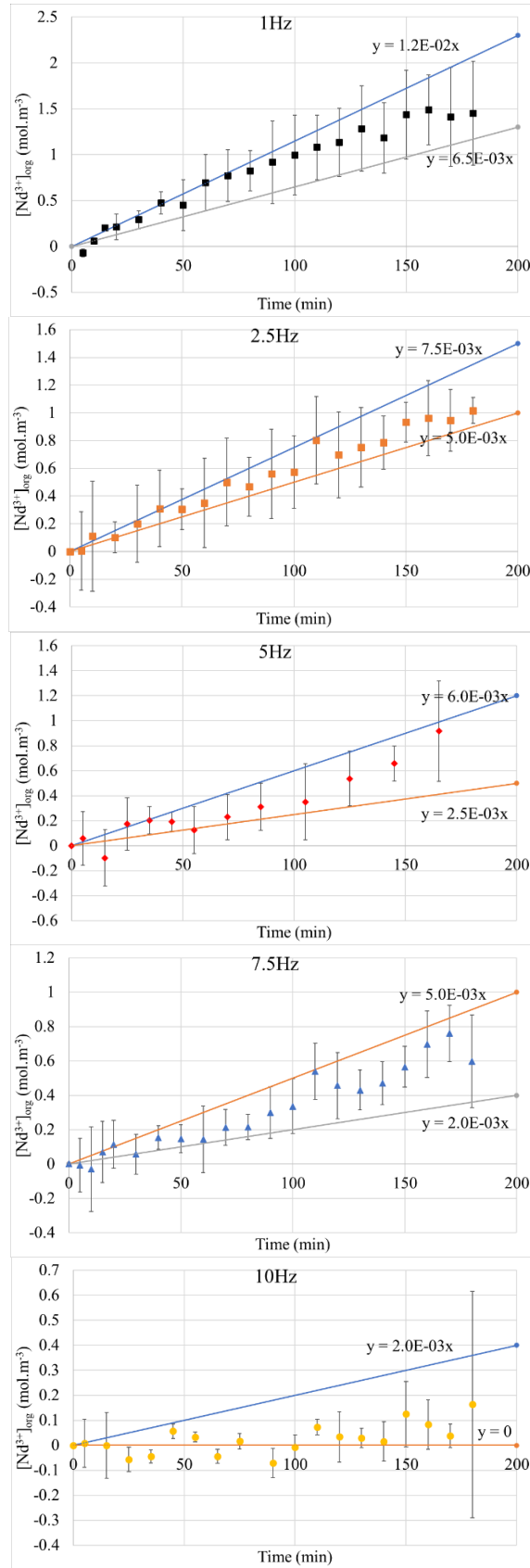


Figure 7.3.8: Plots of Nd(III) concentration with time at different rotation speeds. The slopes of the regression lines plotted over the experimental data divided by two equate to the experimental error of the extraction flux in Figure 7.3.7.

The average extraction flux encountered in Figure 7.3.7, which is $\sim 1 \times 10^{-5} \text{ mol.m}^{-2}.\text{s}^{-1}$ across all rotation speeds, is the same as that found in the TBP/Ce(IV) system, shown in Figure 4.3.2. The initial solution concentrations of ligand and metal ion, the area of the interfacial membrane, and RDC solution volumes are the same in both the Ce(IV) and Nd(III) systems, which could be the reason for their similar extraction performance. However, TBP and TODGA possess very different aqueous solubilities; $1.46 \text{ mmol.dm}^{-3}$ for TBP (Velavendan, et al., 2013) and $0.042 \text{ mmol.dm}^{-3}$ for TODGA (Sasaki, Sugo, Suzuki, & Tachimori, 2001). Therefore, the TODGA system would be expected to have a much faster kinetic rate of complexation compared to the TBP system to make up for the fact that there will be an aqueous TODGA concentration at the interface two orders of magnitude lower.

7.4 Unknown Kinetic Constants Estimation Using Semi-analytical gPROMS Model

As with the TBP/Ce(IV) system, there are a number of unknown constants which are either known or must be estimated for the model to be fully defined.

Values of the known constants were sourced or estimated as follows:

- $[L]_i$, which is the TODGA ligand solubility of $0.042 \text{ mmol.dm}^{-3}$ in nitric acid (Sasaki, Sugo, Suzuki, & Tachimori, 2001).
- $[L]_D$ and $[C]_D$, which are the concentrations of species at the edge of ligand and complex diffusion layers which are zero given the large volume of the bulk aqueous phase and the well-mixed nature of the convection layer.
- The ligand stoichiometry γ is 2.0; the result of the equilibrium stoichiometry study shown in Section 7.2.
- The diffusion coefficient in the organic phase for the TODGA/metal/nitrate ion complex was sourced for Eu(III) and Am(III) in a study by Simonin *et al.* For organic Eu(III), D_C is $1.1 - 1.8 \times 10^{-10} \text{ m}^2.\text{s}^{-1}$ and for organic Am(III), D_C is $1.2 - 1.9 \times 10^{-10} \text{ m}^2.\text{s}^{-1}$. These data were obtained using the RMC and capillary methods (Simonin, Boxall, & Lélías, 2019). Singh *et al* interrogates the organic diffusion coefficient of Cd(II)/ligand/nitrate ion complexes in both TBP-dodecane and TODGA-dodecane organic phases and reports D_C to be $3.7 \times 10^{-11} \text{ m}^2.\text{s}^{-1}$ and $5.8 \times 10^{-10} \text{ m}^2.\text{s}^{-1}$, respectively (Singh, Mukhtyar, Bootwala, & Gaikar, 2017). Thus, TBP/Cd(II) complexes according to the Singh *et al* study are less diffusive than the

TBP/Ce(IV) complexes from the Bromley *et al* studies presented in Sections 4 and 6. However, Singh *et al* employed dodecane as the solvent and used a TBP concentration of 1.0 mol.dm^{-3} , whereas Bromley *et al* used OK as the solvent and had an 80% lower concentration of TBP of 0.2 mol.dm^{-3} . The differing concentrations of organics, especially of the ligand, which has complexing effects, drastically alters the ease with which metal ions diffuse through the organic liquid phase. Thus, the fact that a greater concentration of complexing TBP is manifest in the Singh *et al* TBP system means that it is not comparable to the system studied by Bromley *et al*, shown in Sections 4 and 6. Diffusion coefficients in studies on systems possessing the same key concentrations as the RDC studies undertaken in this thesis are the best approximation for use in these estimations of the unknown constants. The studies by Simonin *et al* employ organic phases with identical solution concentrations to the studies shown here; 0.2 mol.dm^{-3} TODGA in n-dodecane with 5% octanol by volume. The only difference is the use of TPH (total petroleum hydrocarbons) in place of n-dodecane, however they possess very similar physical properties, thus the effects on diffusivity of species and extraction is minimal. Therefore, for this thesis, the diffusion coefficient for the TODGA/Nd(III)/nitrate complex in the organic phase, D_C can be approximated as $1.5 \times 10^{-10} \text{ m}^2 \cdot \text{s}^{-1}$ as the average of the diffusivities from the most relevant literature (Simonin, Boxall, & L  lias, 2019).

- The organic diffusion coefficient D_L is assumed to be double that of the organic TODGA/Nd(III)/nitrate complex, $3.0 \times 10^{-10} \text{ m}^2 \cdot \text{s}^{-1}$, due to the lack of studies available which determine the self-diffusion coefficient for organic TODGA.

As with the TBP/Ce(IV) system, the above unknown constants reflect the species as they travel through the *organic* phase, and the RDC model requires diffusive information pertaining to the *aqueous* phase. Thus, scaling the diffusion coefficients using the Stokes-Einstein equation is also applied here. Observing the viscosity and density information shown in Table 7.4.1, the dynamic viscosity of the aqueous phase, assumed to be equal to that of water, is 35% smaller than the dynamic viscosity of n-dodecane. Thus, the aqueous diffusivities should be 35% greater, resulting in: $D_C = 2.0 \times 10^{-10} \text{ m}^2 \cdot \text{s}^{-1}$ and $D_L = 4.1 \times 10^{-10} \text{ m}^2 \cdot \text{s}^{-1}$.

Table 7.4.1: Table containing viscosity and density information for n-dodecane and water.

Solvent	Kinematic viscosity ($\text{m}^2 \cdot \text{s}^{-1}$)	Density at 25°C ($\text{kg} \cdot \text{m}^{-3}$)	Dynamic viscosity at 25°C (Pa.s)	Reference
n-dodecane	1.8×10^{-6}	746	1.4×10^{-3}	(NIST, 2021)
Water	8.9×10^{-7}	997	8.9×10^{-4}	(NIST, 2021)

7.4.1 Estimating Unknown Constants Where $[C]_i$ is a Constant Across All RDC Rotation Speeds

k'_f , k_b and $[C]_i$ estimations are shown by Figure 7.4.1.1 and Tables 7.4.1.1 and 7.4.1.2. Table 7.4.1.1 includes the estimations of the unknown constants when D_L and D_C are set to the literature values of their diffusivities in the organic phase and Table 7.4.1.2 includes the estimations of unknown constants when D_L and D_C are set to Stokes-Einstein-derived aqueous diffusivities.

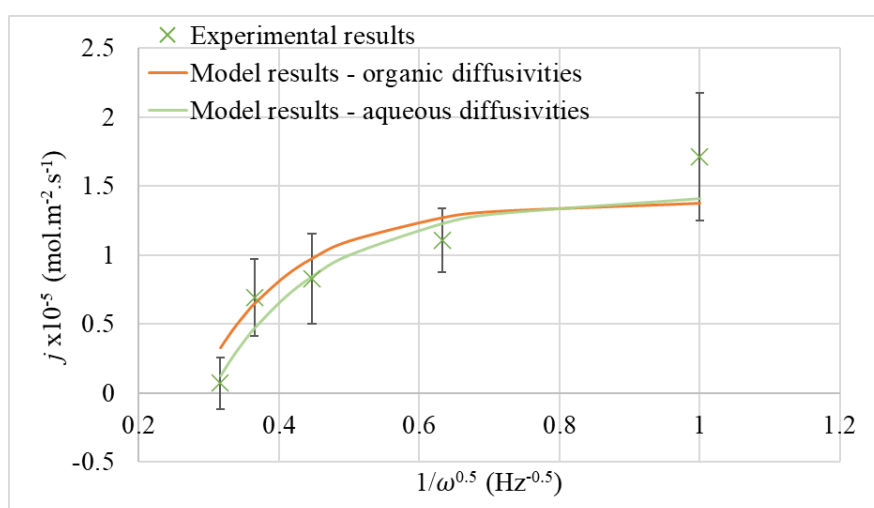


Figure 7.4.1.1: RDC experimental extraction flux as a function of RDC inverse square root of rotation speed, $\omega^{-0.5}$. j of Nd(III) into the organic phase of $0.2 \text{ mol} \cdot \text{dm}^{-3}$ TODGA in n-dodecane with 5% octanol from an initial aqueous phase of $10 \text{ mmol} \cdot \text{dm}^{-3}$ Nd(III) in $1.0 \text{ mol} \cdot \text{dm}^{-3}$ nitric acid. Organic diffusivities are obtained directly from the literature and aqueous diffusivities are derived via the Stokes-Einstein relation. Best fit using the model where $[C]_i$ is a constant in gPROMS.

Table 7.4.1.1: Constants associated with the optimum model fit of the TODGA/Nd(III) system shown by the organic diffusivities model results shown in Figure 7.4.1.1. The χ^2 value being smaller than the χ^2 -critical value indicates a good model fit.

	D_L ($m^2 \cdot s^{-1}$)	D_C ($m^2 \cdot s^{-1}$)	γ	k'_f (s^{-1})	k_b (s^{-1})	$[C]_i$ ($mmol \cdot dm^{-3}$)
Value	3.0×10^{-10}	1.5×10^{-10}	2.0	10000	1.5	2.5
Standard Deviation	-	-	-	89000	8.1	8.6
90% confidence interval	-	-	-	260000	24	25
95% confidence interval	-	-	-	380000	35	37
99% confidence interval	-	-	-	880000	81	86
95% t-value	-	-	-	0.027	0.042	0.068
Reference t-value (95%)	2.9					
χ^2	0.74					
χ^2 -critical	6.0 (5 data - 3 fitting parameters = 2 d.o.f.)					

Table 7.4.1.2: Constants associated with the optimum model fit of the TODGA/Nd(III) system shown by the aqueous diffusivities model results shown in Figure 7.4.1.1. The χ^2 value being smaller than the χ^2 -critical value indicates a good model fit.

	D_L ($m^2 \cdot s^{-1}$)	D_C ($m^2 \cdot s^{-1}$)	γ	k'_f (s^{-1})	k_b (s^{-1})	$[C]_i$ ($mmol \cdot dm^{-3}$)
Value	4.1×10^{-10}	2.0×10^{-10}	2.0	49000	1.0	1.9
Standard Deviation	-	-	-	31000	5.7	4.7
90% confidence interval	-	-	-	92000	17	14
95% confidence interval	-	-	-	140000	24	20
99% confidence interval	-	-	-	310000	56	46
95% t-value	-	-	-	0.036	0.041	0.096
Reference t-value (95%)	2.9					
χ^2	0.33					
χ^2 -critical	6.0 (5 data - 3 fitting parameters = 2 d.o.f.)					

What can be observed from Tables 7.4.1.1 and 7.4.1.2 is similar to what was encountered in Section 6.1.1 with TBP/Ce(IV); the values for k'_f , k_b and $[C]_i$ are accompanied by confidence intervals and standard deviations between two to three orders of magnitude greater than the value. Furthermore, not a single unknown constant in Tables 7.4.1.1 and 7.4.1.2 passes its t-value test. Despite this, the χ^2 value is lower than the χ^2 -critical value in both Tables 7.4.1.1 and 7.4.1.2, which implies a good model fit. The χ^2 test result is due to the fact that the error bars shown in Figure 7.4.1.1 are much larger than those from the TBP/Ce(IV) system in Section 6.1, thus the model fits are within error of the majority of data.

Comparing the mean values of the kinetic rate constants k'_f and k_b for the TODGA/Nd(III) presented in Tables 7.4.1.1 and 7.4.1.2 with the same for the TBP/Ce(IV) system from Section 6.1.1, we can see that k'_f is about two to five times greater and k_b is approximately the same order of magnitude. With all solution concentrations being the same for both TODGA and TBP systems, this result implies that TODGA is a faster-acting complexing ligand than TBP but is similarly prone to decomplexation once the complex has been formed. A TODGA system also counteracts, via this more rapid complexation, the much lower availability of the ligand in the aqueous phase compared to a TBP system. The solubility of TODGA is around a hundred times less than that of TBP.

The natural convergence for $[C]_i$ with the TODGA/Nd(III) system is in-line with the model assumption, which requires $[C]_i$ to converge upon a mean value of 25% or lower of the initial aqueous metal ion concentration, thus implying that metal ion concentration is unperturbed during the experimental time period. Because of the concordance with this assumption in this first instance, i.e. since $[C]_i$ is 1.9 mmol.dm^{-3} for Table 7.4.1.2, for the next estimation $[C]_i$ is assigned to this value. Only the aqueous diffusivities have been taken forward for this analysis as there is minimal difference in the estimated kinetic constants when deploying the organic diffusivities. The following estimation of unknown constants is performed to achieve a better set of associated errors. The results of these runs are presented in Table 7.4.1.3. Since the graphical fit remains the same as shown by Figure 7.4.1.1, it has not been re-presented here.

Table 7.4.1.3: Constants associated with the optimum model fit of the TODGA/Nd(III) system shown by the aqueous diffusivities model results shown in Figure 7.4.1.1. $[C]_i$ boundary condition set at 1.0 mmol.dm^{-3} . The χ^2 value being smaller than the χ^2 -critical value indicates a good model fit.

	D_L ($\text{m}^2.\text{s}^{-1}$)	D_C ($\text{m}^2.\text{s}^{-1}$)	γ	k'_f (s^{-1})	k_b (s^{-1})	$[C]_i$ (mmol.dm^{-3})
Value	4.1×10^{-10}	2.0×10^{-10}	2.0	49000	1.0	1.9
Standard Deviation	-	-	-	24000	1.1	-
90% confidence interval	-	-	-	20000	2.6	-
95% confidence interval	-	-	-	27000	3.6	-
99% confidence interval	-	-	-	50000	6.6	-
95% t-value	-	-	-	0.65	0.28	-
Reference t-value (95%)	2.4					
χ^2	0.35					
χ^2 -critical	7.8 (5 data - 2 fitting parameters = 3 d.o.f.)					

The estimations of the unknown constants described in Table 7.4.1.3 are an improvement, in terms of their confidence intervals and standard deviations, on Tables 7.4.1.1 and 7.4.1.2.

7.4.2 Estimating Unknown Constants Where $[C]_i$ is a Distinct Constant At Each RDC Rotation Speed

Turning to the model where $[C]_i$ is a distinct constant at each rotation speed, Table 7.4.2.1 shows the estimations of unknown constants k'_f , k_b and k_{ex} applying the Stokes-Einstein derived aqueous diffusivities of the ligand and the complex. Figure 7.4.2.1 exhibits the graphical fit.

Firstly, the graphical fits shown by Figure 7.4.2.1 are visually much poorer than the fits for the same chemical system in Section 7.4.1. On a domain of inverse square root of RDC rotation speed, the model curve in Figure 7.4.2.1 has a shallower gradient than the experimental data it is plotted alongside, whereas in other fits generated previously, the model curve plateaus as $\omega^{-0.5}$ tends to 1 or greater, which matches the experimental data in those cases. The general mismatch in the shape of the model curve compared to the experimental data is the reason why the χ^2 values in Table 7.4.2.1 is greater than the χ^2 -

critical value, implying a poor overall model fit using the model where $[C]_i$ is a distinct constant at each rotation speed. Furthermore, the confidence intervals and standard deviations in Table 7.4.2.1 are much larger than in any previous model run being at least one order of magnitude greater than the value itself, in the case of $[C]_i$ but can be as high as five orders of magnitude greater, in the case of k_b . The t-values for all unknown constants are also much smaller than the reference t-value, failing the t-value test, when compared to the estimations of unknown constants in the previous section, implying that no single constant dictates the overall model fit.

No further improvement in the estimation of k_b can be found in these model runs shown in Table 7.4.2.1, and k'_f converges upon a mean value in the same order of magnitude as that found in the constant $[C]_i$ model in the previous section (Table 7.4.1.3). This result emphasises in general the much greater tendency for TODGA to complex with Nd(III) in the aqueous phase of this chemical system than TBP in the system studied in Chapter 6.

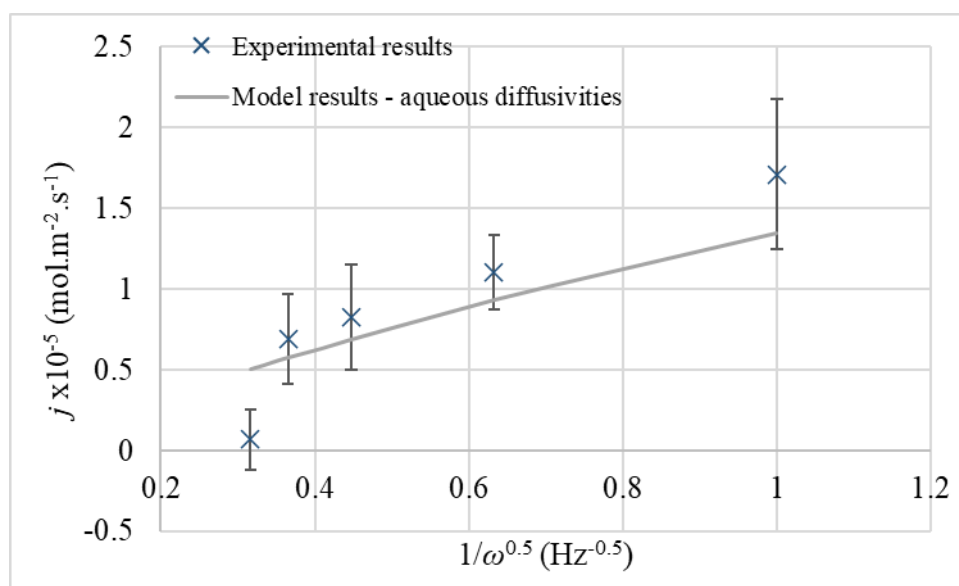


Figure 7.4.2.1: RDC experimental extraction flux, j , of Nd(III) into the organic phase of 0.2 mol.dm^{-3} TODGA in n-dodecane with 5% octanol from an initial aqueous phase of 10 mmol.dm^{-3} Nd(III) in 1.0 mol.dm^{-3} nitric acid, as a function of RDC inverse square root of rotation speed, $\omega^{-0.5}$. Best fit achieved using the model where $[C]_i$ is a distinct constant at each rotation speed in gPROMS.

Table 7.4.2.1: Constants associated with the optimum model fit of the TODGA/Nd(III) system shown by the aqueous diffusivities model results shown in Figure 7.4.2.1. The χ^2 value being larger than the χ^2 -critical value indicates a poor model fit.

	D_L ($m^2 \cdot s^{-1}$)	D_C ($m^2 \cdot s^{-1}$)	γ	k'_f (s^{-1})	k_b (s^{-1})	k_{ex} ($m \cdot s^{-1}$)
	4.1×10^{-10}	2.0×10^{-10}	2.0	11000	1.0×10^{-2}	1.5×10^{-6}
Standard Deviation	-	-	-	4.6×10^5	1.74	3.3×10^{-5}
90% confidence interval	-	-	-	1.3×10^6	5.1	9.5×10^{-5}
95% confidence interval	-	-	-	2.0×10^6	7.5	1.4×10^{-4}
99% confidence interval	-	-	-	4.5×10^6	17	3.2×10^{-4}
95% t-value	-	-	-	0.0058	0.0013	0.011
Reference t-value (95%)	2.9					
χ^2	7.0					
χ^2 -critical	6.0 (5 data - 3 fitting parameters = 2 d.o.f.)					

The mean k_{ex} value resulting from this estimation, shown in Table 7.4.2.1 results in interfacial complex concentrations, $[C]_i$, from approximately $3 \text{ mmol} \cdot \text{dm}^{-3}$, at an RDC rotation speed of 10 Hz, to $8 \text{ mmol} \cdot \text{dm}^{-3}$, at a speed of 1 Hz. These interfacial concentrations of complex are too high for the system to adhere to the assumption that metal ion concentration is not perturbed by the complexation reaction. However, the standard deviation for the nominal k_{ex} value estimated here is so large in Table 7.4.2.1 that the arbitrary setting of this constant to a more suitable value is justified to ensure that $[C]_i$ does not become larger than around 10% of the available metal ion concentration. To this end, k_{ex} is set to $8.00 \times 10^{-6} \text{ m} \cdot \text{s}^{-1}$ in the following estimations which results in a $[C]_i$ range of $0.7 - 1.3 \text{ mmol} \cdot \text{dm}^{-3}$. Figure 7.4.2.2 shows the graphical fit Table 7.4.2.2 are the associated constants which define it.

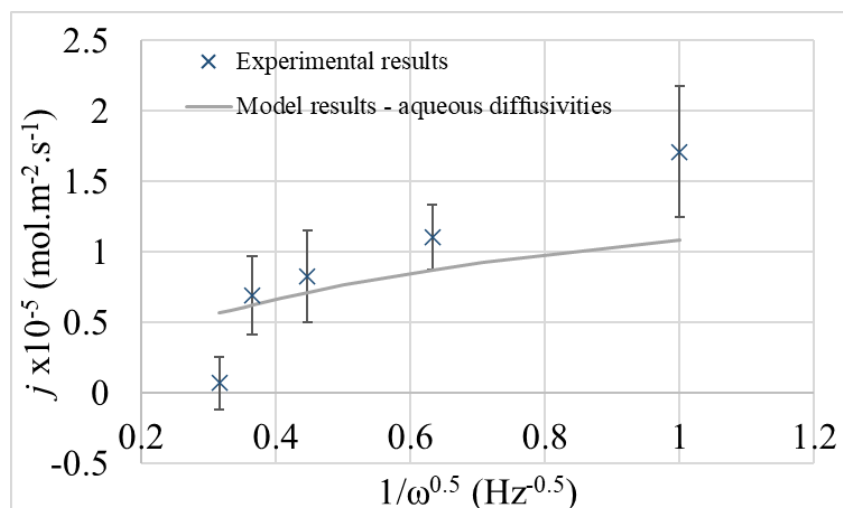


Figure 7.4.2.2: RDC experimental extraction flux as a function of RDC inverse square root of rotation speed, $\omega^{-0.5}$, j , of Nd(III) into the organic phase of 0.2 mol.dm^{-3} TODGA in n-dodecane with 5% octanol from an initial aqueous phase of 10 mmol.dm^{-3} Nd(III) in 1.0 mol.dm^{-3} nitric acid. k_{ex} boundary condition set at $8.00 \times 10^{-6} \text{ m.s}^{-1}$. Best fit achieved using the model where $[C]_i$ is a distinct constant at each rotation speed in gPROMS.

Table 7.4.2.2: Constants associated with the optimum model fit of the TODGA/Nd(III) system shown by the organic diffusivities model results shown in Figure 7.4.2.2. k_{ex} boundary condition set at $8.00 \times 10^{-6} \text{ m.s}^{-1}$. The χ^2 value being larger than the χ^2 -critical value indicates a poor model fit.

	D_L ($\text{m}^2.\text{s}^{-1}$)	D_C ($\text{m}^2.\text{s}^{-1}$)	γ	k'_f (s^{-1})	k_b (s^{-1})	k_{ex} (m.s^{-1})
	4.1×10^{-10}	2.0×10^{-10}	2.0	1100	1.0×10^{-4}	8.0×10^{-6}
Standard Deviation	-	-	-	68	0.63	-
90% confidence interval	-	-	-	1500	1.3	-
95% confidence interval	-	-	-	2000	1.8	-
99% confidence interval	-	-	-	3800	3.6	-
95% t-value	-	-	-	0.53	5.0×10^{-5}	-
Reference t-value (95%)	2.4					
χ^2	10					
χ^2 -critical	7.8 (5 data - 2 fitting parameters = 3 d.o.f.)					

The standard deviation and confidence intervals shown in Table 7.4.2.2 are much smaller than in the previous analysis where k_{ex} was unset and allowed to converge. This generates

more confidence in the estimation k'_f . The mean value of k_b does not change in Table 7.4.2.2 compared to the previous analysis and the standard deviation and confidence intervals remain very large for this constant. Thus, the deduction remains the same; that the forwards rate of complexation is faster and more dominant to the model fit than the decomplexation. This is further supported by the t-values for k'_f which are only five times smaller than the reference t-value, still implying a failure of the t-value test, but by a decreased margin than observed in Table 7.4.2.1 in the previous analysis. Due to the shape of the model fits, as in Table 7.4.2.1 in the previous analysis, the χ^2 values are lower than the χ^2 -critical values in Table 7.4.2.2, implying a poor model fit. To aid understanding of the fundamental causes of the poor model fits in this section, and the trade-offs between different constants, a sensitivity analysis was performed and is discussed below.

The graphical fits of the model where $[C]_i$ is a distinct constant at each rotation speed, when k_{ex} is set to $8.00 \times 10^{-6} \text{ m.s}^{-1}$, shown by Figure 7.4.2.2, are visibly poorer than when k_{ex} is allowed to converge in the case shown by Figure 7.4.2.1. As can be seen in Figure 7.4.2.3, which presents a sensitivity analysis for k_{ex} , the model curve for flux in the $\omega^{-0.5}$ domain approaches a horizontal orientation, i.e. the model curve has a gradient of zero, as k_{ex} tends to the very high or very low values in the range $1 \times 10^{-7} - 5 \times 10^{-5} \text{ m.s}^{-1}$. This phenomenon causes there to be a poor model fit and a failure in the χ^2 tests because the experimental flux data do not have a zero gradient when plotted against $\omega^{-0.5}$ but a positive gradient. The range of $[C]_i$ produced from these model fits is also shown in the legend of Figure 7.4.2.3 and it is clear to see that small values of k_{ex} produce the largest range over the different RDC rotation speeds and the biggest upper bound values of $[C]_i$. In contrast, large values of k_{ex} produce only a small range of $[C]_i$ values with a small upper bound value, adhering to our assumption defined in the model theory, that the metal ion concentration is unperturbed. Thus, a trade-off becomes manifest whereby k_{ex} should ideally be as large as the model will allow before the gradient of the flux as a function of inverse square root of RDC rotation speed becomes zero at very high k_{ex} . $k_{ex} = 8.0 \times 10^{-6} \text{ m.s}^{-1}$ represents an optimum point in this trade-off.

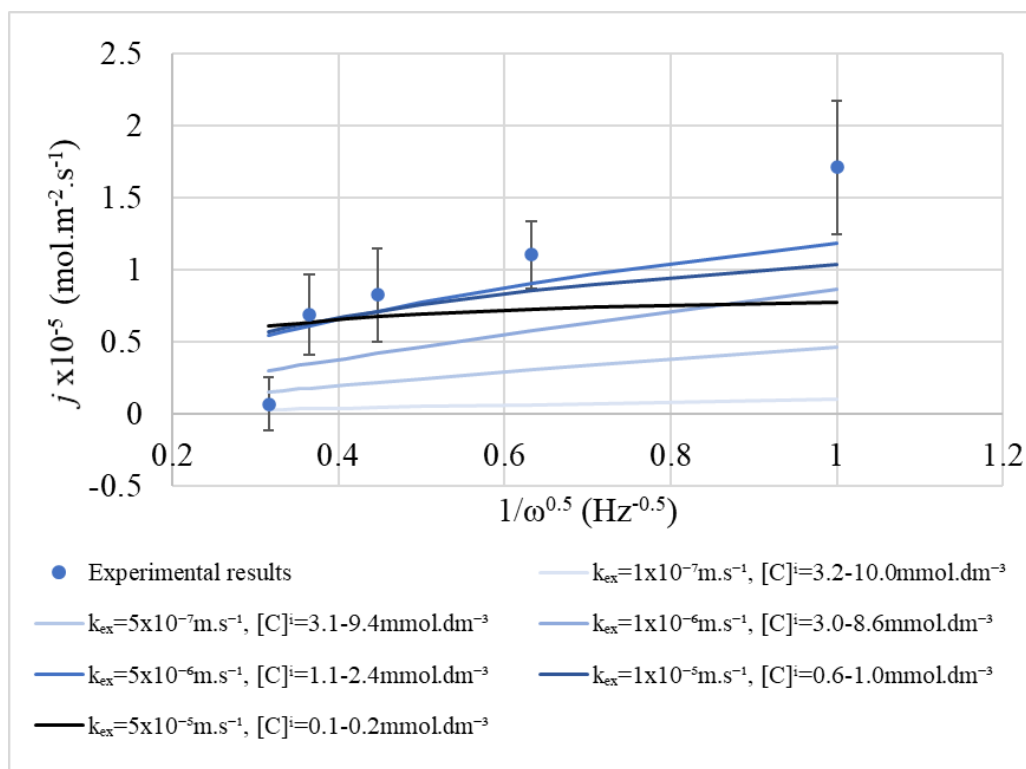


Figure 7.4.2.3: Sensitivity analysis of k_{ex} using model fits of the TODGA/Nd(III) RDC experimental data.

As with the TBP/Ce(IV) system, an understanding of the quantitative concentration profiles of the ligand and complex throughout the diffusion region in the TODGA/Nd(III) reactive system proves insightful for both models: where $[C]_i$ is a constant and where $[C]_i$ is a distinct constant at each rotation speed. This is the subject of the next section.

7.5 Analysis of Ligand and Complex Concentration Profiles

Firstly, the analysis of the concentration profiles for the constant $[C]_i$ boundary condition model is presented. Figure 7.5.1 presents the concentration profiles for free TODGA ligand and TODGA/Nd(III) complex in the aqueous diffusion layer with the aqueous/organic interface being defined at $x = 0$. Unlike the TBP/Ce(IV) data, the free ligand profile of TODGA is unchanged at all rotation speeds implying that there is no steady state build-up of free TODGA at large distances from the interface; free TODGA remains within $1 \mu\text{m}$ of the interface. Therefore, the RDC rotation speed does not affect the steady state build-up of TODGA in the aqueous phase. The hydrodynamic diffusion layer, controlled by RDC rotation speed, principally affects the complex concentration profile which governs the flux behaviour and the rate of overall extraction.

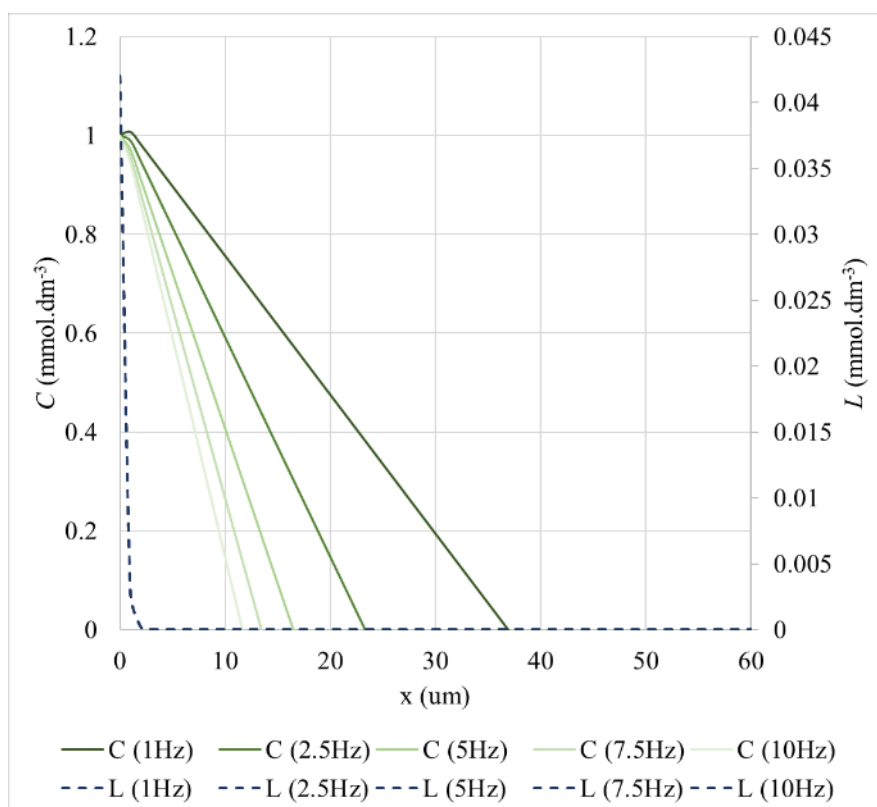


Figure 7.5.1: Aqueous phase diffusion layer concentration profiles resulting from the constant $[C]_i$ model of TODGA (shown by L) and Nd(III)/TODGA complex (shown by C) with diffusivities derived via the Stokes-Einstein equation. List of Constants:

$D_L = 4.1 \times 10^{-10} \text{ m}^2 \cdot \text{s}^{-1}$, $D_C = 2.0 \times 10^{-10} \text{ m}^2 \cdot \text{s}^{-1}$, $\gamma = 2.0$, $k_f' = 49000 \text{ s}^{-1}$, $k_b = 1.0 \text{ s}^{-1}$,
 $[C]_i = 1.9 \text{ mmol} \cdot \text{dm}^{-3}$.

Similar to the TBP/Ce(IV) system, the values of $[C]_{\max}$ and X_D for the TODGA/Nd(III) system can be considered to be controlled by the competition between three processes:

- (i) the rate of reaction of TODGA with Nd(III) in the aqueous phase as TODGA extracts into the aqueous from the organic phase/membrane;
- (ii) once formed, diffusion of the complex to the membrane surface prior to extraction into the organic phase;
- (iii) a competing diffusion process whereby the formed complex diffuses to the outer edge of the diffusion layer at $x = X_D$ prior to it being lost to the convectively stirred bulk solution at $x > X_D$.

The concentration profile of the complex in Figure 7.5.1 is essentially a straight line subtended from the non-zero interfacial concentration, $[C]_i$, to zero at the complex diffusion

layer thickness, which decreases as RDC rotation speed is increased from 1 to 10 Hz. This concentration profile indicates that a TODGA/Nd(III) extraction system is diffusion-limiting to a greater extent than it is kinetically-limiting. This interpretation, that a diffusion-limiting system is manifest, is backed up by the estimations of the unknown constants in the preceding sections of this chapter as a very high forwards rate constant of complexation was procured, as well as a very small decomplexation rate constant.

Similar to the TBP/Ce(IV) system, at higher rotation rates the value of $\frac{d[C]}{dx}$ at $x = X_D$ is steep and large and a significant fraction of complex generated is lost to the solution bulk at $x > X_D$. However, as the rotation speed is decreased, $\frac{d[C]}{dx}$ at $x = X_D$ becomes less steep with the consequence that the fraction of complex lost to the bulk decreases. This results in an increase in $[C]_{\max}$ within the diffusion layer which in turn gives rise to an increase in $\frac{d[C]}{dx}$ at $x = 0$ and thus the extraction flux.

In the TBP/Ce(IV) concentration profiles in Section 6.2, the $[C]_{\max}$ points were clearly visible as they fell somewhere within 10 μm of the interface at $x = 0$. In this section for TODGA/Nd(III), the peaks in the concentration profiles are not observable in Figure 7.5.1 due to the fact that they fall within 1 μm of the interface. Thus, a zoomed in plot of the same concentration profiles are presented in Figure 7.5.2. Although the $[C]_{\max}$ points emerge far closer to the interface in the TODGA/Nd(III) system than the TBP/Ce(IV) system, the trend remains the same in that the peak at higher rotation speeds are smaller in magnitude and occur closer to the interface than those at low rotation speeds. This implies that there is a much greater volume of complex diffusing *towards* the interface, at lower rotation speeds, than at higher rotation speeds. Furthermore, the driving force of the flux towards the interface, which is the complex concentration gradient, is increased when the $[C]_{\max}$ point is greater in magnitude, which occurs for lower rotation speeds.

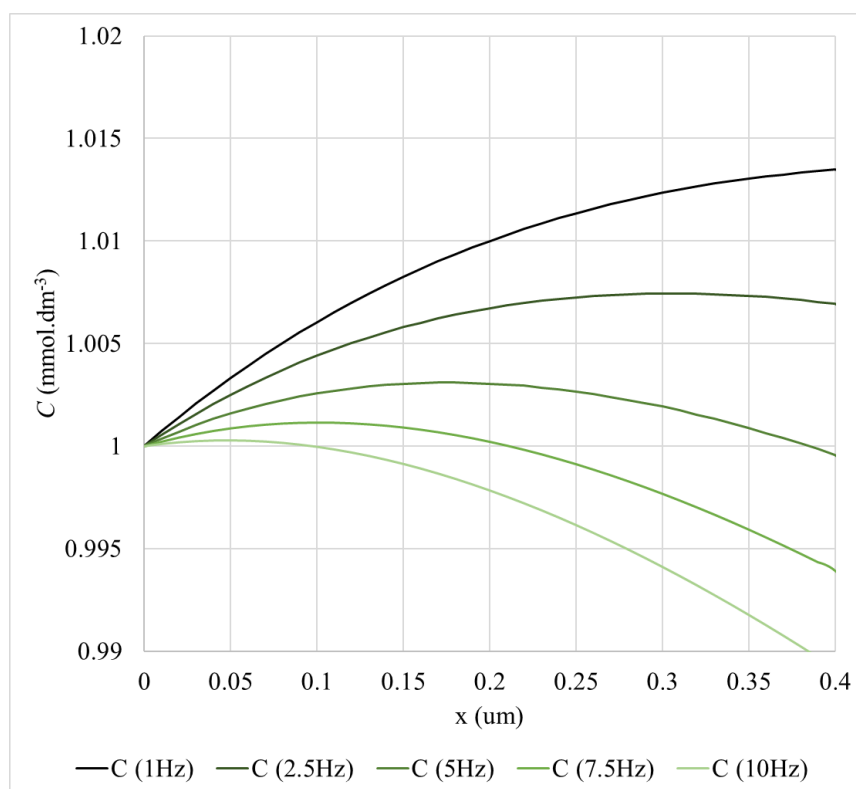


Figure 7.5.2: Zoomed in concentration profile of complex for the system described by the right hand plot of Figure 7.5.1. It is clear to see the negative slope of the complex concentration profile at distances very close to the interface at $x=0$.

Moving to the model where $[C]_i$ is a distinct constant at each rotation speed, concentration profiles obtained from the estimations of the unknown parameters given in Table 7.4.2.2 are presented in Figure 7.5.3.

What can be deduced from Figure 7.5.3, in terms of the overall trends in extraction and the reasons for these trends, is much the same as with the constant $[C]_i$ model concentration profiles, shown by Figure 7.5.1. To summarise briefly again, the ligand concentration profile is unchanged by the RDC rotation speed variation, however the complex concentration profiles have a far greater reach into the aqueous diffusion layer at lower rotation speeds compared to higher rotation speeds. Furthermore, the $[C]_{\max}$ points in Figure 7.5.3, which describe the concentration profile peaks, occur within $1\mu\text{m}$ of the interface which is why they are not easily discernible from the plot. The trend remains the same in that the peaks at higher rotation speeds are smaller in magnitude and occur closer to the interface than those at low rotation speeds. This implies that there is a much greater volume of complex diffusing *towards* the interface, at lower rotation speeds, than at higher rotation speeds. The only difference in the concentration profiles, shown by Figure 7.5.3, compared Figure 7.5.1, is the

interfacial concentrations of complex $[C]_i$, which range from approximately $0.7 - 1.4 \text{ mmol.dm}^{-3}$. Despite the difference in their interfacial concentrations, both models produce concentration profiles with similar properties, resulting in almost identical understandings of how the overall extraction is governed.

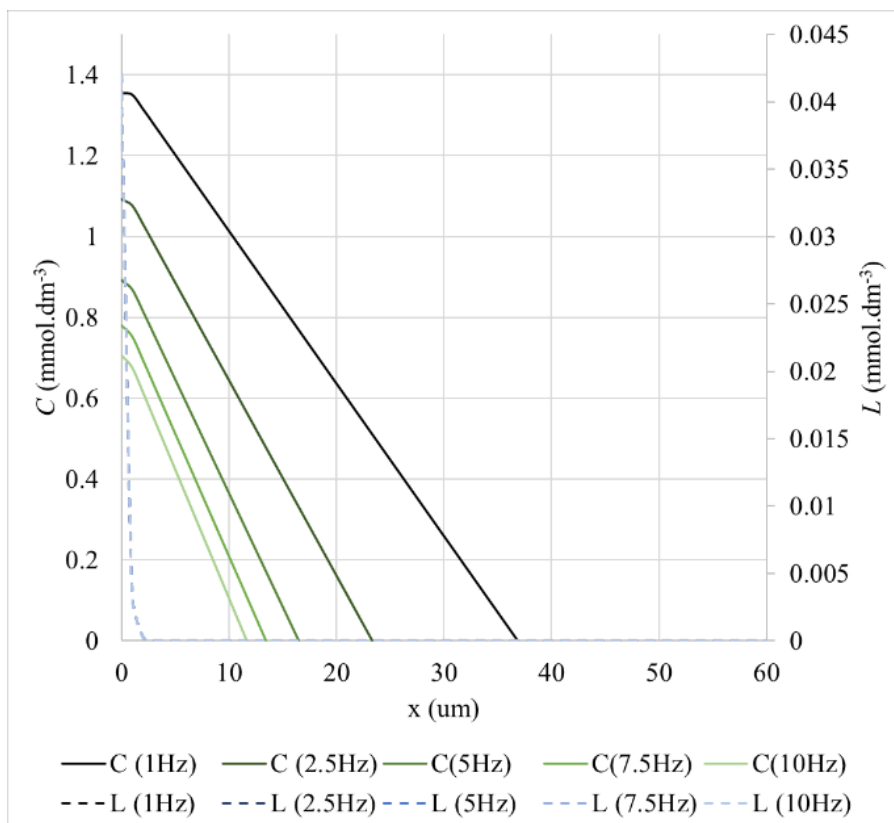


Figure 7.5.3: Aqueous phase diffusion layer concentration profiles of TODGA (shown by L) and Nd(III)/TODGA complex (shown by C). The concentration profiles were made using the model where $[C]_i$ is a constant at each RDC rotation speed. The diffusivities were derived via the Stokes-Einstein equation. List of Constants: $D_L = 4.1 \times 10^{-10} \text{ m}^2.\text{s}^{-1}$, $D_C = 2.0 \times 10^{-10} \text{ m}^2.\text{s}^{-1}$, $\gamma = 2.0$, $k_f' = 1100 \text{ s}^{-1}$, $k_b = 1.0 \times 10^{-4} \text{ s}^{-1}$, $k_{ex} = 8.0 \times 10^{-6} \text{ m.s}^{-1}$.

The following section collates all the findings of both RDC studies shown in this thesis; the TBP extraction of Ce(IV), and the TODGA extraction of Nd(III).

Chapter 8: Conclusions and Further Work

It has been found that the complexation process between TBP and Ce(IV), and between TODGA and Nd(III), occurs in the diffusion layer in the aqueous phase, near to the membrane-supported interface between the aqueous and organic phases. It is precisely due to the emergence of the complex in this diffusion layer that the inverse dependency of extraction rate on RDC rotation speed is manifest as the analytical modelling shows and the concentration profile analysis additionally supports.

In both unknown constants estimations, for the TBP and the TODGA systems, small variations (~25%) in the diffusion coefficients of the species in the aqueous phase, i.e. of the free ligand and the complex, do not significantly change the estimations. However, the value chosen for the interfacial complex concentration $[C]_i$ can change the estimated values of the kinetic constants considerably. This is addressed by setting $[C]_i$ either to a small value, in the case of the model where $[C]_i$ is a constant, or allowing it to vary across multiple small values as a function of flux, in the case of the model where $[C]_i$ is a distinct constant at each rotation speed.

For the TBP/Ce(IV) extraction system, the fits using the model where $[C]_i$ is a constant produced the values of k'_f as 12 - 14 s⁻¹ and k_b as 3 - 4 s⁻¹, whereas the fits using the model where $[C]_i$ is a distinct constant at each RDC rotation speed produced the value of k'_f as 5 - 6 s⁻¹ and k_b as 1 - 2 s⁻¹. Although there is some discrepancy between the results, the magnitude of their difference is small and furthermore, in both cases, the forwards rate constant of complexation is approximately five times greater than the decomplexation rate. The relatively low values of kinetic rate constants bring about the conditions that ensure that TBP systems are controlled by both diffusive *and* kinetic forces, rather than by diffusion alone. These findings for the TBP/Ce(IV) extraction system when investigated via RDC experiments have given a great deal of insight into the anticipated mechanism of the MTWCR process which is ultimately driving the overall extraction. As discussed above, TBP has been a commonly deployed ligand throughout the history of nuclear partitioning processes. As such, there is general consensus in the literature regarding the literature values used in the estimations presented here.

In the case of the TODGA/Nd(III) system, the fits using the model where $[C]_i$ is a constant produced the value of k'_f as $\sim 30000 \text{ s}^{-1}$ ($\pm 20000 \text{ s}^{-1}$) and k_b as $\sim 1.0 \text{ s}^{-1}$ ($\pm 4 \text{ s}^{-1}$), whereas the fits using the model where $[C]_i$ is a distinct constant at each RDC rotation speed produced the value of k'_f as $\sim 1000 \text{ s}^{-1}$ ($\pm 70 \text{ s}^{-1}$) and k_b as negligible. There is a great amount of variation in these results, however the finding that the that, overall, TODGA-based extraction systems have a far greater drive towards complexation than TBP-based systems, is well founded. The concentration profiles imply that TODGA-based extraction systems are diffusion controlled to a far greater extent than they are kinetically controlled.

The above findings provide useful knowledge to assist the selection of liquid/liquid contactor techniques. The rate determining step for the extraction of Ce(IV) by TBP is a mixture of chemical kinetics and diffusion across the aqueous phase diffusion layer. Diffusion limitations may be minimised by deploying a contactor which achieves high shear forces when mixing, such as a centrifugal contactor. However, for a design choice such as this, the overall extraction may not increase compared to a scenario in which a lower shear contactor, such as a box mixer settler, is deployed because the chemical kinetics slow down the rate of overall extraction. Use of centrifugal contactors or pulse columns may not improve upon the effectiveness of PUREX-based extractions. In contrast, TODGA-based liquid/liquid extraction systems are much less limited by chemical kinetics, which means that centrifugal contactors or pulse columns could significantly increase the efficiency of these extractions. EU consortiums which fund the development of the i-SANEX and GANEX processes will benefit from the research undertaken in this PhD. However, this is based on the microscale studies conducted during this PhD and will need further study in the macroscale.

For liquid/liquid extraction systems more generally, the use of the RDC has shown itself to be uniquely capable of studying extraction at a large range of shear conditions. Liquid/liquid extraction has been used widely in nuclear reprocessing but has the potential for use in a variety of emerging industries which NNL, part funder of this PhD, is contributing to. For example, the decontamination of infrastructures following chemical warfare and the destruction of chemical weapons more widely is a growth area for which chemical kinetic and diffusive mass transfer studies can provide key knowledge.

Further work specifically to lead on from this author's work must include the deployment of liquid phases containing actinides rather than analogous metal ions. For studies based on

TODGA, RDC data for Am or Cm will underpin the chemistry of the real i-SANEX system. Consequently, the results can be directly compared to similar studies on Am already undertaken in the RMC by Simonin et al in European laboratories (Simonin, Boxall, & Lélías, 2019; Simonin, Boxall, & Lélías, 2015).

Bibliography

- Albery, W. J., & Choudhery, R. A. (1988). Kinetics and Mechanism of the Solvent Extraction of Copper. *Journal of Physical Chemistry*, *92*, 1142-1151.
- Albery, W. J., Archer, M. D., & Edgell, J. (1977). *Journal of Electroanalytical Chemistry*, *82*, 199.
- Albery, W. J., Bowen, W. R., Fisher, F. S., & Turner, A. D. (1980). Photogalvanic cells: Part IX. Investigations using transparent rotating disk electrode. *Journal of Electroanalytical Chemistry and Interfacial Electrochemistry*, *107*(1), 11-22.
- Albery, W. J., Burke, J. F., Leffler, E. B., & Hadgraft, J. (1976). Interfacial transfer studied with a rotating diffusion cell. *Journal of the Chemical Society, Faraday Transactions 1*, *72*, 1618-1626.
- Albery, W. J., Choudhery, R. A., & Fisk, P. R. (1984). Kinetics and Mechanism of Interfacial Reactions in the Solvent Extraction of Copper. *Faraday Discussions of the Chemistry Society*, *77*, 53-65.
- Albery, W. J., Couper, A. M., Hadgraft, J., & Ryan, C. (1974). Transport and kinetics in two phase systems. *Journal of the Chemical Society, Faraday Transactions 1*, *70*, 1124-1131.
- Amsler, C. (2015). *Nuclear and Particle Physics*. Bristol: IOP Publishing.
- Bevington, P. R., & Robinson, D. K. (1994). *Data Reduction and Error Analysis for the Physical Sciences* (2 ed.). International: McGraw-Hill Inc.
- Boslaugh, S. (2012). Chapter 6. The t-Test. In *Statistics in a Nutshell, 2nd Edition*. O'Reilly Media, Inc.
- Boxall, C. (2022). Personal communications.
- Boxall, C., & Albery, W. J. (2000). Photochemistry with the optical rotating disk electrode. Part 2. Steady-state and transient studies on colloidal CdS. *Physical Chemistry Chemical Physics*, *2*, 3641-3650.
- Boxall, C., & Albery, W. J. (2000). Photoelectrochemistry with the optical rotating disk electrode. Part 1. The theoretical analysis for photophysical-electrochemical processes. *Physical Chemistry Chemical Physics*, *2*, 3631-3639.
- Bromley, M. (2021). Personal communications.
- Bromley, M., & Boxall, C. (2015). A study of cerium extraction by TBP and TODGA using a rotating diffusion cell. *Nucleonika*, *60*(4), 859-864. Retrieved from <https://doaj.org/article/8027136e4c084685b5dd8bebc30>
- Burchell, T. D. (2001). Nuclear Graphite and Radiation Effects. In *Encyclopedia of Materials: Science and Technology (2nd Edition)* (pp. 6310-6319). Elsevier.
- Carrot, M., Bell, K., Brown, J., Geist, A., Gregson, C., Hères, X., . . . Taylor, R. (2014). Development of a New Flowsheet for Co-Separating the Transuranic Actinides: The "EURO-GANEX" Process. *Solvent Extraction and Ion Exchange*, *32*, 447-467.
- Chen, H., Taylor, R., Jobson, M., Woodhead, D., & Masters, A. (2016). Development and Validation of a Flowsheet Simulation Model for Neptunium Extraction in an Advanced PUREX Process. *Solvent Extraction and Ion Exchange*, *34*(4), 297-321.
- Corne, F., Lélías, A., Magnaldo, A., Sorel, C., Raimondi, N. D., & Prat, L. (2019). Experimental Methodology for Kinetic Acquisitions Using High Velocities in a Microfluidic Device. *Chemical Engineering & Technology*, *42*(10), 2223-2230.
- Cotton, S. A. (Ed.). (2006). *Lanthanide and Actinide Chemistry*. Hoboken: John Wiley & Sons.
- Edwards, S., Andrieux, F., Boxall, C., Sarsfield, M. J., Taylor, R. J., & Woodhead, D. (2019). Neptunium(IV)-hydroxamate complexes: their speciation, and kinetics and mechanism of hydrolysis. *Dalton Transactions*, *48*, 673-687.

- Gamry Instruments. (2021). *Spectroelectrochemistry - Part 1: Getting Started*. Retrieved 4 21, 2021, from <https://www.gamry.com/application-notes/physechem/spectroelectrochemistry-part-1-getting-started/>
- Geist, A., Müllich, U., Magnusson, D., Kaden, P., Modolo, G., Wilden, A., & Zevaco, T. (2012). Actinide(III)/Lanthanide(III) Separation Via Selective Aqueous Complexation of Actinides(III) using a Hydrophilic 2,6-Bis(1,2,4-Triazin-3-Yl)-Pyridine in Nitric Acid. *Solvent Extraction and Ion Exchange*, 30, 433-444.
- Gschneidner, K. A., Bünzli, J.-C. G., & Pecharsky, V. K. (Eds.). (2006). Applications of Tetravalent Cerium Compounds. *Handbook on the Physics and Chemistry of Rare Earths*, 36, 304.
- Hammerstein, A. F., Shin, S.-. H., & Bayley, H. (2010). Single-Molecule Kinetics of Two-Step Divalent Cation Chelation. *Angewandte Chemie (International ed.)*, 49(30), 5085-5090.
- Healy, T. V., & McKay, H. A. (1956). The Extraction of Nitrates by Tri-n-Butyl Phosphate (TBP): Part 2. The Nature of the TBP Phase. *Transactions of the Faraday Society*, 52, 633-642.
- Hecht, G. (2012). *Being Nuclear: Africans and the Global Uranium Trade*. Cambridge, Mass: MIT Press.
- Horner, D. E., Mallen, J. C., Coggins Jr, J. R., Thiel, S. W., Scott, T. C., Pih, N., & Yates, R. G. (1980). Interphase Transfer Kinetics of Thorium between Nitric Acid and Tributyl Phosphate Solutions Using the Single Drop and the Lewis Cell Techniques. *Industrial & Engineering Chemistry Fundamentals*, 19(3), 287-291.
- Hughes, M. A., & Biswas, R. K. (1991). The kinetics of vanadium (IV) extraction in the acid sulphate-D2EHPA-n-hexane system using the rotating diffusion cell technique. *Hydrometallurgy*, 26, 281-297.
- Hughes, M. A., & Biswas, R. K. (1993). The kinetics of manganese(II) extraction in the acidic sulphate-D2EHPA-n-hexane using the rotating diffusion cell technique. *Hydrometallurgy*, 32, 209-221.
- Hughes, M. A., & Kuipa, P. K. (1996). Kinetics and Mechanism of Copper Extraction with Dialkylphosphoric Acids and Hydroximes Studied by a Rotating Diffusion Cell. *Industrial & Engineering Chemistry Research*, 35(6), 1976-1984.
- Hughes, M. A., & Rod, V. (1984). A General Model to Account for the Liquid/Liquid Kinetics of Extraction of Metals by Organic Acids. *Faraday Discussions for the Chemistry Society*, 77, 75-84.
- Hughes, M. A., & Zhu, T. (1985). Rates of Extraction of Cobalt from an Aqueous Solution to D2EHPA in a Growing Drop Cell. *Hydrometallurgy*, 13, 249-264.
- IAEA. (2001). *WIMS Library Update Project: Fission Product Yields*. Retrieved 1 17, 2020, from <https://www-nds.iaea.org/wimsd/fpyield.htm>
- Isted, C.-L., & Stetzel, D. (2011). NDA closing Sellafield MOX Plant, says commercial risk too big. *Platts Nuclear Fuels*, 36(16), 1.
- Jackson, A. S., Boxall, C., Bromley, M. A., Taylor, R. J., & Woodhead, D. (2019). The Effects of Nitric Acid on the Extraction Properties of TODGA During Fission Product Management. *Global/Top Fuels 2019*. Seattle: American Nuclear Society.
- Jones, C. J. (2001). *D- and F-block chemistry*. Cambridge: Royal Society of Chemistry Distribution Services.
- Joyce, M. (2016). *Nuclear Engineering, A Conceptual Introduction to Nuclear Power, 1st ed.* Oxford: Butterworth Heinemann.
- Kislik, V. S. (2012). Chapter 4 - Engineering Development of Solvent Extraction Processes. In *Solvent Extraction* (pp. 157-184). Elsevier B.V.

- LabChem. (2021, May). *Safety Data Sheet for Kerosene, Odourless*. Retrieved from [www.labchem.com](https://www.labchem.com/tools/msds/msds/LC15850.pdf): <https://www.labchem.com/tools/msds/msds/LC15850.pdf>
- Lélias, A., & Miguirditchian, M. (2015). CEA Contribution to Deliverable D12.5 - Kinetics to extraction and stripping. *Confidential Publications of SACSESS*, 45-48.
- Levich, V. G. (1962). Solution of the equation for convective diffusion to the surface of a rotating disk. In *Physicochemical Hydrodynamics* (pp. 60-72). Prentice-Hall.
- LibreTexts.org. (2019). *General Chemistry, A Molecular Approach by Nivaldo Tro, Chapter 20: Radioactivity and Nuclear Chemistry*. Retrieved 1 15, 2020
- MacLean, D. W., & Dreisinger, D. B. (1993). The kinetics of zinc extraction in the di (2-ethylhexyl) phosphoric acid, n-heptane-Zn(ClO₄)₂, HClO₄, H₂O system using the rotating diffusion cell. *Hydrometallurgy*, 33, 107-136.
- Magnusson, D., Christiansen, B., Glatz, J.-P., Malmbeck, R., Modolo, G., Serrano-Purroy, D., & Sorel, C. (2009). Development of a TODGA based process for partitioning of actinides from a PUREX raffinate part III: Centrifugal contactor runs using genuine fuel solution. *Solvent Extraction and Ion Exchange*, 27(1), 26-35.
- Mandin, P., Fabian, C., & Lincot, D. (2006). Numerical Simulation of Hydrodynamic and Mass-Transport Properties at a Laminar Rotating Cylinder Electrode. *Journal of The Electrochemical Society*, 153(3), D40-D50.
- Marshall, P., & MacLachlan, A. (2000). U.K. OFFICIALS NEARING VISIT TO JAPAN FOR MOX DISCUSSIONS. *Platts Nuclear Fuels*, 25(14), 12.
- Martin, B. R. (2011). *Nuclear and Particle Physics: An Introduction, 2nd ed.* Somerset: Wiley.
- Meng, M. X., Yu, S., & Chen, J. C.-. (1996). Kinetics of iron(III) extraction with primary amine and TBP using a modified rotating diffusion cell. *Hydrometallurgy*, 41, 55-70.
- Modolo, G., Asp, H., Schreinemachers, C., & Vijgen, H. (2007). Development of a TODGA based process for partitioning of actinides from a PUREX raffinate part I: Batch extraction optimization studies and stability tests. *Solvent Extraction and Ion Exchange*, 25(6), 703-721.
- Modolo, G., Asp, H., Vijgen, H., Malmbeck, R., Magnusson, D., & Sorel, C. (2008). Development of a TODGA based process for partitioning of actinides from a PUREX raffinate part II: Centrifugal contactor runs. *Solvent Extraction and Ion Exchange*, 26(1), 62-76.
- Modolo, G., Wilden, A., Kaufholz, P., Bosbach, D., & Geist, A. (2014). Development and demonstration of innovative partitioning processes (i-SANEX and 1-cycle SANEX) for actinide partitioning. *Progress in Nuclear Energy*, 72, 107-114.
- Nash, K. L., & Lumetta, G. J. (Eds.). (2011). *Advanced separation techniques for nuclear fuel reprocessing and radioactive waste treatment*. Oxford: Woodhead Publishing no.2.
- Nave, S., Modolo, G., Madic, C., & Testard, F. (2004). Aggregation properties of N,N,N',N'-tetraoctyl-3-oxapentanediamide (TODGA) in n-dodecane. *Solvent Extraction and Ion Exchange*, 22(4), 527-551.
- NDA. (2018). *Business Plan: Financial year beginning April 2018 to financial year ending March 2021*. Retrieved 1 22, 2020, from <https://www.gov.uk/government/consultations/nuclear-decommissioning-authority-business-plan-2018-to-2021>
- NDA. (2019). *Draft Business Plan: Financial year beginning April 2020 to financial year ending March 2023*. Retrieved 1 22, 2020, from <https://www.gov.uk/government/consultations/nuclear-decommissioning-authority-draft-business-plan-2020-to-2023>

- NEA. (2011). *Spent Nuclear Fuel Assay Data for Isotopic Validation - State-of-the-art Report*. OECD.
- NEA. (2021). *N,N,N',N'-tetraoctyldiglycolic amide*. (OECD) Retrieved from IDEaL - The International Database for Extractant Ligands: <https://www.oecd-nea.org/ideal/extractants/TODGA>
- Nikolaev, A. V., Afanas'ev, Y. A., Durasov, V. B., & Ryabinin, A. I. (1963). The Determination of the Dimensions of the Molecules of Solvates Formed from Tributyl Phosphate (TBP). *Zhurnal Strukturnoi Khimii*, 5(3), 490-492.
- NIRAB. (2020). *The UK Civil Nuclear R&D Landscape Survey*. NIRO. UK Department of Business, Energy and Industrial Strategy (BEIS).
- NIST. (2013). *Neutron scattering lengths and cross sections*. Retrieved from NIST Center for Neutron Research: <https://www.ncnr.nist.gov/resources/n-lengths/>
- NIST. (2021). Fluid properties of Dodecane (1 bar, 298K). *NIST Standard Reference Database 69: NIST Chemistry WebBook*. Retrieved from <https://webbook.nist.gov/cgi/cbook.cgi?Name=dodecane&Units=SI>
- NIST. (2021). Fluid properties of Water (1 bar, 298K). *NIST Standard Reference Database 69: NIST Chemistry WebBook*.
- Nye, M. J. (Ed.). (2002). *The Cambridge History of Science. Volume 5: The Modern Physical and Mathematical Sciences*. Cambridge: Cambridge University Press.
- Paul, N., Schulz, J. M., & Kraume, M. (2015). Determination of phase separation and mass transfer in complex micellar three phase systems. *Chemical Engineering and Processing*, 99, 143-148.
- Perry, R. H., & Green, D. W. (2007). *Perry's Chemical Engineers' Handbook (8th Edition)*. McGraw-Hill.
- Poinssot, C., Rostaing, C., Grandjean, S., & Boullis, B. (2012). Recycling the Actinides, The Cornerstone of Any Sustainable Nuclear Fuel Cycles. *Procedia Chemistry*, 7(C), 349-357.
- Ravi, J., Mishra, S., Murali, R., Desigan, N., & Pandey, N. K. (2021). Effect of temperature, radiation dose and composition on density, viscosity and volumetric properties of N,N,N',N'-tetraoctyl diglycolamide (TODGA) and n-dodecane mixture, a promising system for the separation of actinides. *Journal of Radioanalytical and Nuclear Chemistry*, 328, 1301-1312.
- Reed, B. C. (2015). *The atomic bomb : the story of the Manhattan Project : how nuclear physics became a global geopolitical game-changer*. London: Morgan and Claypool.
- Ritchie, H., & Roser, M. (2020). *Nuclear Energy, Chapter: Putting death rates from different energy sources in perspective*. Retrieved from Our World in Data: <https://ourworldindata.org/nuclear-energy>
- Rod, V., Strnadová, L., Hančil, V., & Šír, Z. (1981). Kinetics of Metal Extraction by Chelate Formation Part II. Extraction of Cu(II) by Hydroxyoximes. *Chemical Engineering Journal*, 21, 187-193.
- SACSESS. (2015). *Roadmap: Actinide separation processes*. European Commission.
- Sasaki, Y., Sugo, Y., Suzuki, S., & Tachimori, S. (2001). The novel extractants, diglycolamides for the extraction of lanthanides and actinides in HNO₃-n-dodecane system. *Solvent Extraction and Ion Exchange*, 19(1), 91-103.
- Simonin, J. -P., Boxall, C., & Lélías, A. (2019). GENIORS deliverable D5.1 - experimental and modelling studies of transfer kinetics.
- Simonin, J. -P., & Weill, J. (1998). Rotating membrane cell technique for the study of liquid/liquid extraction kinetics. *Solvent Extraction and Ion Exchange*, 16(6), 1493-1514.

- Simonin, J.-P., Boxall, C., & Lelias, A. M. (2015). SACSESS deliverable d12.5 - kinetics of extraction and stripping. (A. Geist, & S. Bourg, Eds.)
- Simonin, J.-P., Perrigaud, L., Perrigaud, K., & Vu, T.-H. (2014). Kinetics of Liquid/Liquid Extraction of Europium(III) Cation by Two Malonic Diamides. *Solvent Extraction and Ion Exchange*, 32, 365-377.
- Singh, M. B., Mukhtyar, A. J., Bootwala, Y. Z., & Gaikar, V. G. (2017). Extraction of cadmium by TODGA-dodecane and TBP-dodecane: A comparative study by MD simulation. *Separation Science and Technology*, 52(7), 1172-1185.
- Singh, M. B., Nayak, S. G., Kanthe, A. D., Patil, R. B., & Gaikar, V. G. (2017). Insight into activity driven third phase formation of TBP in organic solutions by MD simulation. *Journal of Molecular Liquids*, 232, 1-8.
- Sjöstrand, N. G., & Story, J. S. (1960). *Cross sections and neutron yields for U-233, U-235 and Pu-239 at 2200 m/sec*. Stockholm: Aktiebolaget Atomenergi.
- Taylor, R. (Ed.). (2015). *Reprocessing and Recycling of Spent Nuclear Fuel* (Vol. 79). Woodhead Publishing.
- Theobald, D., Hanson, B., Fairweather, M., & Hegggs, P. (2020). Implications of hydrodynamics on the design of pulsed sieve-plate extraction columns: A one-fluid multiphase CFD model using the volume of fluid method. *Chemical Engineering Science*, 221, 115640.
- Van Hecke, K., & Goethals, P. (2006). *Open Report: Research on Advanced Aqueous Reprocessing of Spent Nuclear Fuel: Literature Study*. SCK - CEN. Retrieved from <https://www.osti.gov/etdeweb/servlets/purl/21505070>
- Velavendan, P., Ganesh, S., Pandey, N. K., Geetha, R., Ahmed, M. K., Kamachi Mudali, U., & Natarajan, R. (2013). Studies on solubility of TBP in aqueous solutions of fuel reprocessing. *Journal of Radioanalytical Nuclear Chemistry*, 295(2), 1113-1117.
- Weßling, P., Müllich, U., Guerinoni, E., Geist, A., & Panak, P. (2020). Solvent extraction of An(III) and Ln(III) using TODGA in aromatic diluents to suppress third phase formation. *Hydrometallurgy*, 192, 105248.
- Whittaker, D., Geist, A., Modolo, G., Taylor, R., Sarsfield, M., & Wilden, A. (2018). Applications of Diglycolamide Based Solvent Extraction Processes in Spent Nuclear Fuel Reprocessing, Part 1: TODGA. *Solvent Extraction and Ion Exchange*, 36(3), 223-256.
- Wongsawa, T., Koonsang, T., Kunthakudee, N., Prapasawat, T., Maneeintr, K., & Pancharoen, U. (2018). The experimental investigations on viscosity, surface tension, interfacial tension and solubility of the binary and ternary systems for tributyl phosphate (TBP) extractant in various organic solvents with water. *Journal of Molecular Liquids*, 251, 229-237.
- Woodhead, D., McLachlan, F., Taylor, R., Müllich, U., & Geist, A. (2019). Nitric Acid Extraction into a TODGA Solvent Modified with 1-Octanol. *Solvent Extraction and Ion Exchange*, 37(2), 173-190.
- Woodhead, J. L. (1965). The ultra-violet absorption spectra of nitric acid and metal nitrates in tri-n-butyl phosphate solutions. *Journal of Inorganic and Nuclear Chemistry*, 27(5), 1111-1116.
- World Nuclear Association. (2018). *Safeguards to Prevent Nuclear Proliferation*. Retrieved 1 23, 2020, from <https://world-nuclear.org/information-library/safety-and-security/non-proliferation/safeguards-to-prevent-nuclear-proliferation.aspx>
- Zhu, Z., Sasaki, Y., Suzuki, H., Suzuki, S., & Kimura, T. (2004). Cumulative study on solvent extraction of elements by N,N,N',N'-tetraoctyl-3-octapentanediamide (TODGA) from nitric acid into n-dodencane. *Analytica Chimica Acta*, 527(2), 163-168.

